NASA CR-66158

TECHNICAL REPORT

PROJECT SLOPE
STUDY OF LUNAR ORBITER PHOTOGRAPHIC EVALUATION

By: R.E. Kinzly, P.G. Roetling, and T.M. Holladay

CAL No. VS-2182-D-2

Prepared for:

National Aeronautics and Space Administration
Langley Research Center, Langley Station
Hampton, Virginia 23365

Phase I Final Report
NASI-5800
20 MAY 1966

GPO PRICE $ _____

CFSTI PRICE(S) $ _____

Hard copy (HC) 3.25

Microfiche (MF) 1.00

ff 653 July 65

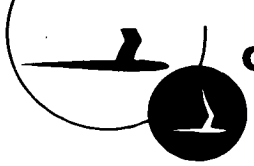

CORNELL AERONAUTICAL LABORATORY, INC.
OF CORNELL UNIVERSITY, BUFFALO, N. Y. 14221

NASA CR-66158

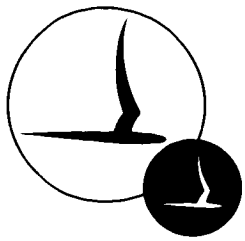

CORNELL AERONAUTICAL LABORATORY, INC.
BUFFALO, NEW YORK 14221

PROJECT SLOPE
STUDY OF LUNAR ORBITER PHOTOGRAPHIC EVALUATION

CAL REPORT NO. VS-2182-D-2
PHASE I FINAL REPORT
CONTRACT NO. NASI-5800
20 MAY 1966

Prepared for:

NATIONAL AERONAUTICS AND SPACE ADMINISTRATION
LANGLEY RESEARCH CENTER, LANGLEY STATION
HAMPTON, VIRGINIA 23365

PREPARED BY: R. E. Kinzly
P. G. Roetling
T. M. Holladay

APPROVED BY: J. Lotsof

J. Lotsof, Head
Observation Sciences Department

ABSTRACT

A Study of Lunar Orbiter Photographic Evaluation (SLOPE) is a continuing investigation conducted for the purpose of determining a method by which quantitative measurements could be made of factors which define the quality of black-white monoscopic photographs to be received from the Lunar Orbiter spacecraft. The first phase of the study included a review of both quality measurement techniques and the operation of the Lunar Orbiter photographic system. From this review, a set of quality measures which define the received photographic quality was established. A set of test targets was selected, some on the lunar surface and some in a pre-exposed data block, from which the quality factors could be measured, and measurement and data reduction techniques were developed. The quality measurements were related theoretically to factors which define directly the ability to extract topographic data from the Lunar Orbiter photographs and possible combinations of these factors to define a figure of merit were suggested. Finally, experimental and theoretical tests were made to check the quality measurement techniques and the variation of the ability to extract topographic information with various possible off-nominal conditions of the Lunar Orbiter system.

It was found that crater shadow-to-sunlight edges, relatively uniform areas on the lunar surface, and data from the pre-exposed data block provide sufficient targets to measure quality in terms of modulation transfer functions, signal gain level, and noise level. The mathematical relations required to reduce these data were developed, programs for an IBM 7044 digital computer were prepared, and the procedures are described. Three factors, the probable errors in: measuring slope angle, slope length, and detecting conical obstacles, were selected to relate quality measurements to the ability to extract topographic information. The mathematical relations were derived by use of statistical communication theory, and the variations of these factors with various operating conditions are shown graphically. It was found experimentally that the methods derived can be used to detect reasonably small operational degradations such as image motion and defocus.

FOREWORD

The research reported herein is the result of studies during the first 16 weeks of a continuing contract from NASA Langley Research Center; Contract No. NAS1-5800 monitored by Mr. T. Hansen.

The authors are grateful to Mr. G. Smith, of Jet Propulsion Laboratory, who supplied the Ranger photographs used for target studies and experimental tests, and Mr. D. Exner, of Boeing Corporation, who participated in a helpful discussion of the noise analysis of the Lunar Orbiter system. Acknowledgement of the contributions of other researchers at Cornell Aeronautical Laboratory is expressed as separate authorship of appendices to the report.

TABLE OF CONTENTS

TABLE OF CONTENTS (Cont.)

LIST OF FIGURES

LIST OF FIGURES (Cont.)

LIST OF FIGURES (Cont.)

1. INTRODUCTION

This is the final report documenting the results achieved during the first phase of the Study of Lunar Orbiter Photographic Evaluation (SLOPE) being conducted under Contract NAS1-5800. As specified in the contract schedule, "The primary objective of this contract is to determine the method by which there can be made a quantitative measure of those factors which define the quality of black-white monoscopic photographs, to be received from the Lunar Orbiter spacecraft."

To meet the contract objective, factors which influence photographic quality were briefly reviewed, and a set of measures which define the quality was selected. However, this set of measures does not necessarily consist of those upon which Lunar Orbiter photographic quality will be determined. Methods were to be determined by which the selected quality measures could be evaluated from the ground reconstructed Lunar Orbiter photographs. To perform this task, the operation of the Lunar Orbiter photographic system had to be examined. The relationships between the quality measures and the ability to detect and measure topographic features (i. e., obstacles and slopes) had to be established and the relative effects of off-nominal performance evaluated. Finally, the feasibility of making the required measurements was to be demonstrated.

To establish the quality of a photographic image, parameters must be defined so as to describe the rendition of detail in the image, the reproduction of tonal quality (i. e. gray levels), and the level of noise (i. e., spurious fluctuations in gray level). All of these parameters can be functions of location in the image, and the first and last can be functions of orientation as well.

The measurement of detail rendition is accomplished by use of a test pattern of known shape and usually quite detailed, as for example bar charts (square waves), sinusoidal patterns, impulses (i. e., points or lines), or step functions (i. e., edges). The problem fro the Lunar Orbiter photographs was to select a "test pattern" on the lunar surface, that is, find

some pattern on the moon for which the detail is already known. It was anticipated that edges were the only feasible target, and the approach described therefore examines various edged objects on the lunar surface. Measures which can be used to describe the detail rendition are[1], for example, point spread, line spread, acutance, or resolution; or, when the system is linear, a spatial frequency analysis may be made and parameters such as modulation transfer function or passband may be used. In general, the approach taken has been to establish where non-linearities exist in the Lunar Orbiter System, and between the non-linearities employ available test patterns to evaluate each linear portion of the system in terms of a modulation transfer function. Other related parameters are used occasionally, as convenient, in intermediate calculations.

The measurement of tonal reproduction and noise level present fewer problems. The tonal reproduction can be measured by use of standard sensitometric procedures so long as a series of standard exposures are placed on the photographic film. Since this procedure is followed in the Lunar Orbiter, this problem has a straightforward solution, and the corresponding quality parameter is simply a measure of signal level or system gain. The measurement of noise level is quite similar to that for other photographic systems, and previous work[2] can be used extensively. Special test targets are not required, so long as adequate knowledge of general noise sources and signal reproduction is available. The technique described uses spatial frequency separation to eliminate residual signals from noise measurements made in areas of relatively low detail content.

The problem of relating the quality parameters to the detection and measurement of topographic features has been approached by application of statistical communication theory to the specific detections or measurements desired. In the case of measuring the slope of the lunar surfaces, the feature of interest is an area where the surface has a given slope for a given distance. Optimum extraction techniques are assumed, and the probable errors in the measurement of the angle of the slope and the length of the slope are evaluated theoretically. In the case of detection of obstacles,

the test obstacle is taken to be a cone of given height and base. The approach again assumes optimum detection in this case by a matched filter, and the probable error of detecting the given obstacles is taken to characterize the performance of the system for detecting obstacles.

The following sections of the report discuss the application of the above approach to the problem of determining a quantitative measure of quality factors of Lunar Orbiter photographs. Section 2 describes in detail the definition of quality parameters, the selection of test targets needed to measure these parameters, and the procedures for extracting the quality measures from the ground reconstructed photographs to be obtained. In Section 3, the relation of the quality parameters to the ability to detect and measure topographic features is considered. Possible means for combining the parameters to a figure of merit are discussed. Experimental verification of the applicability of the measurement techniques by use of Ranger photographs is discussed in Section 4, as well as theoretical evaluations of the effect of nominal and off-nominal conditions on the ability of the Lunar Orbiter System to detect and measure topographic features. Conclusions and recommendations are given last. Several appendices are included which provide mathematical proof of results given in the text.

2. MEASUREMENT OF QUALITY PARAMETERS

The most important task during this project was the definition of a set of quality measures and the establishment of methods for extracting these quality measures from Lunar Orbiter photographs. Three basic types of measures are discussed in the following subsections, that is, the measures of detail rendition, signal level (or gain), and noise level. In each case, appropriate test targets were selected and data reduction procedures established.

2.1 Detail Rendition. - The approach selected for the evaluation of detail rendition was to measure the modulation transfer function (MTF) of the system. Since a modulation transfer function is only defined for a linear system and it cannot be assured that the Lunar Orbiter system is linear end-to-end, this statement should be taken to mean that a separate modulation transfer function would be measured for each connected set of linear elements. The approach is quite reasonable, and has a number of advantages. First, it has become common practice in the optical industry to provide MTF data for components such as lenses and films, thus allowing the use of much existing data in performance comparisons. Second, operational degradations such as uncompensated image motion are readily identifiable in MTF form, even when compounded with other degrading factors. Third, since limiting performance is of most interest, it is to be expected that topographic features of interest will create low contrast images, allowing the whole system to be considered as linear, and the modulation transfer functions can easily be combined for the system.

To select test targets, three questions must be considered: (1) How many non-linear elements are there in the Lunar Orbiter system?, (2) How many regions in the format must be evaluated to characterize the differences in performance across the format?, and (3) Are any changes with orientation to be expected? The first question is answered by examining the block diagram of the Lunar Orbiter system shown in Figure 1. There

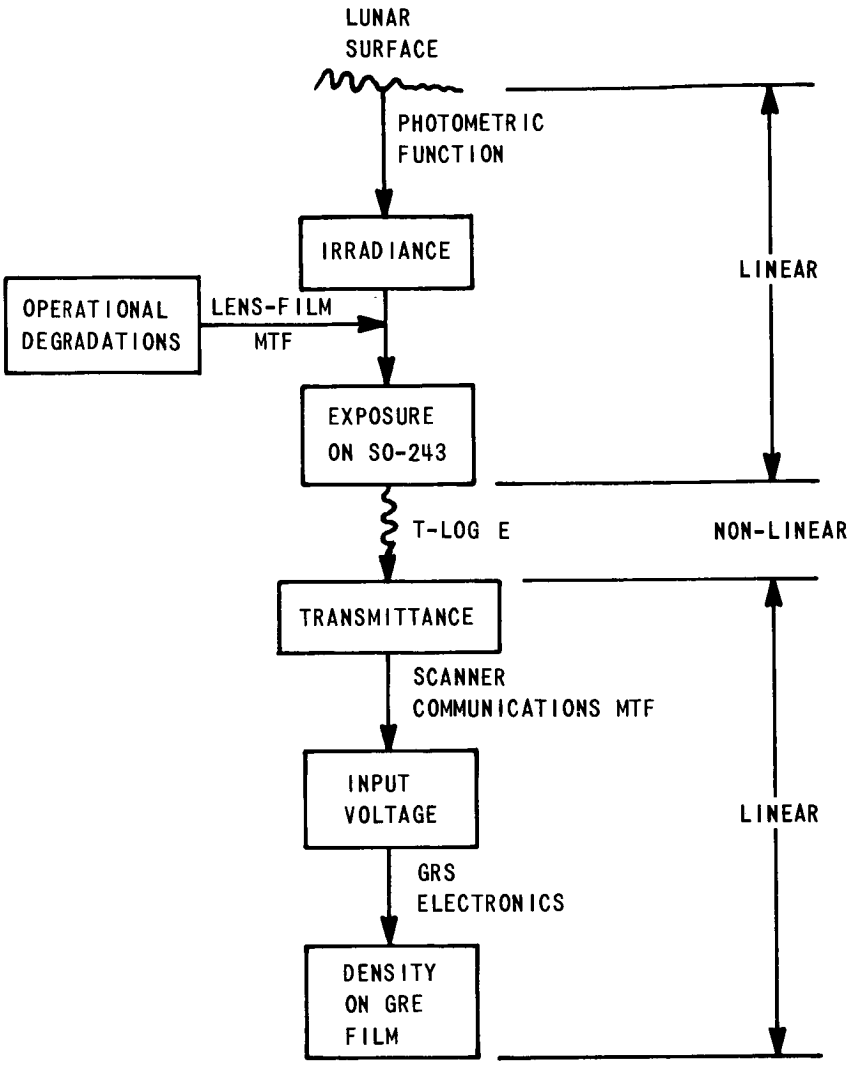

Figure 1 LUNAR ORBITER PHOTOGRAPHIC DATA FLOW DIAGRAM

is only one non-linear element, namely the SO-243 spacecraft film, in a position between linear elements. The fact that the scanner and communications systems can be treated by linear analysis is verified in Appendix A. Thus, two separate modulation transfer functions are required, and two sets of test targets, one on the lunar surface and one pre-exposed on the SO-243 film. Questions 2 and 3, regarding measurement of the changes of MTF with format position and orientation, depend on the nature of the relation between the quality parameter and performance, and are answered in a later section of the report. Pending answers to these questions at this point, it is desirable to select targets on the lunar surface which may appear at various format locations and which can be used to evaluate various orientations. On the SO-243 film, orientation should be considered because these targets will be used to evaluate the scanner and communications systems. In addition, location of the targets, relative to the scanning framelets is important to test scanner defocusing. The selection of targets on the lunar surface is considered below, followed by target selection on the SO-243 film, with the data reduction procedures considered last.

2.1.1 Selection of Targets on the Lunar Surface. - An examination of the lunar surface shows that almost no characteristic targets exist where it can be safely assumed that the detailed shape is known at a level of detail size of less than one meter. Almost the only feasible targets appear to be edged objects, such as edges of craters, rills, or shadows. Figure 2 shows three types of typical crater profiles and their corresponding theoretical intensity distribution in the phase plane. It can be seen from the figure that both the leading edge and final edge in the intensity distribution produced by the rims of the crater are strongly dependent upon the crater type and could only be used as targets if the crater shape were accurately known. On the other hand, the shadow-to-sunlight edge near the center of each intensity distribution remains relatively invarient with crater shape and therefore could be a suitable target.

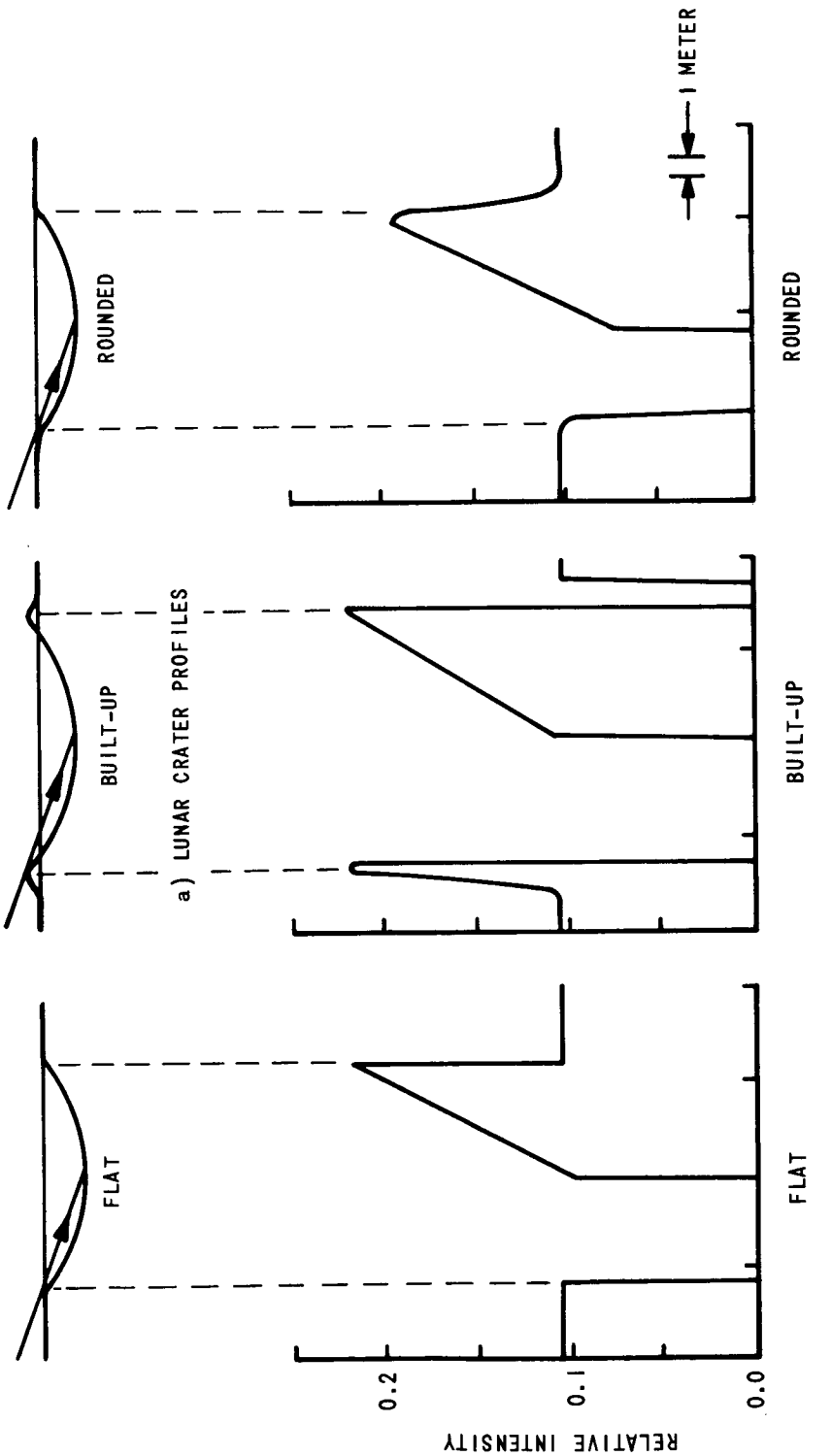

Figure 2 VARIOUS CRATERS AND THEIR INTENSITY DISTRIBUTIONS

Figure 3 shows a microdensitometer trace over a crater in a Ranger 9 photograph, illustrating that built up crater edges can, in fact, be observed and do affect the recorded densities, as shown in the figure. The only possible class of test targets is therefore the shadow-to-sunlight edges. Before these targets can be considered acceptable, the sharpness of the shadow edge and the shape of the total function must be considered.

Figure 4 shows the shadow geometry with a penumbra of length ℓ, created by the approximate $1/2^{o}$ angular subtense of the solar disk. Figure 5 shows the shape of the intensity function through the penumbral region. The equation used to plot the curve shown is derived in Appendix B. Typical penumbral lengths are given in Figure 6, as functions of phase angle and crater size assuming a diameter to depth ratio of 8 which is a typical value[3]. Another characteristic of the shadow-to-sunlight edge is the zero intensity in the shadow and the non-constant intensity beyond the penumbra. The theoretical intensity beyond the penumbra due to a spherical crater floor is derived in Appendix B, and is given by:

$$I_{Rel} = \frac{b_0 + b_1 \alpha(x,y) + b_2 \alpha^2(x,y)}{b_0 + b_1 \alpha(x_p, y_p) + b_2 \alpha^2(x_p, y_p)} \qquad (1)$$

$$\alpha(x,y) = \arctan\left(\frac{x}{\sqrt{a^2 - (x^2 + y^2)}}\right),$$

where:

$$x_p = (a-d)\sin 2\theta - \frac{D}{2}\cos 2\theta \sqrt{1 - \left(\frac{2y_p}{D}\right)^2}$$

x_p, y_p = coordinates of the edge of the interface between the penumbra shadow and the sunlight crater floor.

D = diameter of crater

d = depth of crater

θ = sun angle, i.e., 90^{o} minus the phase angle, and

$$a = \frac{d}{8}\left[4 + \left(\frac{D}{d}\right)^2\right]$$

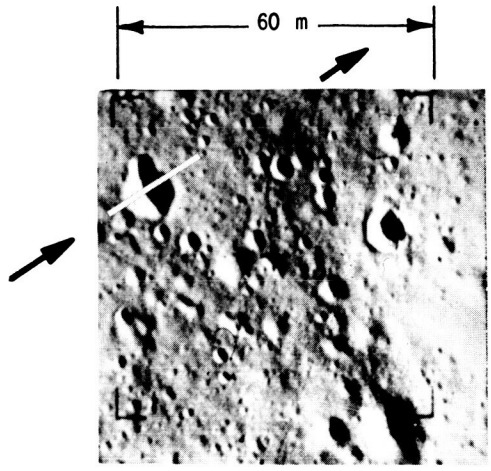

a) RANGER 9 PHOTOGRAPH

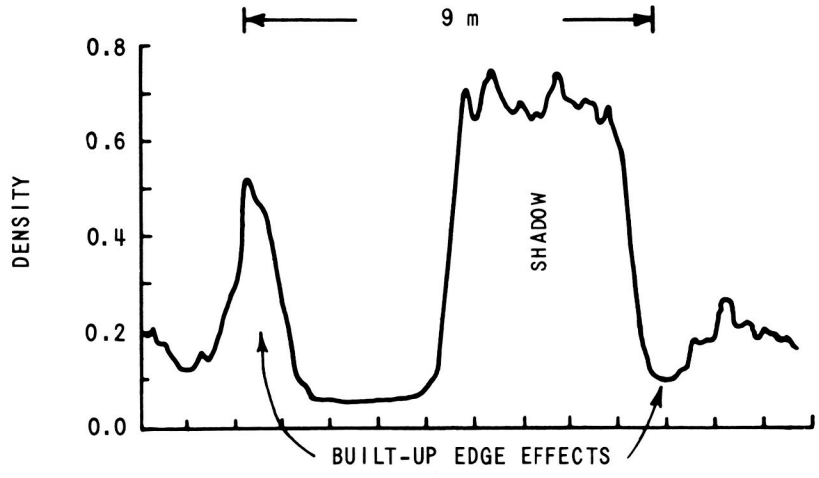

b) TYPICAL CRATER TRACES

Figure 3 EXAMPLE OF BUILT-UP CRATER EDGE FROM RANGER 9.

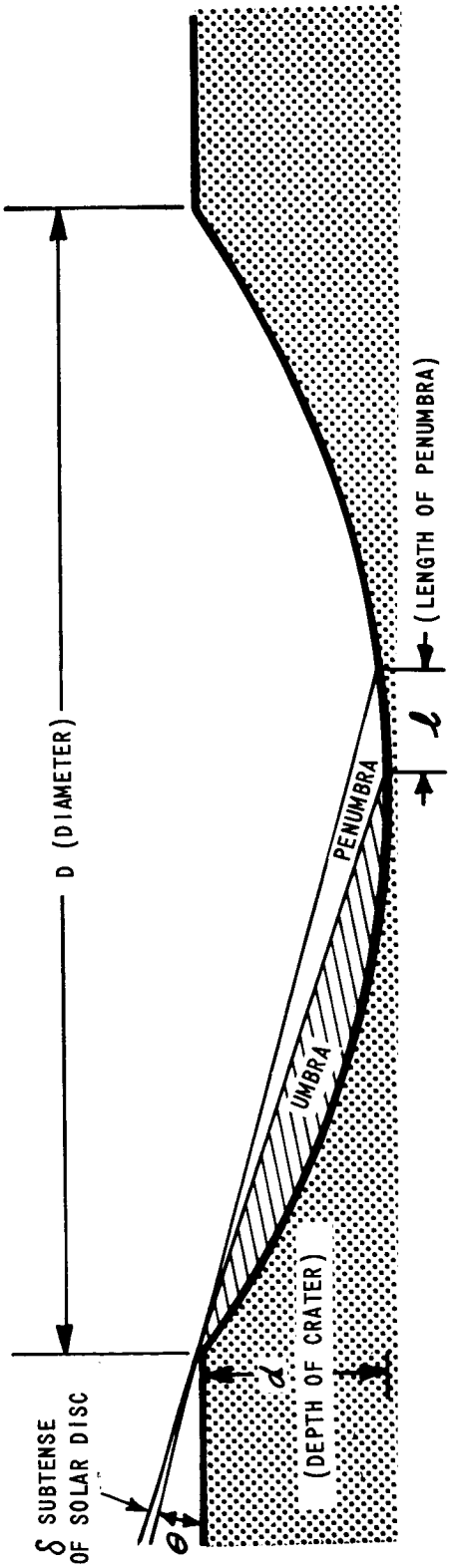

Figure 4 GEOMETRY OF THE SHADOW IN A SPHERICAL CRATER ON THE MOON

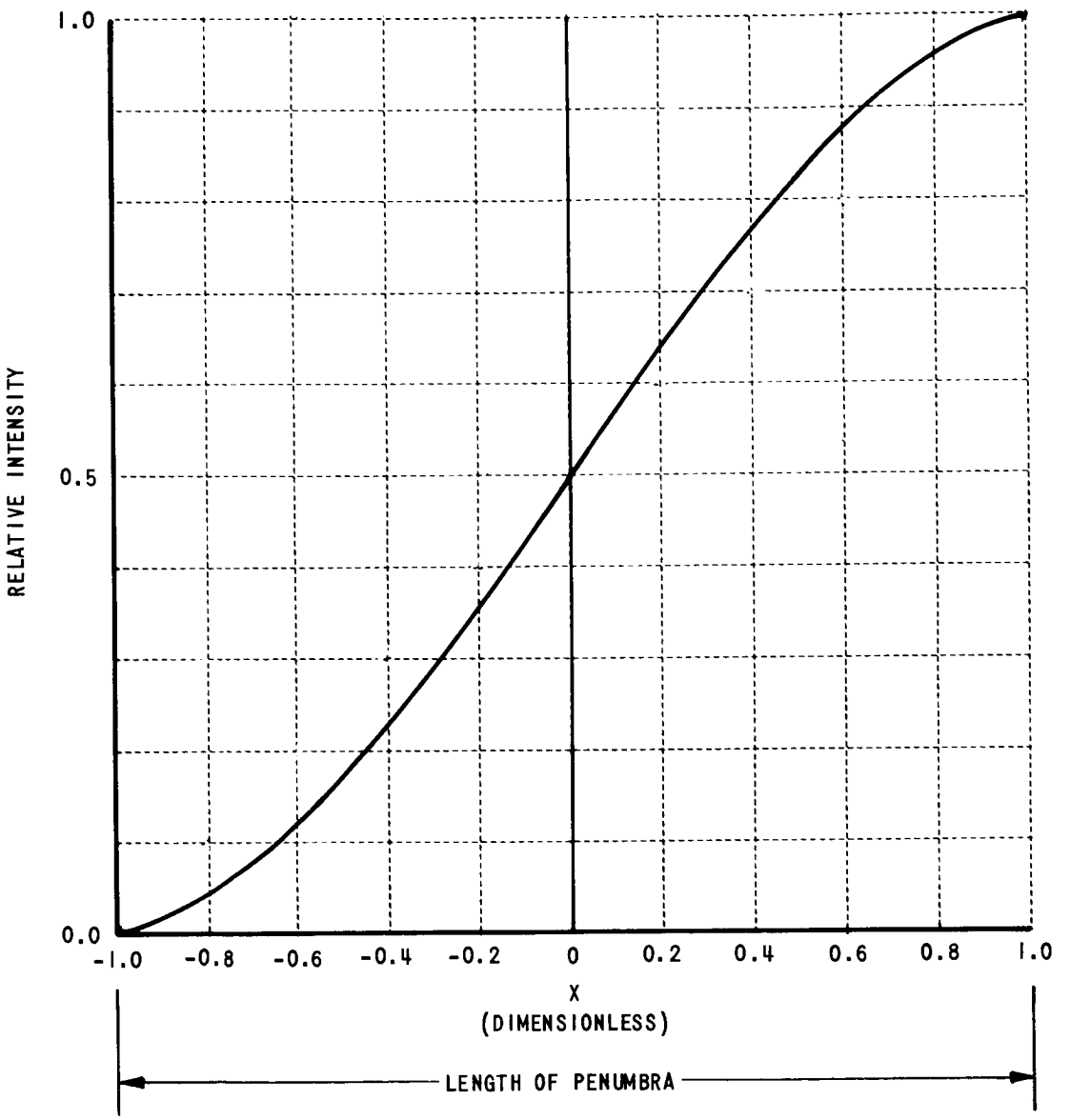

Figure 5 PENUMBRAL INTENSITY DISTRIBUTION

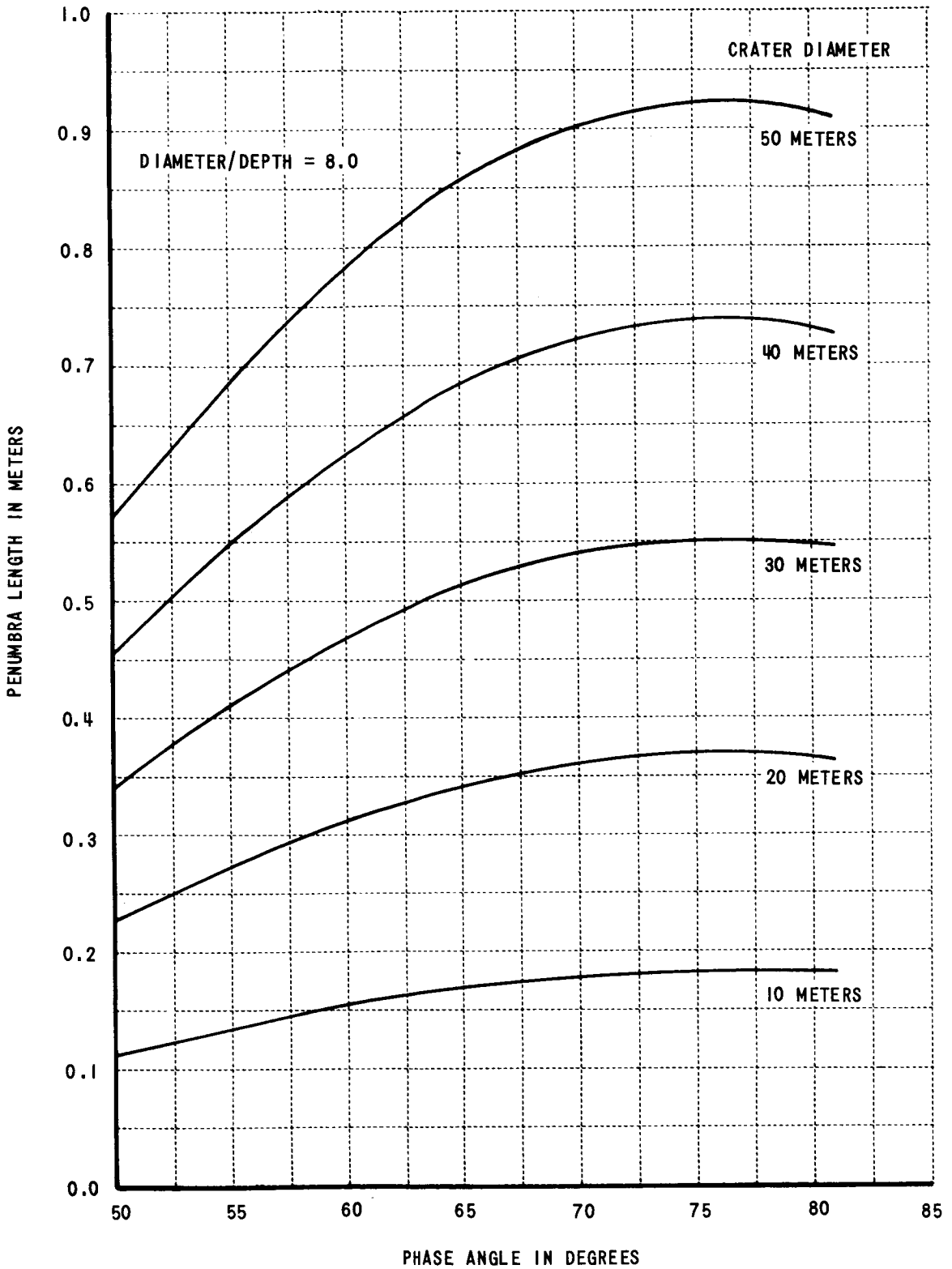

Figure 6 VARIATION OF PENUMBRA LENGTH IN THE PHASE PLANE

Based upon the above results, it can be concluded that selected shadow-to-sunlight edges will provide feasible targets for evaluation of detail rendition in various parts of the format. It should be noted that some limitations exist for the edges selected. If no image details are present in a large area of the format due to lack of significant topographic features or if phase angles are such as to eliminate shadows, then no targets will be available for evaluation. Such circumstances are unlikely under nominal operation of the Lunar Orbiter system. Although it may be possible that a small area in any one format could lack sufficient targets, this is obviously not a serious limitation. It is shown in Appendix B that the selected shadow-to-sunlight edges can be used to evaluate the system at orientations away from the phase plane through a range of ± 45 degrees. Beyond this range, the number of potential targets available will be limited.

2.1.2 Selection of Targets on SO-243 Film. - The edge data which is pre-exposed on the SO-243 film prior to loading into the spacecraft contains several potential targets (e.g., bar charts and edges) which may be used to evaluate the combination of the scanner-communications-GRS system. A sample of the edge data is shown in Figure 7. As seen from the figure, the targets in the pre-exposed edge data exist in at most three orientations to the film direction, 0°, 45°, and 90°. If the response in another direction is required, an interpolation procedure is necessary. A microdensitometer trace over the edge in density step No. 7 is also shown in Figure 7. The sharpness of this edge was tested by scanning the same edge on four frames of the sample SO-243 film supplied by NASA. The results are shown in Figure 8, as an MTF which would be characteristic of a degrading process producing the observed edge data on the SO-243, if the true edge had initially been perfectly sharp. There is no reason to expect this MTF to change with orientation. The bar charts were also scanned to obtain square wave modulation and the data reduced to MTF form.[4] The results of this procedure are also shown in Figure 8 for comparison. Considering the fact that the normalization of the bar chart

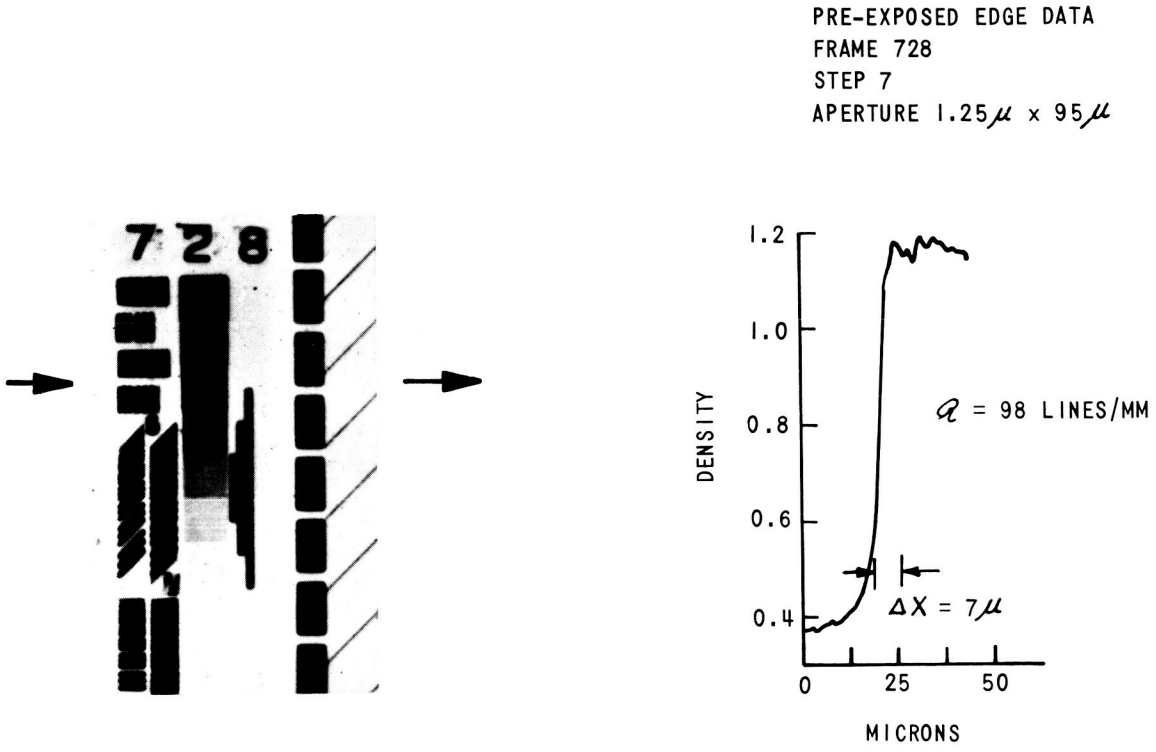

Figure 7 MICRODENSITOMETER TRACE OF THE 7TH DENSITY STEP ON THE SO-243 FILM

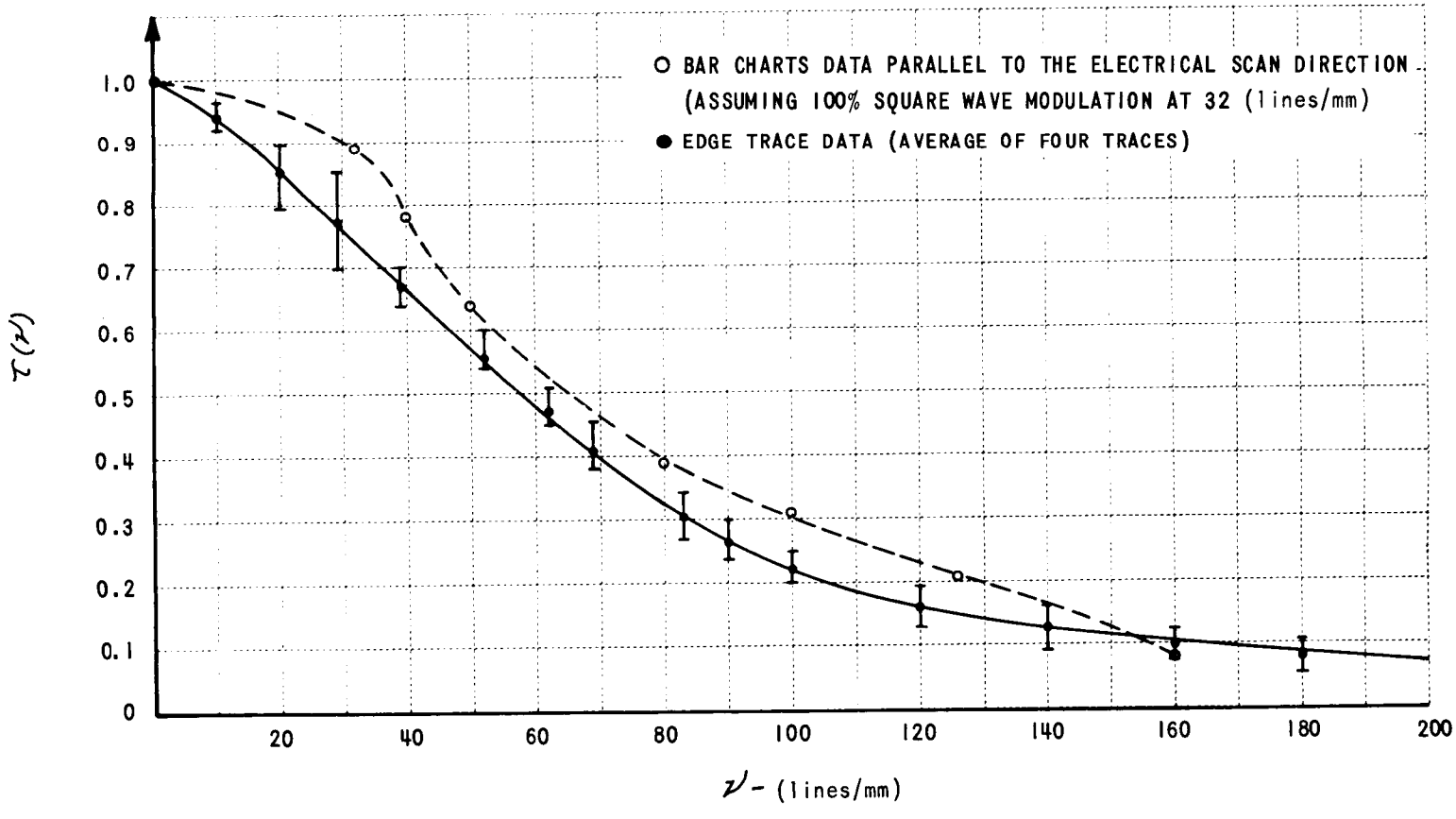

Figure 8 A COMPARISON OF MTF'S CALCULATED FROM THE EDGE DATA OF THE 7TH DENSITY STEP AND FROM THE BAR CHART DATA OF THE SO-243 FILM

response is not known exactly, the curves show good agreement between the two methods. For information in the orthogonal direction, a similar edge in that direction should be employed. It should be noted that edges between steps of the sensitometric wedge should be avoided, as they cannot be assumed to be sufficiently sharp.

There are sufficient test targets present in the SO-243 edge data for evaluation of detail rendition, at this element. The results in Figure 8 can be used to correct for the finite sharpness of these test targets when employing them to evaluate the frequency response of the combined scanner-communications-GRS system.

2.1.3 Data Extraction. - Once the targets have been selected, the problem becomes one of devising data reduction methods to extract the values of MTF for each of the groups of linear elements in the Lunar Orbiter system. The method described below can be used to evaluate the modulation transfer functions at various format positions and for various orientations; it is only necessary to employ input data appropriate to the case of interest. The selected edge target in the SO-243 pre-exposed data and the shadow edge on the lunar surface are used to provide inputs. Because the lunar shadow edge image is of high contrast, the non-linearity of the SO-243 film must be taken into account. Therefore, two separate modulation transfer functions are computed for the two linear segments of the system. The computations are shown in summary in the flow chart in Figure 9 and the equations used for the computations are discussed in Appendix C. The first step, shown starting from input 2 in Figure 9, is to obtain the MTF of the combined scanner-communications-GRS system. The edge in the pre-exposed SO-243 data array (comparable to the one shown in Figure 7) is scanned on the GRE film, using a microdensitometer with a scanning slit which is narrow with respect to the edge width (i.e., a slit width of less than 20μ). Since there is a linear relation between density on the GRE film and transmittance of the SO-243 film, no correction is needed. The edge trace is sampled and read into a digital computer, where the edge trace is smoothed by numerical filtering to remove noise

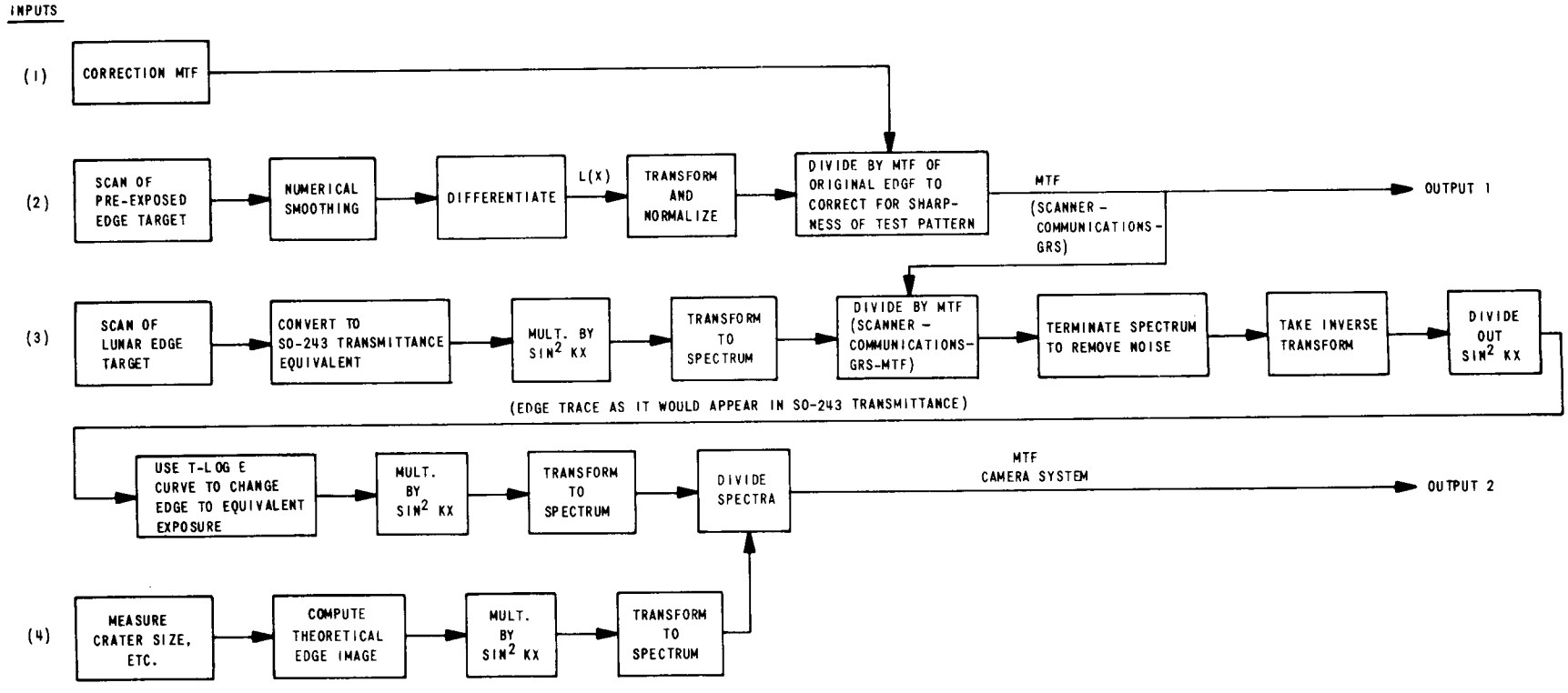

Figure 9 FLOW CHART OF EDGE TRACE DATA REDUCTION

and differentiated to obtain the line spread function.[2] The Fourier transform of the line spread function is computed and normalized to obtain a MTF. Finally, the computed MTF is divided by the MTF shown in Figure 8 to correct for the finite sharpness of the initial test edge in the pre-exposed edge data (input 1 of Figure 9).

The second operation, shown starting from input 3 in Figure 9, is to obtain the MTF of the camera system. This operation requires the use of the selected shadow edge on the lunar surface. The edge is scanned on the GRE film and sampled in the same manner used for the other edge just described. After these operations, several new features must be added to the calculations to correct for the MTF of the combined scanner-communications-GRS system, to account for the non-linearity of the SO-243 film, and to compensate for the high luminance side of the edge not being constant. The edge trace is first corrected from density on the GRE film to transmittance on the SO-243 film by use of the linear relation for signal gain discussed in the next section. The absolute transmittance values are necessary later to account for non-linear effects. To remove the MTF of the combined scanner-communications-GRS system, the Fourier spectrum of the edge must be found and divided by this MTF. Mathematical difficulties arise in attempting to obtain the Fourier spectrum of the edge trace in that termination of the edge trace by a sharp step introduces undesirable high frequencies in the spectrum and extension by extrapolation creates a function for which no spectrum is defined. A smooth decrease of the function to zero must be achieved at the ends of the sample interval. This is done by multiplying the function by $\sin^2 Kx$, where $x = 0$ is one end of the sampled interval of the edge trace, and $Kx = \pi$ is the other end of the interval. As discussed in Appendix C, this mathematical convenience has almost no effect on the spectrum, simply convolving it with a very narrow, smooth function. The complex Fourier spectrum of the edge function times $\sin^2 Kx$ is computed and divided by the MTF of the combined scanner-communications-GRS system. The resulting spectrum is terminated artifically at a frequency corresponding to about 100 lines/mm on the SO-243 film scale to reduce noise in the edge trace. The inverse

Fourier transform of the terminated spectrum is computed and the $\sin^2 Kx$ term is divided out to yield the edge trace as it must have appeared on the SO-243 film (in transmittance).

Next, the edge trace is converted from transmittance on the SO-243 film to relative exposure on the film by point to point transformation through the transmittance versus log exposure curve measured as described in the next section. The remaining step is to determine the MTF of the camera system. This is accomplished by dividing the Fourier spectrum of the edge trace measured in exposure by the spectrum of the ideal edge image. To obtain the Fourier spectrum of the edge trace, the same mathematical trick used before is repeated and the spectrum is computed. The ideal edge image is derived from the information given in the previous section on lunar targets. This derivation is shown starting from input 4 in Figure 9. If an appropriate crater was chosen, the penumbra length is small enough compared to the detail resolved that the finite penumbra can be assumed to be zero in length. The intensity beyond the penumbra is computed from equation (1), by measuring the appropriate crater dimensions. The spectrum of the ideal edge trace is computed in the same manner as the spectrum of the measured edge trace. The two spectra are divided to obtain the MTF of the camera system.

2.2 Signal Level Measurements. - The signal level is described by using the gain factors of the photographic system. These factors represent the conversion of aerial exposure to density on the SO-243 film and the conversion of density or transmittance on the SO-243 film to the corresponding density on the GRE film. These factors are used to determine the contrast of gross detail in the image and, in combination with the modulation transfer functions just described, the contrast of fine details. The gain factors are used for two purposes in the quality analysis. First, as mentioned in the previous section, they are needed in evaluating the modulation transfer functions of the system components. Second, they are used in evaluating image quality criteria, in combination with the modulation transfer functions described previously and noise measurements described in the next section.

The gain factors needed are those which relate: (1) transmittance of the SO-243 film to the camera exposure, (2) density of the GRE film to the transmittance of the SO-243 film, and (3) if copies of the GRE original film are used in analysis, the conversion from density of the copy to the density of the GRE original film. For applications where only low contrast objects are considered, or in cases where only gross detail is treated, only the gain relation between the final copy density and the original camera exposure is required. Because this is the simplest measurement to make, it is considered first.

A typical copy of a portion of the GRE original film is shown in Figure 10 (a). The sample is a first copy (and is therefore the same sense as the SO-243 film) and shows the area of the format containing the pre-exposed data array. The series of controlled exposure steps (log exposure changing 0.15 between steps) is scanned by a microdensitometer* and the measured density is plotted as a function of exposure as shown in Figure 10 (b). This curve provides the necessary signal level relation for the complete system.

To obtain the individual signal gain factors, additional information is necessary. If a copy of the GRE film has been used, as in the example above, it is necessary that the same series of density steps be scanned on the GRE original film and on the GRE copy film. A graph is then plotted relating density on the copy to density on the original film. There are no targets available to determine the gain of the system between the GRE film density and the transmittance SO-243 film. However, if all gain settings are recorded and available, it is possible to determine the relation between density on the GRE film and transmittance of the SO-243 film. This relation is shown in Figure 11 for nominal Lunar Orbiter system operating conditions. Finally, the transmittance of the SO-243 can be related to camera exposure by utilizing the data from graphs equivalent to those shown in Figures 10 (b) and 11.

---

* It is possible to use an ordinary densitometer if a small enough aperture is available, but the microdensitometer is more convenient.

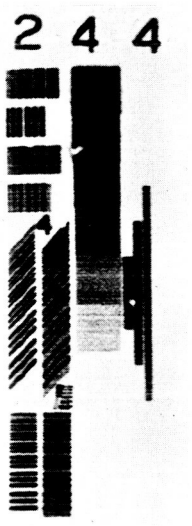

a) GRE COPY

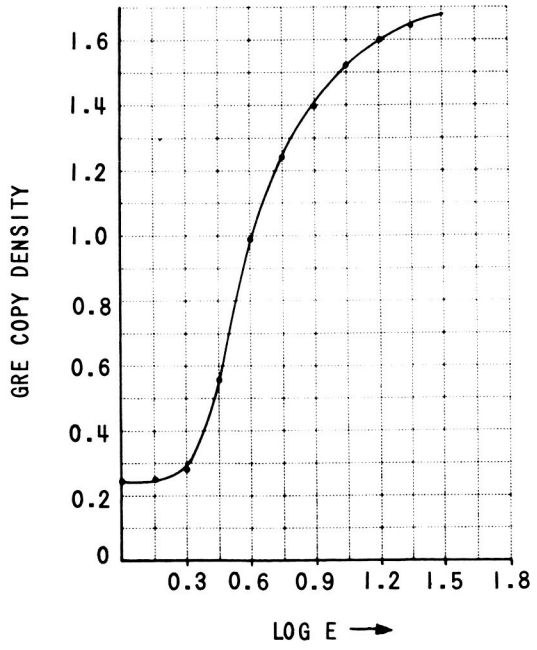

b) RELATION BETWEEN GRE COPY DENSITY AND ORIGINAL CAMERA EXPOSURE

Figure 10 SYSTEM SIGNAL LEVEL MEASUREMENTS

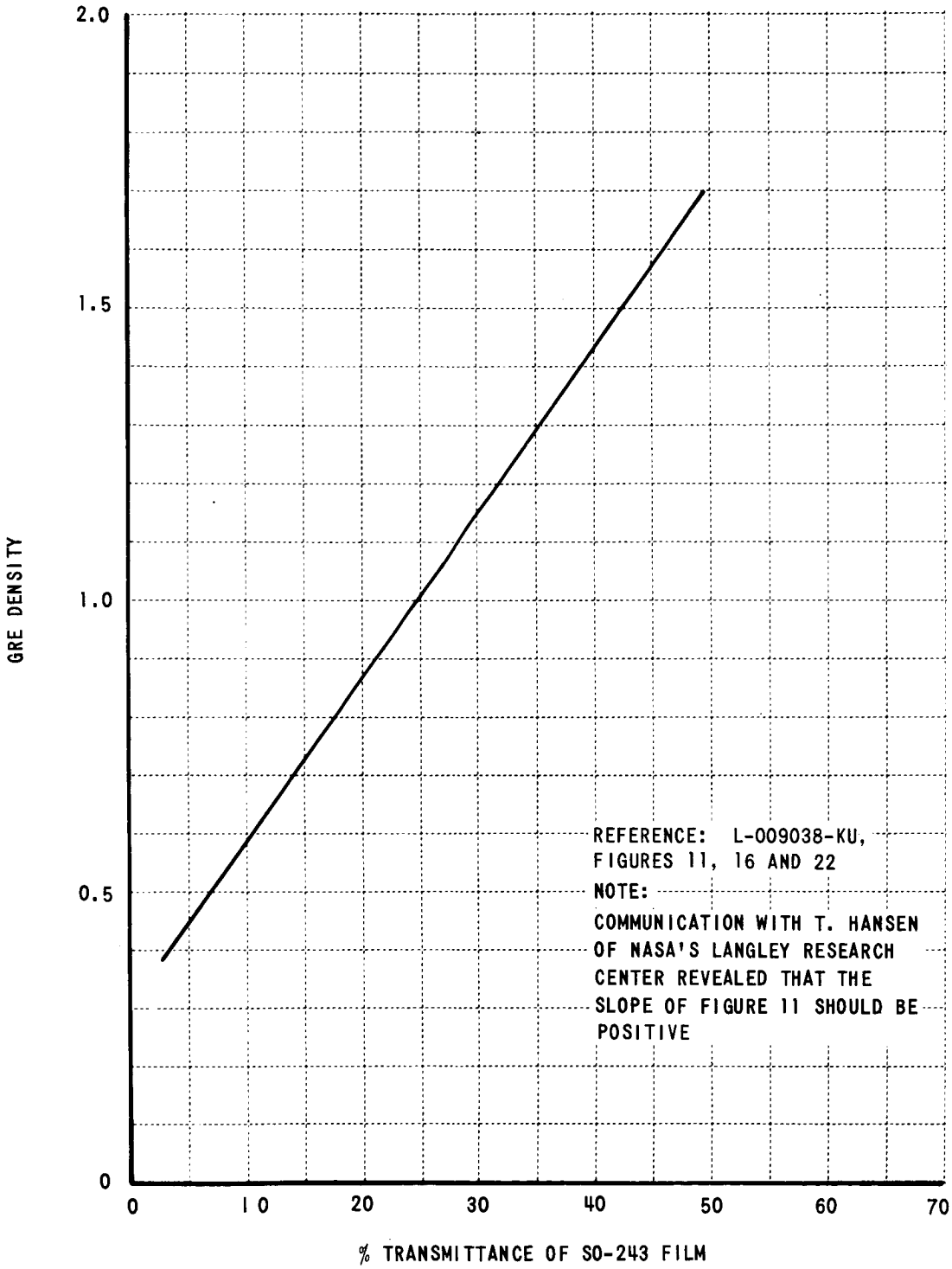

Figure 11 NOMINAL RELATIONSHIP BETWEEN TRANSMITTANCE ON THE SO-243 FILM AND THE DENSITY ON THE GRE ORIGINAL

In lieu of the above, as for example if some portion of the data are not available, a less reliable alternative approach is available for determining the individual gain factors. The transmittance of the SO-243 as a function of camera exposure can be determined for nominal operation by scanning the series of exposure steps directly on a sample of SO-243 film obtained, for example, during system checkout tests on the ground. Such a curve, obtained from the sample of SO-243 film supplied by NASA is shown in Figure 12. The system gain from the density on the GRE copy film to the transmittance of the SO-243 could potentially then be obtained by assuming nominal SO-243 development and combining curves similar to those shown in Figures 10 (b) and 12.

2.3 Noise Level Measurement. - Noise is contributed to the Lunar Orbiter images by a number of components, as shown in the block diagram in Figure 13. An analysis of these noise sources was conducted, using the nominal operation of the Lunar Orbiter, and typical noise spectra were derived for the complete system. The details of this analysis are presented in Appendix D, and a typical noise spectrum in two-dimensions and as would be measured by scanning the GRE film is shown in Figure 14. It can be seen that both the two-dimensional and the one-dimensional spectrum as measured by a point scan spot are almost completely contained within the bandwidth of interest (i.e., up to about 100 lines/mm scaled to the SO-243 film scale). The noise measure has been chosen to be the total noise power in this band converted to an equivalent noise power per unit bandwidth assuming a white noise spectrum.

The standard photographic test pattern for granularity or noise measurements is a uniformly exposed area of film. The series of controlled exposure steps (step wedge in the pre-exposed edge data) discussed in the previous section provide such targets. Moreover, it is not difficult to locate what appear to be reasonably uniformly exposed regions (i.e., lacking in detail) in lunar photographs such as those taken by Ranger spacecraft. Experience has shown [2] that, unless extreme care is taken to make the exposure uniform, however, that it is best to assume, in any case, that a small amount of low frequency signal is present. This

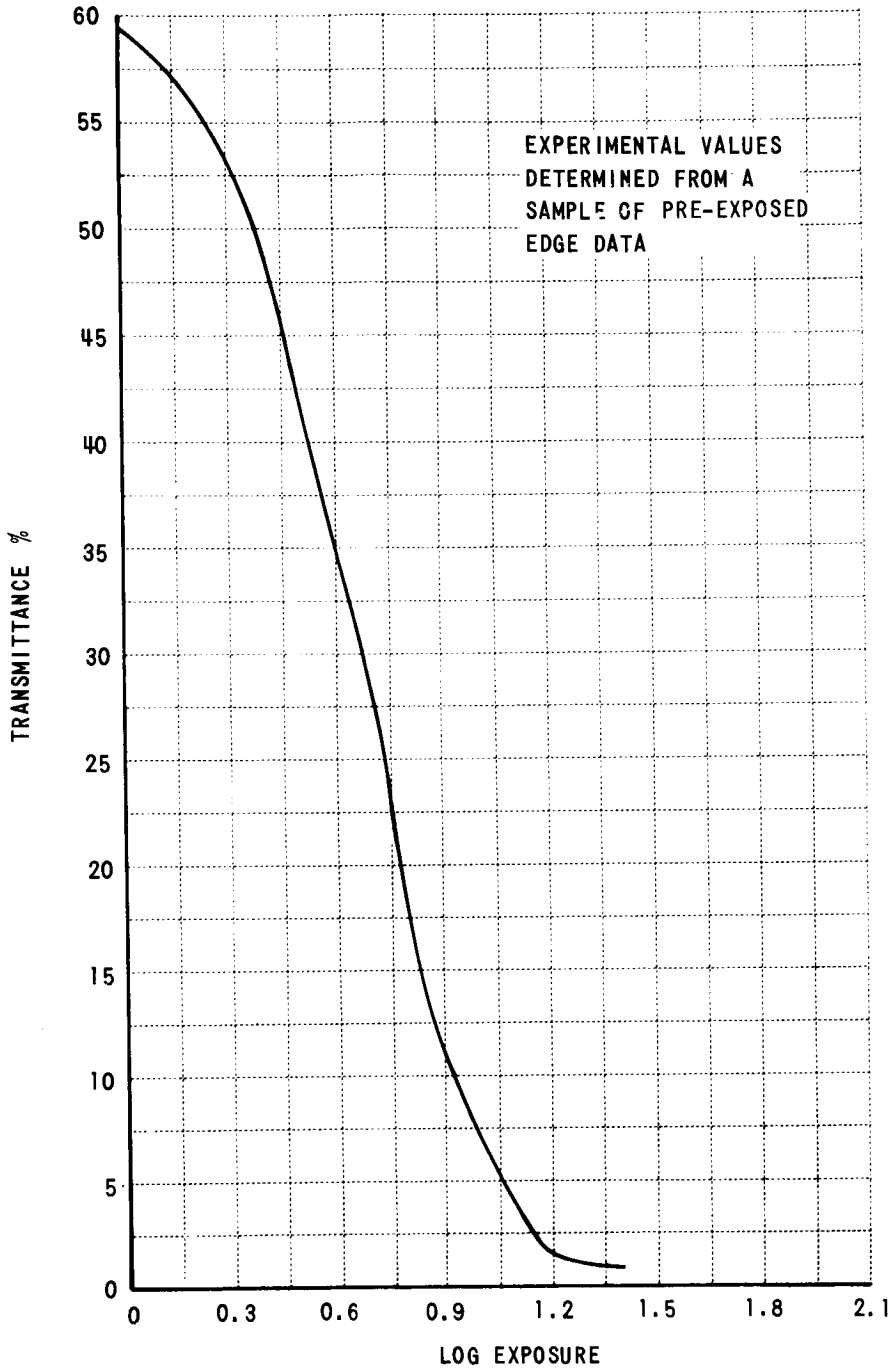

Figure 12 EXAMPLE OF RELATIONSHIP BETWEEN TRANSMITTANCE OF THE SO-243 AND THE LOG EXPOSURE

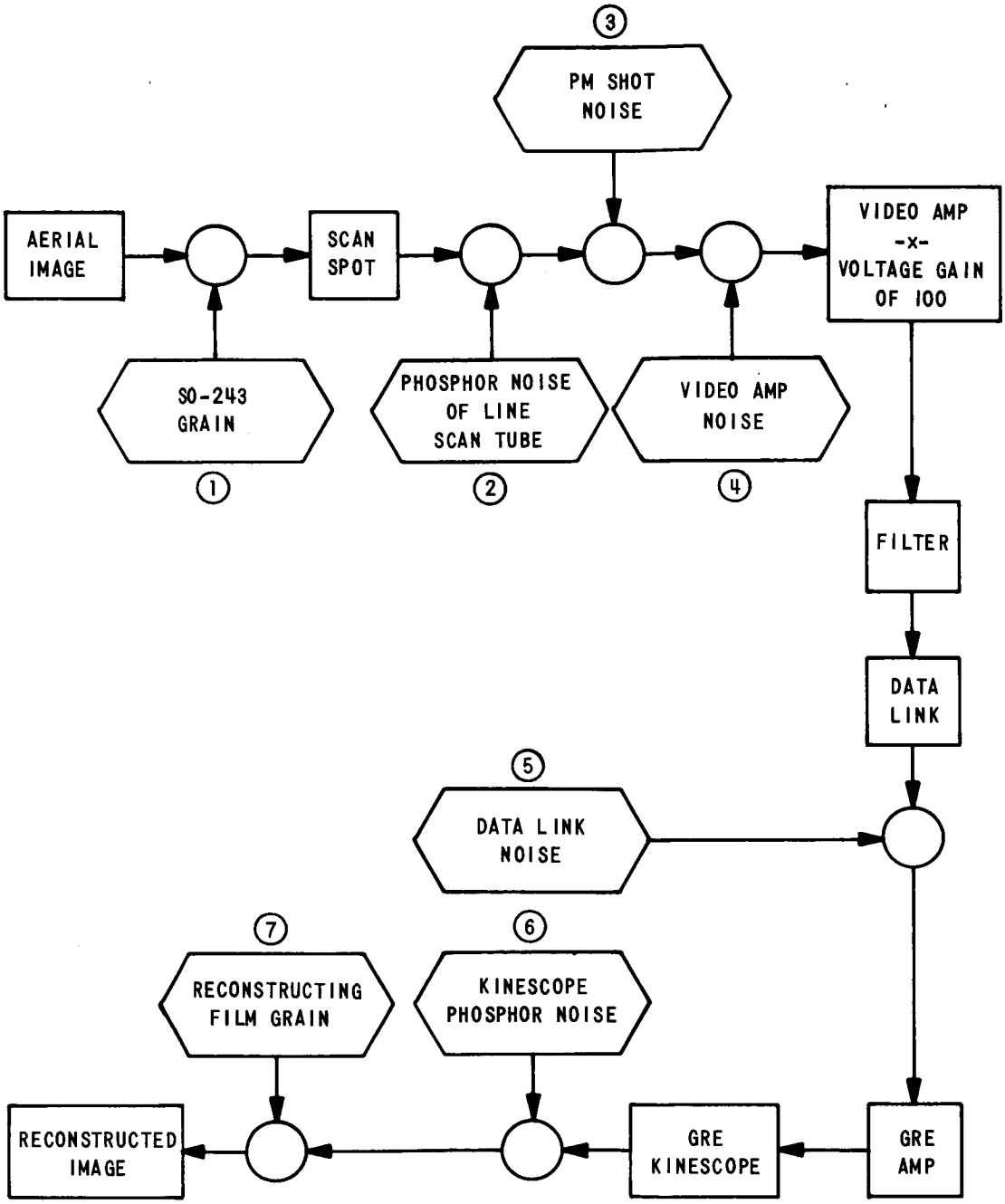

Figure 13 BLOCK DIAGRAM SHOWING NOISE COMPONENTS

CROSS-SECTION OF TWO-DIMENSIONAL SPECTRUM

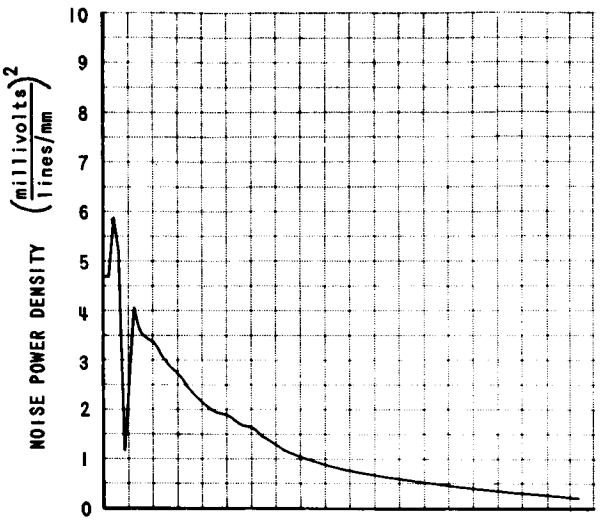

a) MECHANICAL SCAN DIRECTION

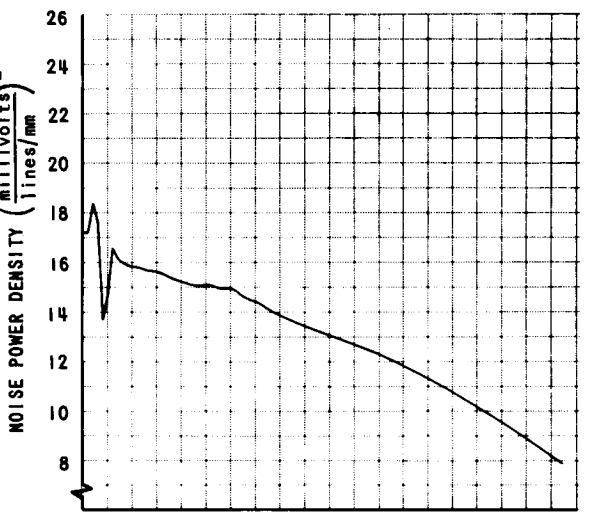

b) ELECTRICAL SCAN DIRECTION

ONE-DIMENSIONAL SPECTRUM

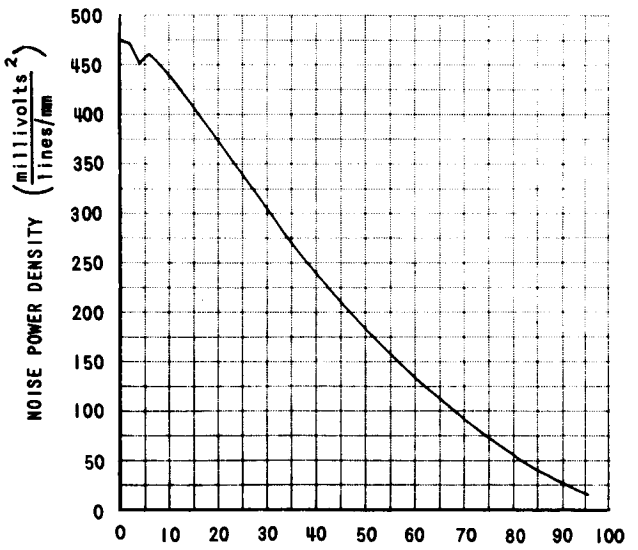

c) MECHANICAL SCAN DIRECTION

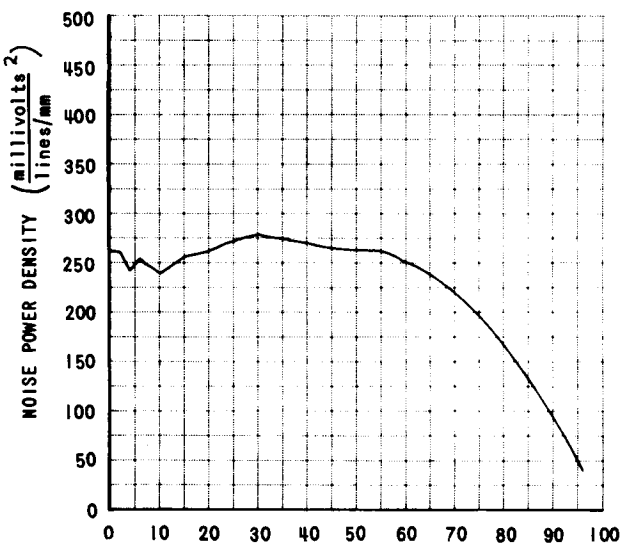

d) ELECTRICAL SCAN DIRECTION

Figure 14 TYPICAL NOISE SPECTRUM

assumption is made in the data reduction and then any target which looks uniform is acceptable for noise measurements. It is assumed that the noise measurements will be made both in the image area and on a controlled exposure step. The total noise power is shown in Appendix D to be a function of GRE film density level. Since the images of topographic features are of low contrast, the noise measurements are assumed to be made near the average image density.

The noise measurement is made by scanning the target with a microdensitometer with a relatively small aperture (i.e., a circular aperture about 25μ or less in diameter). A typical noise trace is shown in Figure 15. The density is read out digitally at a sample rate which yields one sample approximately every 33μ. This corresponds to a Nyquist frequency of 15 lines/mm, that is, noise frequencies up to 15 lines/mm are adequately sampled. This frequency is above the system resolution limit on the GRE film. Alternatively if one desires to eliminate the effects of the coherent noise (i.e., scan lines) when scanning perpendicular to the electrical scanning direction, the sample spacing can be chosen to be one sample per scan line or every 24.3 microns.

The sampled data are read into a computer and high-pass filtered to remove the effects of residual signal. The total noise power is computed by calculating the mean square density fluctuation and correcting for both the noise removed by the high-pass filter and that filtered by the microdensitometer aperture used.

A high-pass filter used in previous work[5] is applicable here. Its frequency response is given in Figure 16 for the 33μ sampling interval. If the sampling interval is decreased, the frequencies in Figure 16 are increased proportionally. The mean square density fluctuation or measured total noise power (σ_D^2) is computed in a straightforward manner. To correct for the high-pass filtering, σ_D^2 is multiplied by a factor equal to 2.12, where a spectrum shaped like that in Figure 14 is used to compute the correction.

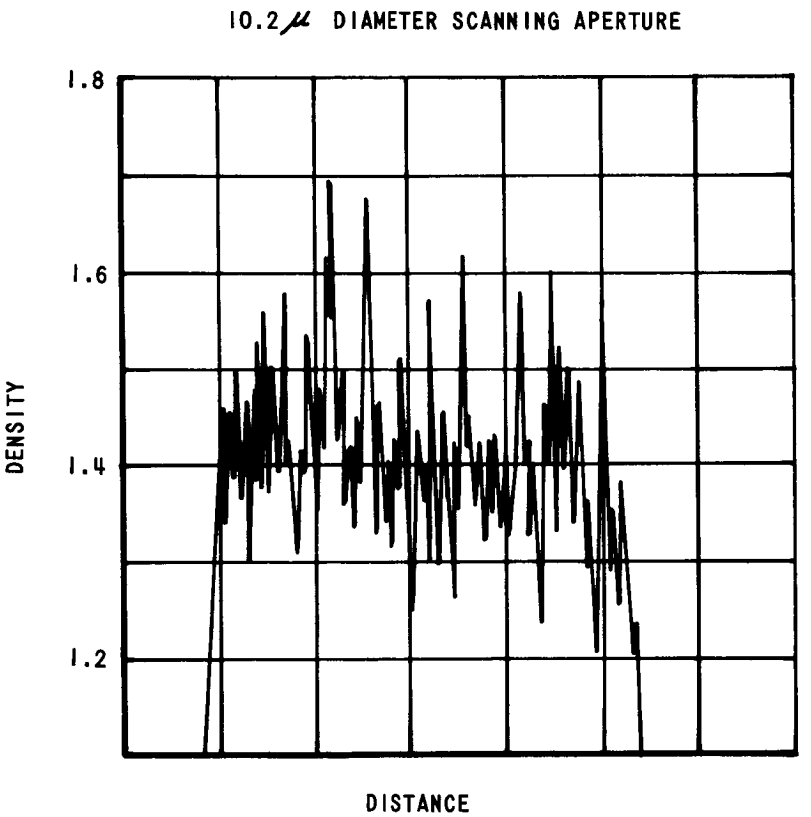

Figure 15 TYPICAL NOISE SCAN OF A UNIFORM GREY AREA ON THE GRE COPY FILM

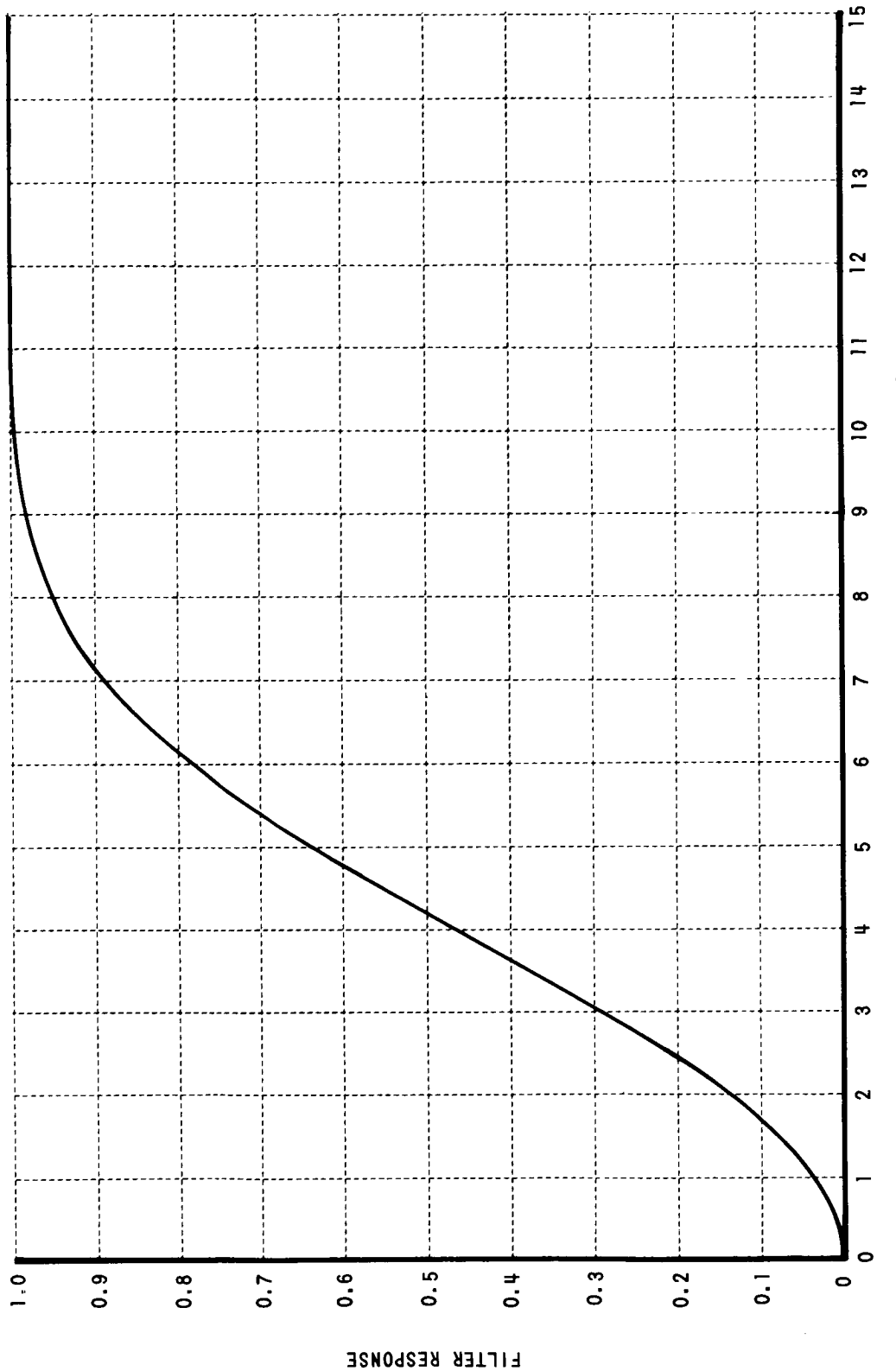

Figure 16 RESPONSE CURVE OF NUMERICAL FILTER

Finally, if the microdensitometer scanning aperture is taken to have a diameter less than 25μ, it has essentially no effect and requires no correction. The noise power, N_0 , per unit frequency cell in the two-dimensional spectrum is computed from:

$$N_0 = \frac{\sigma_{D1}^2}{(2\nu_R)^2} = \frac{\sigma_{D1}^2}{4(15)^2} \tag{2}$$

where σ_{D1}^2 is the mean square fluctuation corrected for the effects of the high pass filter, and ν_R is the signal bandwidth limit on the GRE film. The noise power per unit frequency, ψ , in the one-dimensional spectrum is calculated from N_0 by summing over the signal bandwidth in one dimension, that is,

$$\psi = 2(15)\, N_0 . \tag{3}$$

The value of ψ is the noise parameter used in the following sections for studies of extraction of topographic features, while N_0 is used for studies of detectability of obstacles.

3. RELATION OF QUALITY PARAMETERS TO LUNAR ORBITER OBJECTIVES

With quality parameters defined and measurement techniques available, it is significant to ask how the MTF, signal level, and noise level values affect the ability to detect and measure topographic features on the lunar surface. During an actual mission, the Lunar Orbiter spacecraft will photograph the lunar surface in the nadir direction. Variations in exposure on the SO-243 film are produced by the dependence of the reflectance of the surface upon the orientation of the lunar surface. The relative reflectance is expressed through the photometric function. This function depends upon the phase angle (the compliment of sun elevation) and the angle made by the projection of the normal to the surface in the phase plane and the optical axis of the camera system. Therefore, the density variations observed in the reconstructed photographs do not contain information concerning surface variations in a direction perpendicular to the phase plane. One objective of the Lunar Orbiter Mission is to measure the one-dimensional topographic profile in the phase plane. A topographic feature has been specified by NASA[6] for evaluation of the system in the performance of this task. This feature is a flat area, sloped from the horizontal for a given distance, surrounded by a horizontal area. If such a feature existed on the lunar surface its reconstructed image on the GRE film would be a degraded square upon a uniform background. The density difference between the image and the background depend upon various mission conditions such as phase angle, exposure time, etc. Because the resulting topographic data for this task is in the form of a one-dimensional profile, the analysis presented below assumes a one-dimensional profile model in the phase plane.

Another objective of the Lunar Orbiter Mission is to assess the general surface roughness. In order to perform this task one must be able to detect obstacles on the lunar surface. Again, a topographic feature has been specified by NASA[6] for evaluation of system performance. This feature is a right circular cone with a vertical axis and protruding from or recessed into a horizontal surface.

The capability for measuring slopes is considered below, followed by a description of the analysis of detection capability for conical obstacles. In both cases, the methods of statistical communication theory are used to evaluate the system capability. Possible combinations of performance criteria are then considered as a figure of merit for Lunar Orbiter photographs.

3.1 Measurement of Slopes. - The capability of using the Lunar Orbiter photographs to estimate slopes is related to the quality parameters by deriving expressions for the variances or the best estimates of the desired topographic measurements. A one-dimensional model is used, where the test feature is assumed to be horizontal everywhere except over a length, ℓ , where the slope is a constant value α_o as shown in Figure 17. The method of maximum likelihood estimation is used, and the variances in the measurement of α_o and ℓ are derived. These variances correspond to the minimum variance to be expected from an unbiased estimate and are therefore indicative of limiting performance, which may not be achieved in actual data reduction.

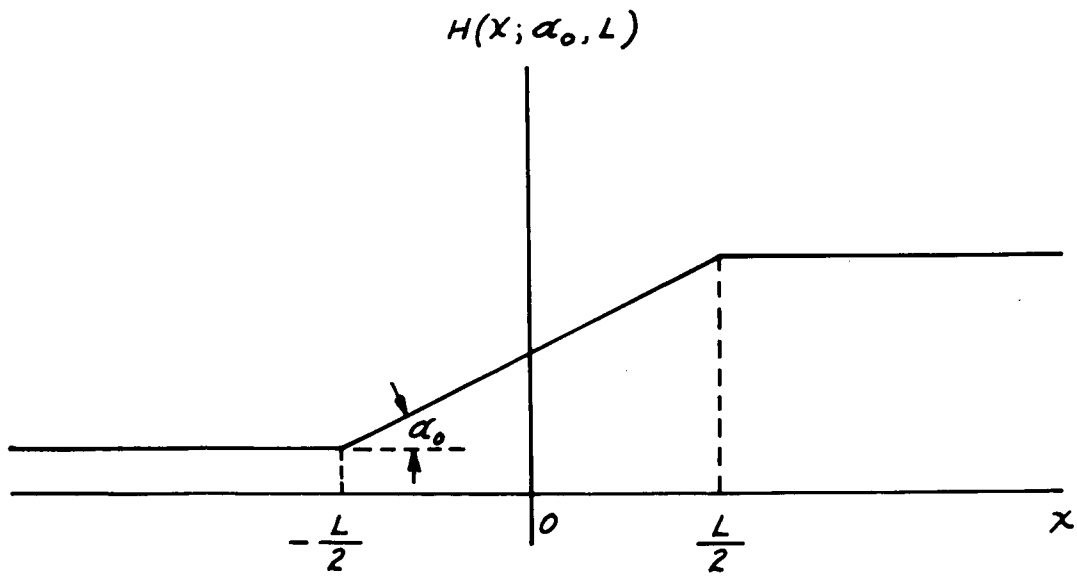

Figure 17 A TWO PARAMETER FAMILY OF TERRAIN PROFILES

The use of the method of maximum likelihood is discussed in Appendix E, where the variance equations are derived. The approach is to calculate the exposure on the SO-243 film for the assumed ramp function object by employing the photometric function. For the slopes of interest, the exposure due to the object is a low contrast rectangular function. Because the exposure function is of low contrast, the entire Lunar Orbiter system can be approximated as linear. Thus, the MTF of the combined scanner-communications-GRS system can be multiplied by the MTF of the camera system to obtain one system MTF, and the complete system gain function represents the gain factor needed.

The variances in the measures of slope angle, α_o , and length, ℓ , are given respectively by:

$$\sigma_\alpha^2 = \frac{A_{22}}{A_{11} A_{22} - A_{12}^2}$$

$$\sigma_\ell^2 = \frac{A_{11}}{A_{11} A_{22} - A_{12}^2} \qquad (4)$$

where:

$$A_{11} = \frac{2}{\psi}\left(\frac{\partial D}{\partial \alpha}\right)^2 \int_0^\ell (\ell - \xi)\, \phi_L(\xi)\, d\xi$$

$$A_{22} = \frac{(\Delta D)^2}{2\psi}\left[\phi_L(0) + \phi_L(\ell)\right] \qquad (5)$$

$$A_{12} = \frac{\Delta D}{\psi}\left(\frac{\partial D}{\partial \alpha}\right)\int_0^\ell \phi_L(\xi)\, d\xi$$

and ψ is the noise power per unit spatial frequency, D is the density of the target and Δ D is the change in density on the GRE film from background to target for a perfect system, and ϕ_L is the autocorrelation of the line spread function. ϕ_L may be obtained by taking the Fourier transform of the square of the MTF of the entire system.

Equations 4 and 5 relate the quality measures, that is MTF, signal level, and noise level, to the ability to measure slopes on the lunar surface; as expressed by the variances in slope angle and length. Several features of these relations can be noted. First, σ_α^2 and σ_ℓ^2 are both directly proportional to ψ , the noise level. The signal level enters implicity, in the relation of density, D , to aerial

exposure. This relation is such that both σ_α and σ_ℓ are inversely proportional to signal level. Finally, the relation to MTF through the function $\phi_L(\xi)$ is complicated, but it is interesting to note that $\phi_L(0)$ is not only the maximum value of $\phi_L(\xi)$, but is also the well known quality parameter, Schade's equivalent passband. If the length, ℓ, of the slope is taken to be long compared to the system spread function, the integrals in Equation 5 can be evaluated and limiting forms obtained. It is found that the variance in α_o becomes independent of the system MTF and is inversely proportional to ℓ, as expected. The variance in the measurement of ℓ becomes independent of ℓ and is inversely proportional to Schade's passband value. Examples of the evaluation of σ_α and σ_ℓ for various combinations of quality parameters are given in a later section of the report.

3.2 Detection of Obstacles. - The analysis of the ability to detect obstacles proceeds in a manner which is closely analogous to that used in the previous discussion of measurement of slopes. In the case of detection, the test object is chosen to be a specified conical obstruction of height, h, and radius, r. The phase angles are assumed to be chosen so that no shadow is cast by the obstacle. The presence of a shadow enhances the ability to detect a cone object, and therefore, the measure determined with no shadow present represents an upper found on the error probability. As in the previous analysis, the object is low contrast, so the system is approximated by a linear system. However, the detection analysis must necessarily be treated in two dimensions.

Since the question is one of detection, the visual detection process is simulated for purposes of analysis by a matched filter designed for the specified size and shape of the obstacle. Although this matched filter is not applicable to detecting general obstacles from an actual photograph, it is useful in establishing a measure of system performance. This filter is used to make a decision in the optimum manner as to whether an obstacle is present or only a noisy background is observed. Following the previous approach, the signal to be expected for cones of interest is calculated, and the measure

of system performance is taken to be the minimum average probable error in deciding whether conical obstruction is present, that is, equally weighting errors of missing detection or of falsely detecting an obstruction. By extension of one dimensional analyses to two dimensions, as discussed in Appendix F, the minimum average error probability, P_e , can be written as:

$$P_e = 1 - \text{erf}\sqrt{\frac{Q}{4N_0}} \tag{6}$$

where N_0 is the two dimensional noise power density as measured in Section 2.3. The quantity, Q, is called the "quadratic content", and is evaluated by computing the difference in the noise free signals expected with and without the obstruction present, squaring, and integrating over the area where the two signals differ. It should be noted that Q will depend on the MTF of the system and the signal level. However, because of the integration over the signal, the value of Q does not depend uniquely on target shape. It is, therefore, reasonable that an approach which defines a more simply shaped, "equivalent" target, such as a bar chart, might be employed. The approach taken here, however, is a straightforward evaluation of Q, and therefore of P_e , by evaluating the appropriate integrals.

The value of Q can be written in terms of the autocorrelation function of the system point spread*, $\phi_p(x,y)$, and the autocorrelation function of the difference between the signals expected from a perfect system, with and without the conical obstacle present, $\phi_\Delta(x,y)$ as:

$$Q = \iint_{-\infty}^{\infty} \phi_\Delta(x,y)\, \phi_p(x,y)\, dx\, dy . \tag{7}$$

The derivation of this form for Q is given in Appendix F.

* The point spread is the Fourier transform of the two dimensional MTF.

3.3 Suggested Figure of Merit. - Previous sections have been concerned with the evaluation of the ability to extract topographic information, that is, measure slopes and detect obstacles on the lunar surface, from Lunar Orbiter photographs. Three system performance criteria, namely, the variance in slope angle measurements, σ_α , the variance in slope length measurements, σ_ℓ , and the minimum average error probability in detecting conical obstacles, P_e , were defined and related to measureable quality parameters of the Lunar Orbiter photographs. To obtain a single "figure of merit" for the system, the three criteria, σ_α, σ_ℓ and P_e must be combined in some manner, weighting each relative to the importance of performing that task from Lunar Orbiter photographs.

Two specific tasks have been defined for evaluation purposes, namely:

(1) Measurement of the slope of an area 7 x 7 meters inclined nominally 7° from horizontal within $\pm 2^\circ$, and

(2) Detection of conical obstacles 1/2 meter high, with base diameters from 2 to 7 meters.

These specific tasks are essentially the reason for choosing the more general criteria of shape measurement and obstacle detection for which σ_α, σ_ℓ and P_e were defined. Assuming that inclination angle measurement is the primary task, a figure of merit, FM , could be defined as:

$$FM_1 = \frac{1}{\sigma_\alpha} \qquad for \quad \begin{cases} \alpha^\circ = 7 \\ \ell = 7 \text{ meters} \end{cases} \tag{8}$$

If, however, the primary task is considered to be determination of topographic profiles, the relative height at one point with respect to another is important, and the probable error in height should be evaluated. In terms of measurements of α and ℓ , as before, and assuming independence of these measurements, the variance in height estimation is:

$$\sigma_h^2 = (\tan^2\alpha)\,\sigma_\ell^2 + \ell^2(\sec^2\alpha)^2\sigma_\alpha^2 \tag{9}$$

where σ_α is measured in radians, and a possible figure of merit would be:

$$FM_2 = \frac{1}{\sigma_h} \qquad for \begin{cases} \alpha = 7^\circ \\ \ell = 7 \text{ meters} \end{cases} \tag{10}$$

This figure of merit will be found to be more sensitive to system MTF than FM_1, because of its dependence upon σ_ℓ.

Assuming detection of obstacles is most important, a reasonable figure of merit would be:

$$FM_3 = 1 - P_e \tag{11}$$

where P_e is evaluated for 1/2 meter high, 2 meter base cones. This figure of merit would give the probability of correctly deciding whether a conical obstacle was present.

Clearly, other possible figures of merit could be generated by altering the values of the parameters (slope angle, length, and cone size) or comparing the figure of merit measured for the actual system to the same figure of merit evaluated for the nominal system. Such comparisons would be most useful in judging the effect of off nominal performance created by operational degradations or system failures. In addition, the figures of merit discussed above have not included the effects of variations in performance with format position and orientation. All of the performance criteria can be evaluated at various positions and orientation. Therefore, a single figure of merit can also be an average over these factors.

Thus, the final choice of a figure of merit must be based on the user's weighting of relative importance of the various tasks, where the measures of performance can be obtained from the factors σ_α, σ_ℓ and P_e.

4. EXAMPLES OF THE USE OF THE MEASURING TECHNIQUES AND SYSTEM PERFORMANCE CRITERIA

The previous sections have defined a set of quality measures, measurement techniques, and mathematical relationships needed to reduce the measured data. The quality measures have been related to specific Lunar Orbiter tasks through system performance criteria. In this section, examples of the use of these concepts are given. The measurement techniques and data reduction processes are demonstrated to the extent possible by using Ranger photographs as a simulation of Lunar Orbiter results. The relation between system performance criteria and nominal and off-nominal conditions of Lunar Orbiter system operation is demonstrated by theoretical evaluation.

In Section 4.1, the measurement techniques are applied to Ranger photographs. A cursory experiment was first conducted to determine whether a change in MTF occurred with orientation, and to demonstrate the ability to scan crater shadow edges at various orientations. The precision of the measurement and data reduction techniques, when applied to lunar photographs, was then demonstrated by a second experiment. Since the actual MTF of the original Ranger photographic system was not known, the Ranger photographs were used as controls and a known function was obtained by generating degraded copies with image motion and defocus in the copy process. The MTF of the copy and the original could be measured and compared to determine whether the MTF of the known degradation was obtained.

Section 4.2 considers the variations of the system performance criteria, σ_{α} and σ_{ℓ} for nominal and off-nominal conditions. The Lunar Orbiter system is simulated employing operational degradations and various mission conditions. Evaluations of the system performance criteria under these conditions demonstrate graphically the variation of these measures for off-nominal conditions.

4.1 Demonstration of Measurement Techniques. - Copies of Ranger 7, 8, and 9 mission film were available for use in experiments. To obtain phase angles in the range of Mission A of the Lunar Orbiter (i.e., 60^{o} to 80^{o}), it was found that the lowest altitude (and therefore highest ground resolution) photographs could not be used. Instead, photographs were selected from the RA-9 series, with scales between $1:1 \times 10^{6}$ and $1:4 \times 10^{6}$. Except for differences in ground resolution, it was assumed that these photographs would provide a reasonable simulation of expected Lunar Orbiter output GRE film.

A crater image was selected on frame 436 of the RA-9 series, and the shadow-to-sunlight edge was scanned to obtain an MTF. Scans were made perpendicular to the edge at three locations, thus employing three different orientations with respect to the phase plane. The phase plane is oriented approximately 20^{o} from the perpendicular to the electrical scan lines, and the microdensitometer scans were made approximately -55^{o}, 30^{o}, and 60^{o} from the phase plane. Figure 18 shows the derived MTF's for the three orientations. The MTF appears to be essentially independent of orientation over this range of angles. It should be noted that sensitometric data were not available, hence corrections were not made in the analysis for non-constant light intensity beyond the shadow, characteristic of this edge (see Section 2.1.1). The results confirm that it is reasonable to expect that measurements can be made over a range of orientations of $\pm 45^{o}$ from the phase plane.

Frame 1220 of the RA-9 series was selected as an original transparency to generate degraded copies with image motion and defocus. To generate image motion, the original was imaged on the copy through a mirror system in which one mirror was translated by a drive motor during the exposure. Introduction of defocus was done in a straightforward manner. All exposures were equalized by use of neutral density filters, all images were recorded on Plus-X film, and all were developed identically. The original photograph, from the P1 camera, frame 1220, is shown in (a) of both Figure 19 and Figure 20. A typical copy with image motion introduced is shown in Figure 19 (b) and a defocused copy is shown in Figure 20 (b).

a) RANGER 9 PHOTOGRAPH

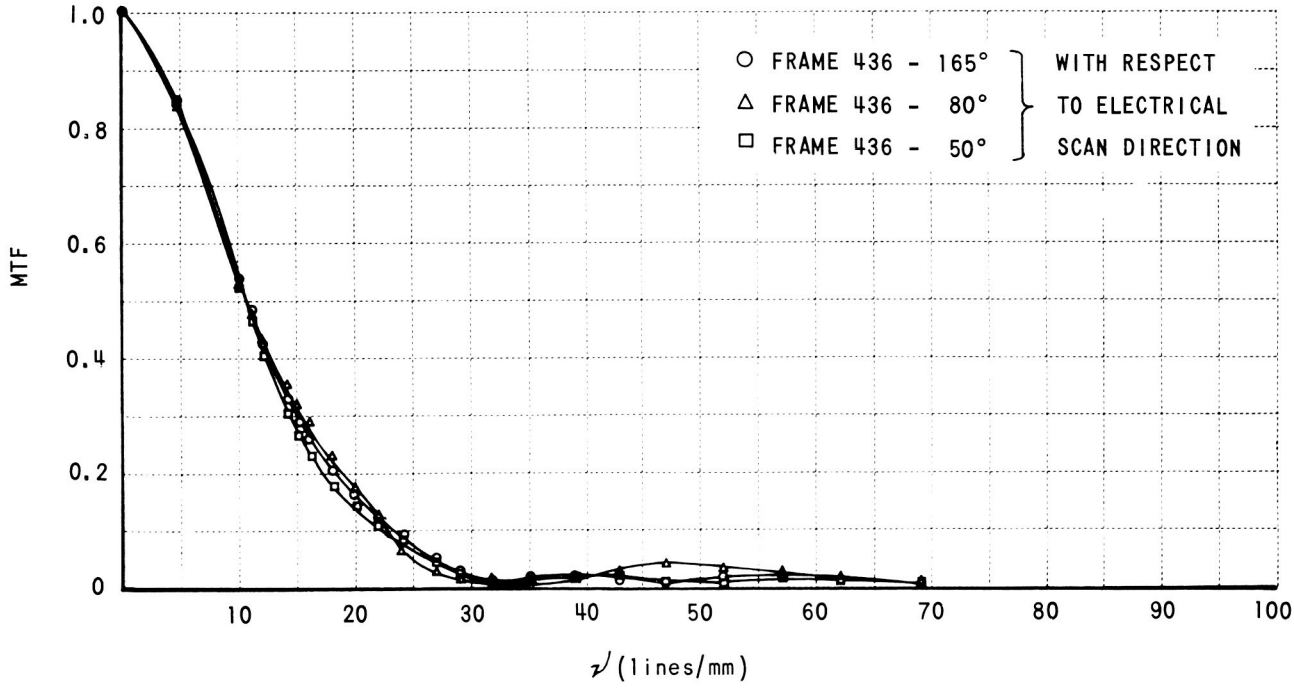

b) DERIVED MTF FROM VARIOUS ORIENTATIONAL SCANS

Figure 18 A COMPARISON OF VARIOUS MTF'S DERIVED FROM THREE ORIENTATIONAL SCANS ACROSS THE CRATER'S SHADOW EDGE OF FRAME 436 OF THE RANGER 9 PHOTOGRAPHS

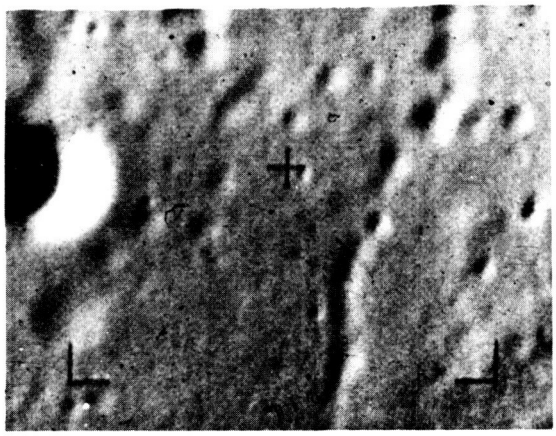

a) ORIGINAL PHOTOGRAPH (FROM PI CAMERA OF 1220)

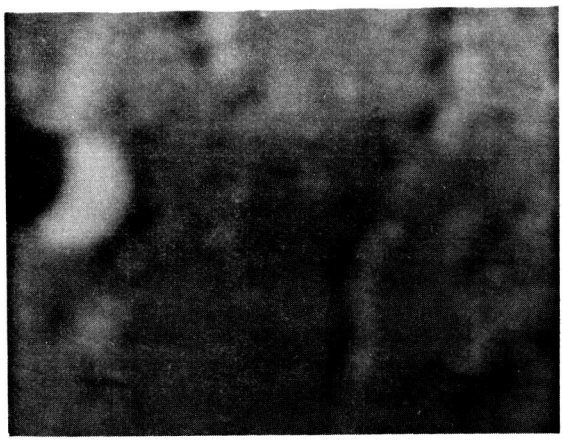

b) TYPICAL IMAGE MOTION PHOTOGRAPH

RATIO OF THE AMOUNT OF IMAGE MOTION TO RESOLUTION ELEMENT OF ORIGINAL = 2.2

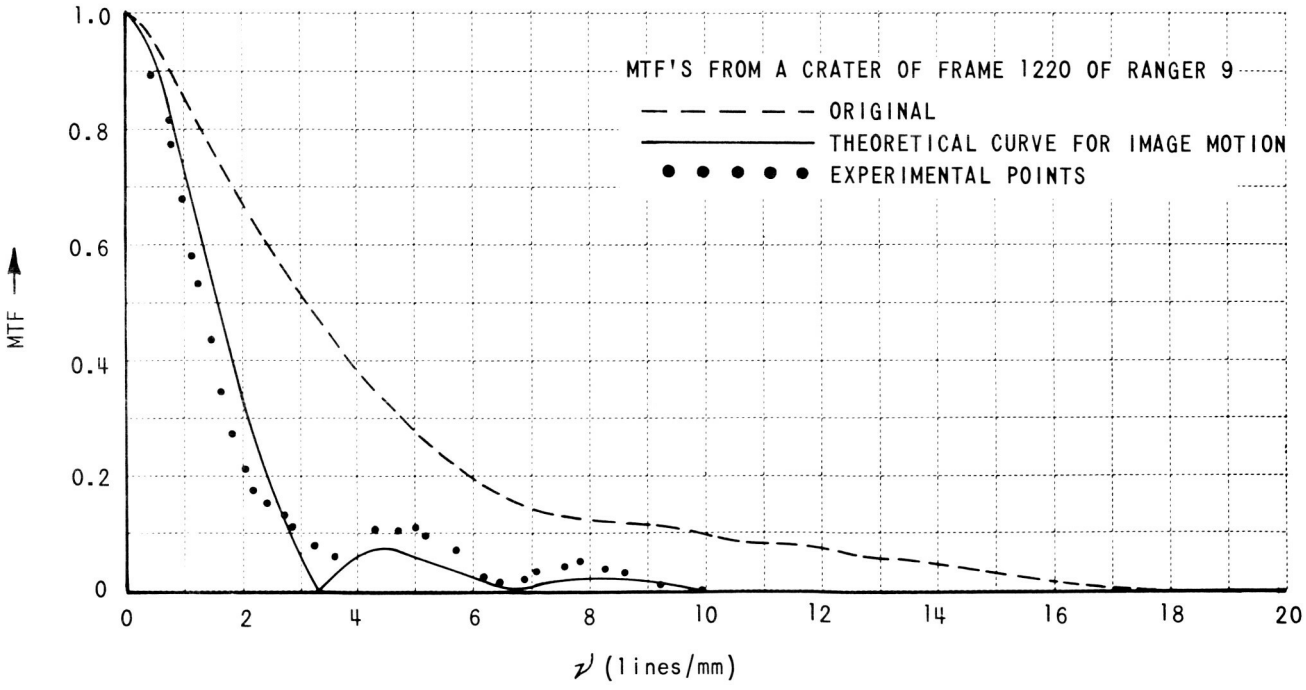

c) DERIVED MTF OF THE IMAGE MOTION TRANSPARENCIES

Figure 19 ANALYSIS OF INDUCED IMAGE MOTION IN THE RANGER 9 PHOTOGRAPHS

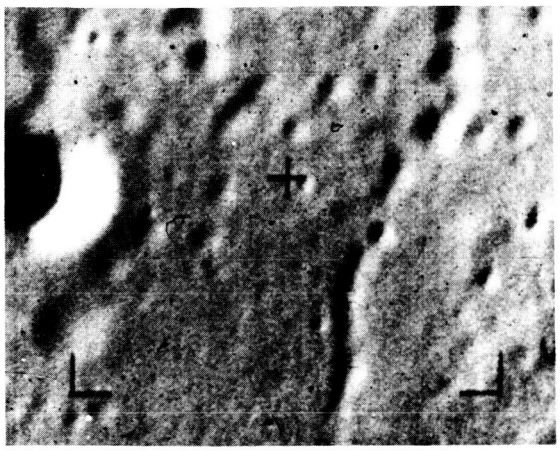

a) ORIGINAL PHOTOGRAPH (FROM PI CAMERA OF FRAME 1220)

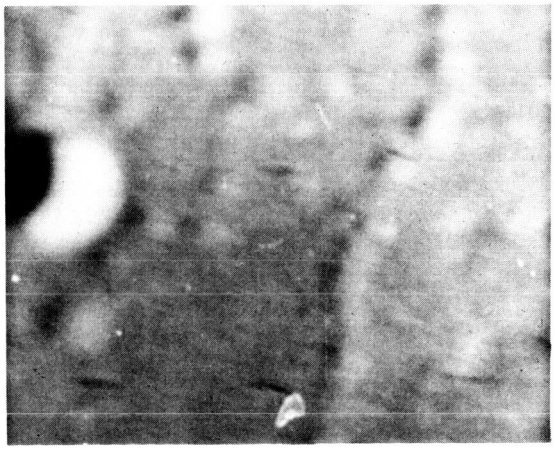

b)TYPICAL DEFOCUSED PHOTOGRAPH

RATIO OF THE AMOUNT OF DEFOCUS TO RESOLUTION ELEMENT OF THE ORIGINAL = 1.7

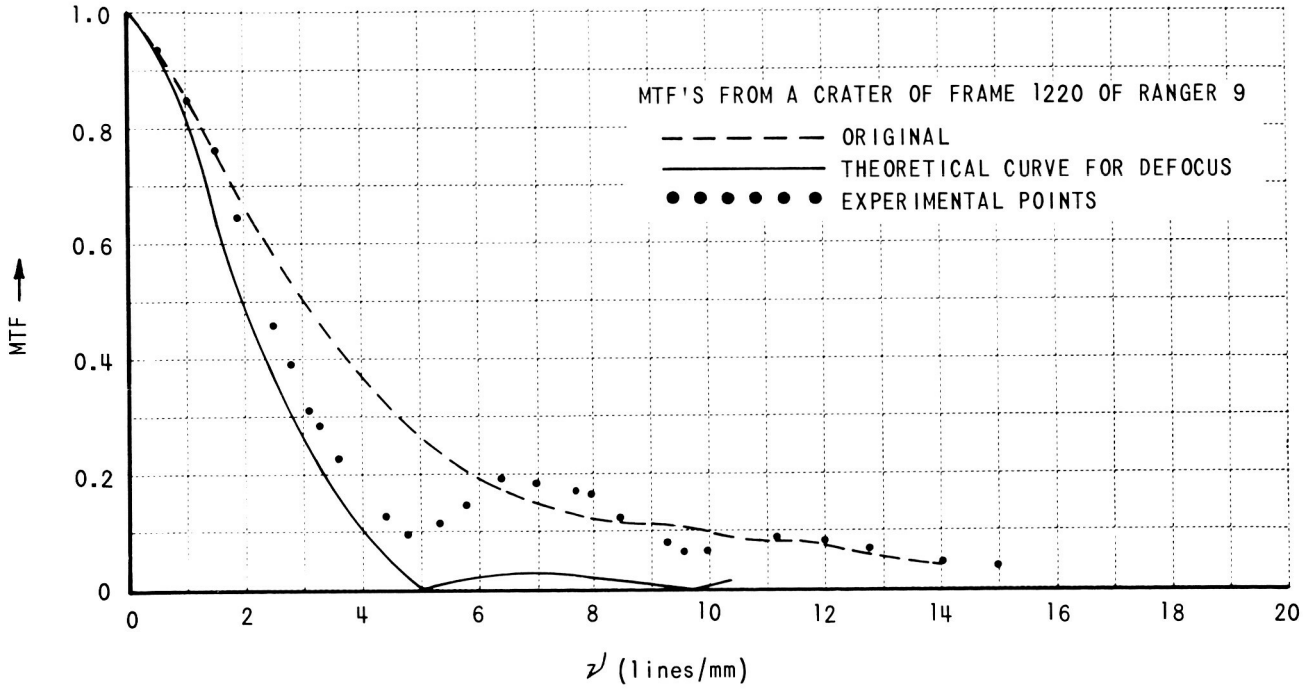

c) DERIVED MTF'S OF THE DEFOCUSED TRANSPARENCIES

Figure 20 ANALYSIS OF INDUCED DEFOCUS IN THE RANGER 9 PHOTOGRAPHS

As before, a sunlight-to-shadow edge inside a crater was selected as a test target, and the same edge was scanned on the original photograph and on each copy. Again, without sensitometric data, the non-constant intensity beyond the edge was not taken into account in deriving the degrading modulation transfer functions. The MTF of the original photograph is shown as a dashed line in Figure 19 (c) and 20 (c). The dotted lines in Figure 19 (c) shows the measured MTF of the motion degraded copy, while the dotted lines in Figure 20 (c) correspond to the measured MTF for the defocused copy.

To illustrate the level of precision achievable in measurement and data reduction, the measured MTF of each degraded copy can be compared to the theoretically expected MTF calculated from the MTF of the original and that of the degrading process. The amount of motion or defocus must be determined. In each case, approximate values were available from the parameters of the copy process. However, the well defined zero locations of the measured modulation transfer functions provide much more accurate estimates of the magnitude of the degradation and, in each case, the answer derived in this manner falls within the error in the calculated values taken from experimental parameters. Knowing the magnitude of the degradations, the solid curves in Figures 19 (c) and 20 (c) are derived by multiplying the measured MTF of the original photograph by the theoretical MTF of the degrading process.

Good agreement can be seen between the measured and computed MTF for each degraded photograph. The gradual increase of the measured values above the computed values at high frequencies can probably be attributed to the non-constant density on the sunlit side of the edge, which was not taken into account. The variation in density in this region is clearly seen in the trace shown in Figure 21, and as more of the non-constant portion of the density trace is included, the discrepancy in the results becomes worse. The analysis methods suggested in Section 2 will correct for this effect, but requires sensitometric data which was not available for Ranger photographs, but will be a part of the Lunar Orbiter data.

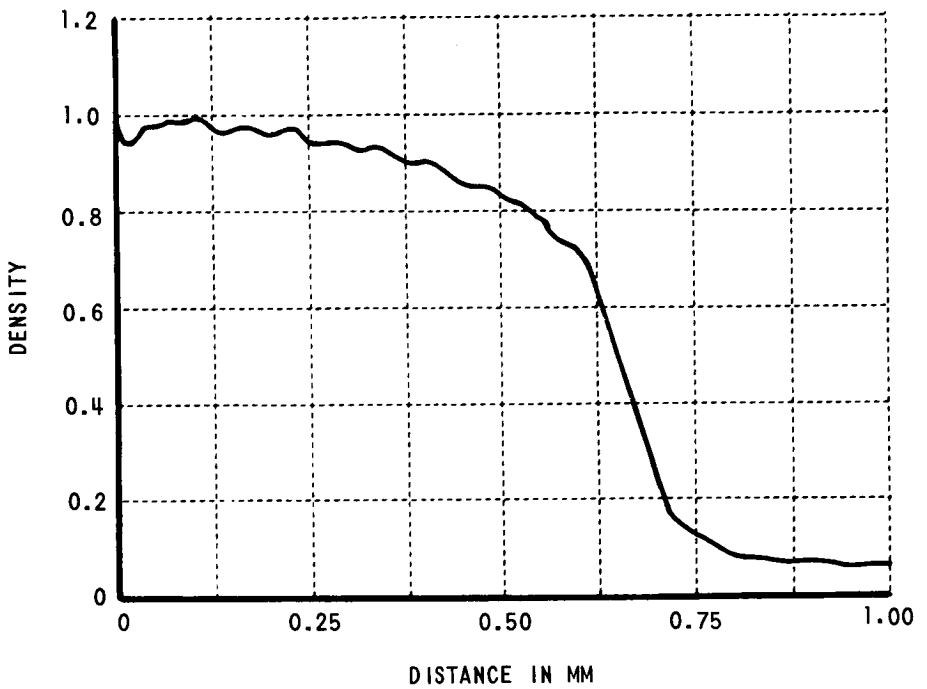

Figure 21 TYPICAL MICRODENSITOMETER TRACE OF A SHADOW EDGE OF A RANGER 9 CRATER

From the above experiment, it can be seen that an MTF can be derived from a lunar photograph with reasonable precision. It can also be anticipated that it will be possible to detect operational degradations in cases where the degradation is the order of one to two times the size of the nominal resolution element.

4.2 Evaluation of System Performance Criteria for Nominal and Off-Nominal Conditions. - The effects of nominal and off-nominal conditions upon the system performance criteria are presented in this section. In particular, the variation of performance criteria discussed in Section 3.1 are examined as a function of phase angle, radiation exposure level and operational degradations (e.g., image motion, image vibration and defocus). It is shown that the values of σ_α and σ_ℓ (the error in measurement of slope and length) increase above their nominal values for off-nominal operating conditions. The data in this section were obtained using an IBM 7044 programmed with a solution of the equations described in Appendix E and simulating system response by employing analytically determined line spread functions. In addition to these results, image traces computed assuming a point scanning aperture, are given for various off-nominal conditions as illustrative examples of the degradation introduced into the image if such conditions should exist during a mission. In most cases the object chosen for the computation is a sloped surface 7 meters long inclined at 7 degrees to the horizontal.

Variation of the value of P_e , the error probability for the detection of cone targets, could not be analyzed in as great detail due to the lack of sufficient time.

4.2.1 Effect of Total Noise Power Upon Performance. - All three performance criteria, namely, σ_α, σ_ℓ and P_e , depend upon the noise power density. The first two criteria, as shown in Appendix E, are directly proportional to the square root of the effective white noise power density and hence to the total noise power. In the noise analysis

described in Appendix D, it was found* that the nominal total noise power in the reconstructed image expressed relative to the GRE input signal is about 43 800 (millivolts)^2. Converting this to density on the GRE film, by employing the linear relationship between input voltage and GRE film density, one finds that rms density difference is about $\sigma_D = 0.06$ which agrees quite well with that visible on the typical trace made on the GRE copy and shown in Figure 15. Table 1 shows the distribution of the nominal total noise power with respect to the various noise sources in the system. The largest contributor to the noise in the image is the SO-243 film grain.

Table 1 DISTRIBUTION OF THE NOMINAL TOTAL NOISE POWER (DENSITY OF 0.8 ON SO-243 FILM)

SOURCE	PERCENTAGE OF NOMINAL TOTAL NOISE POWER
SO-243 FILM GRAIN	69.3
DATA LINK	13.3
LST PHOSPHOR	5.3
KINE PHOSPHOR	5.2
5374 FILM GRAIN	3.9
PHOTOMULTIPLIER SHOT NOISE	3.0
VIDEO AMPLIFIER	NEGLIGIBLE

The total noise power in the image for off-nominal conditions may be computed by using the curves shown in Figure 22. These curves show the contribution of each noise source to the total noise power in the image. For convenience, the curve for the SO-243 film grain is plotted against

* The nominal values of the total noise power for each noise source assumed to be those given in Reference 7.

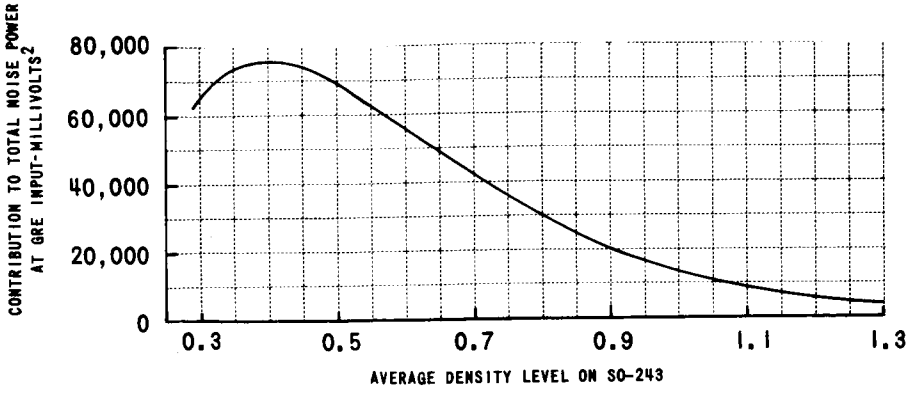

(a) SO-243 FILM GRAIN

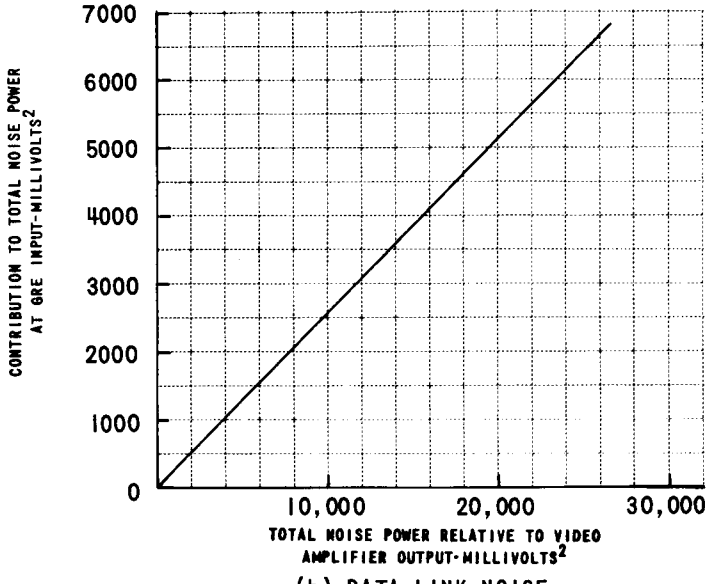

(b) DATA LINK NOISE

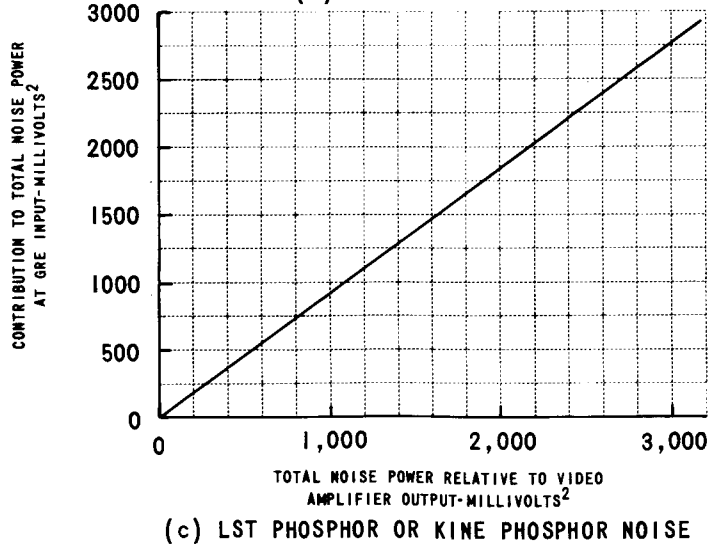

(c) LST PHOSPHOR OR KINE PHOSPHOR NOISE

Figure 22 CONTRIBUTION OF VARIOUS NOISE SOURCES TO THE TOTAL NOISE POWER IN THE GRE IMAGE (1 OF 2)

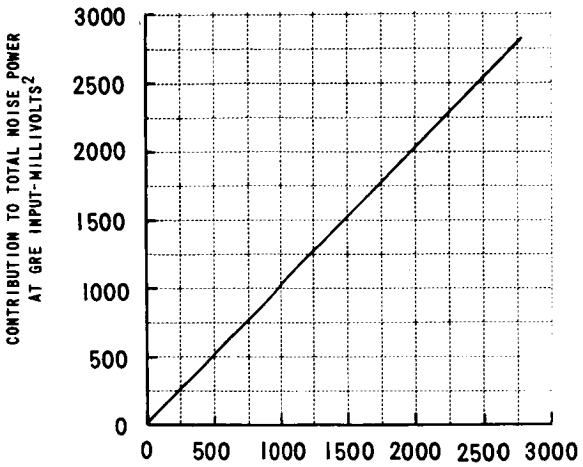

(d) 5374 FILM GRAIN

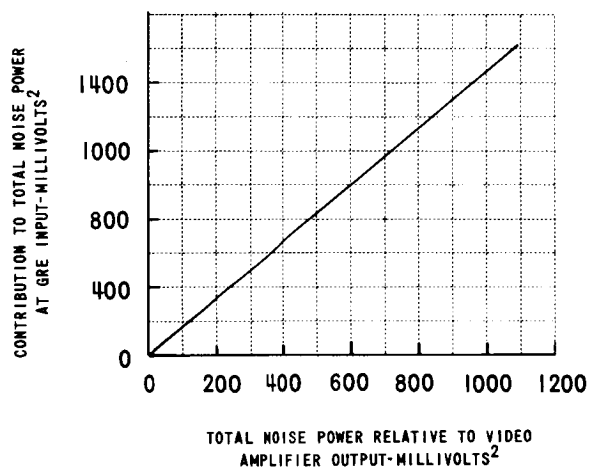

(e) PHOTOMULTIPLIER SHOT NOISE

Figure 22 CONTRIBUTION OF VARIOUS NOISE SOURCES TO THE TOTAL NOISE POWER IN THE GRE IMAGE (2 OF 2)

the average density level of image on the SO-243 film. To correct for off-nominal noise performance it is only necessary to compute a new noise power by adding the contributions from each noise source determined from the figure and adjust the values of σ_α and σ_ℓ by multiplying by the square root of the ratio of the new noise power to the nominal noise power.

4.2.2 Effect of Phase Angle and Radiation Exposure Upon Performance. - Several factors can alter the density recorded on the SO-243 film for the same topographic feature on the lunar surface. The effect upon σ_α and σ_ℓ of two such factors, the phase angle and radiation exposure are considered here. Figure 23 (a) shows the change in σ_α as the phase angle is increased. Two features are considered; both are slopes 7 meters long and inclined toward the sun at angles of 7 degrees and 11 degrees. Similarly, Figure 23 (b) shows the change in σ_ℓ with phase angle for two cases; ℓ = 7 meters and ℓ = 15 meters, both objects inclined at 7 degrees toward the sun. The values of σ_α and σ_ℓ shown were computed assuming a nominal system line spread for the 24" lens and using the nominal total noise power. In all cases, higher values of phase angle decrease the errors in measuring the parameters. It is interesting to note that although σ_α decreases with increasing phase angles as would be expected, the rate of change is smaller in the region above 70° than below.

There is a possibility that the film in the spacecraft will receive some radiation exposure before development. This exposure is added to the exposure due to the aerial images to determine the density on the developed SO-243 film. Figure 24 shows the variation of σ_α and σ_ℓ with the fog density (i.e., the density in an area of the format where the aerial exposure is zero). These values were computed for nominal total noise power of 17 200 square millivolts to account for the higher average density or lower total noise power of the SO-243 film. From the figure it can be seen that the errors increase rapidly with the level of radiation exposure. Once the fog density of the SO-243 film is above 0.8 the criteria indicates that the photographs contain very little topographic information.

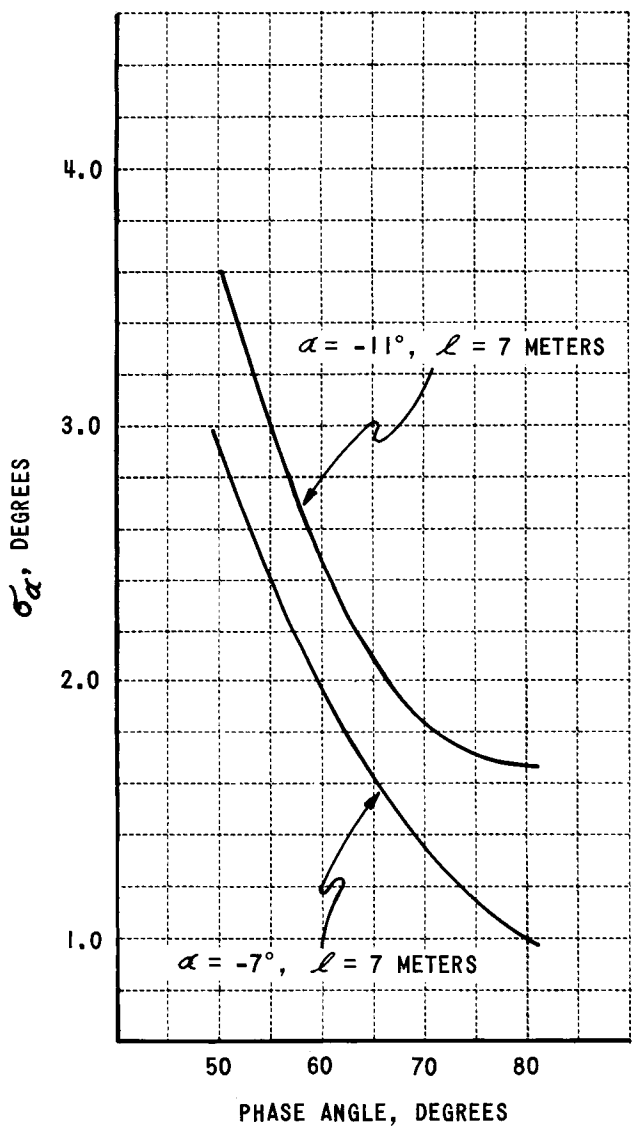

(a) VARIATION OF σ_α WITH PHASE ANGLE

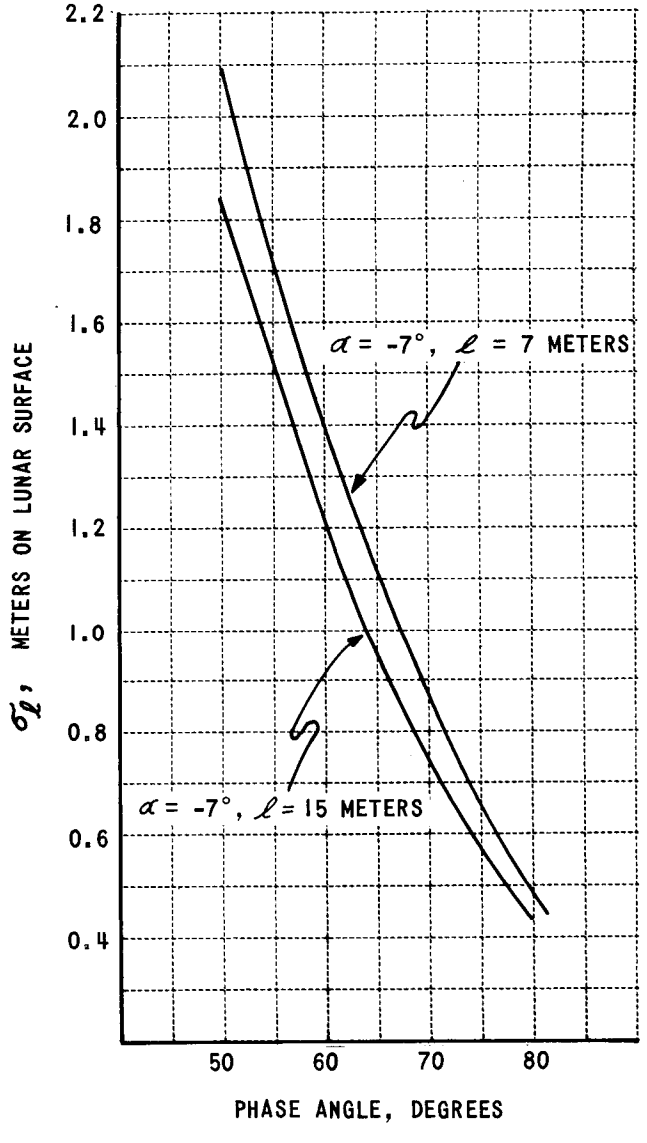

(b) VARIATION OF σ_ℓ WITH PHASE ANGLE

Figure 23 EFFECT OF PHASE ANGLE UPON σ_ℓ AND σ_α

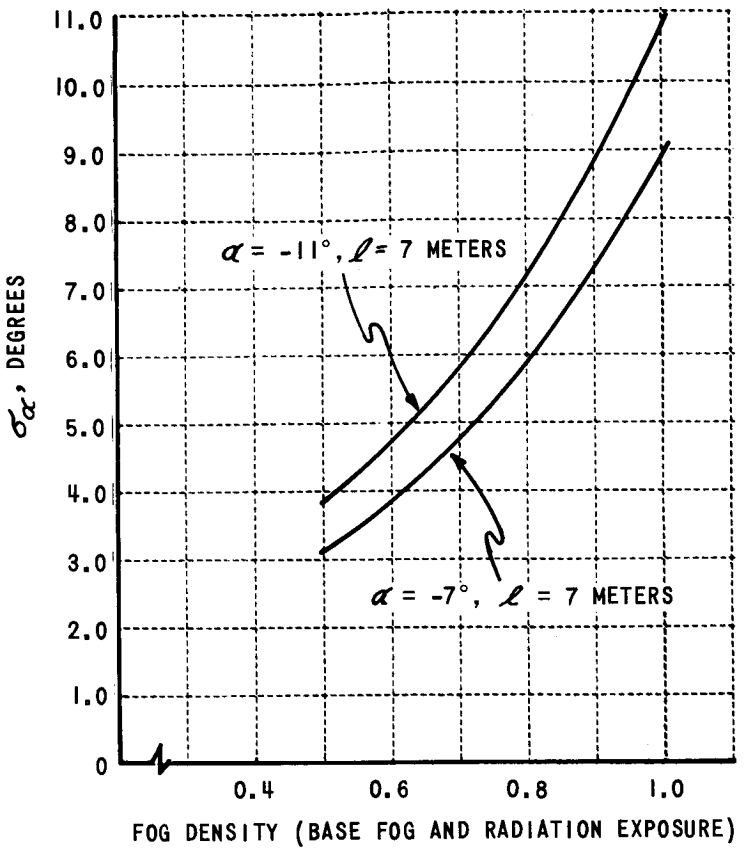

(a) VARIATION OF σ_α

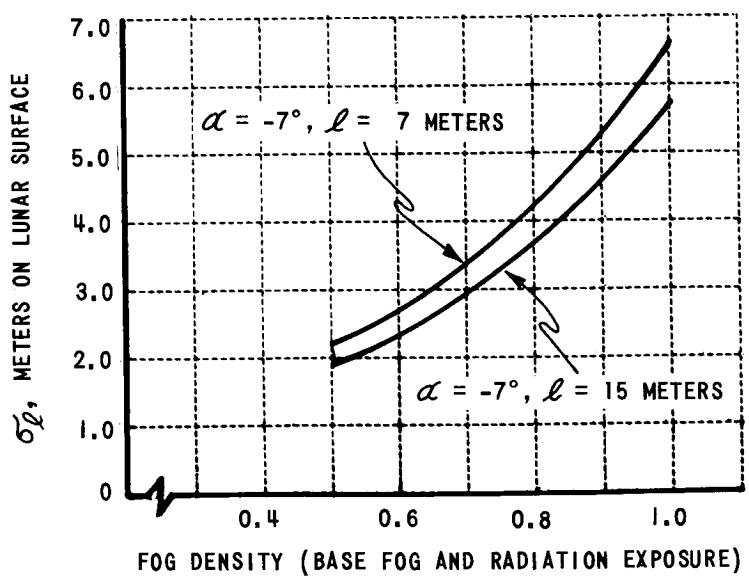

(b) VARIATION OF σ_ℓ

Figure 24 EFFECT OF RADIATION EXPOSURE

REFERENCE:

D2-100293-1
"PICTURE DATA STSTEMS ANALYSIS", P. 140
FIGURE 6.1-4

4.2.3 Effect of Operational Degradations. - Three types of operational degradations were investigated; image motion, image vibration, and defocus. The system line spread function for various magnitudes of these degradations is shown in Figure 25. These line spread functions were determined by using a computational program simulating system performance. The distances shown in Figure 25 are measured at the SO-243 film plane. At the nominal altitude of 46 km, 1 meter on the lunar surface is equivalent to 13.25 microns on the SO-243 film in the high resolution photographs. From the figure, it is seen that the degradations decrease the maximum of the line spread function (which is equivalent to the area under the modulation transfer function) below nominal, as would be expected. Note that the double spike characteristic of image vibration is visible in the two-meter degradation but not in the corresponding one-meter case. Figure 26 shows the change in σ_α for all three degradations for two cases; $\alpha = -7^\circ, \ell = 7$ meters, $\alpha = -11^\circ$, and $\ell = 7$ meters. In the computation, a phase angle of 70° was assumed. Similar changes of σ_ℓ for the cases of $\alpha = -7^\circ$, $\ell = 7$ meters and $\alpha = -7^\circ$, $\ell = 15$ meters are shown in Figure 27. In all cases, it is seen that the error measures increase monotonically with the magnitude of the degradation as would be expected from reasonable criteria. In order to illustrate the effect upon the image content of a test profile for these various degradations, the image synthesis techniques described in detail in Appendix G were employed. The parameters chosen for the test object are $\alpha = -7^\circ$ and $\ell = 7$ meters to correspond to the data previously presented. The traces shown in Figure 28 correspond to traces made across the image on the GRE original film using a point aperture. These traces are expressed in terms of GRE kinescope voltage which, for the nominal case, is linearly related to the GRE film density. The distances are measured in microns at the SO-243 film plane and a magnification of 7.2 must be included if it is desired to determine the corresponding distance on the GRE film. A phase angle of 70° and the nominal SO-243 bimat processing D log E curve were assumed. For the test profile chosen, that is, a slope inclined toward the sun between two flat surfaces, the perfect image would be an inverted rectangular pulse in GRE film density. This is shown in part

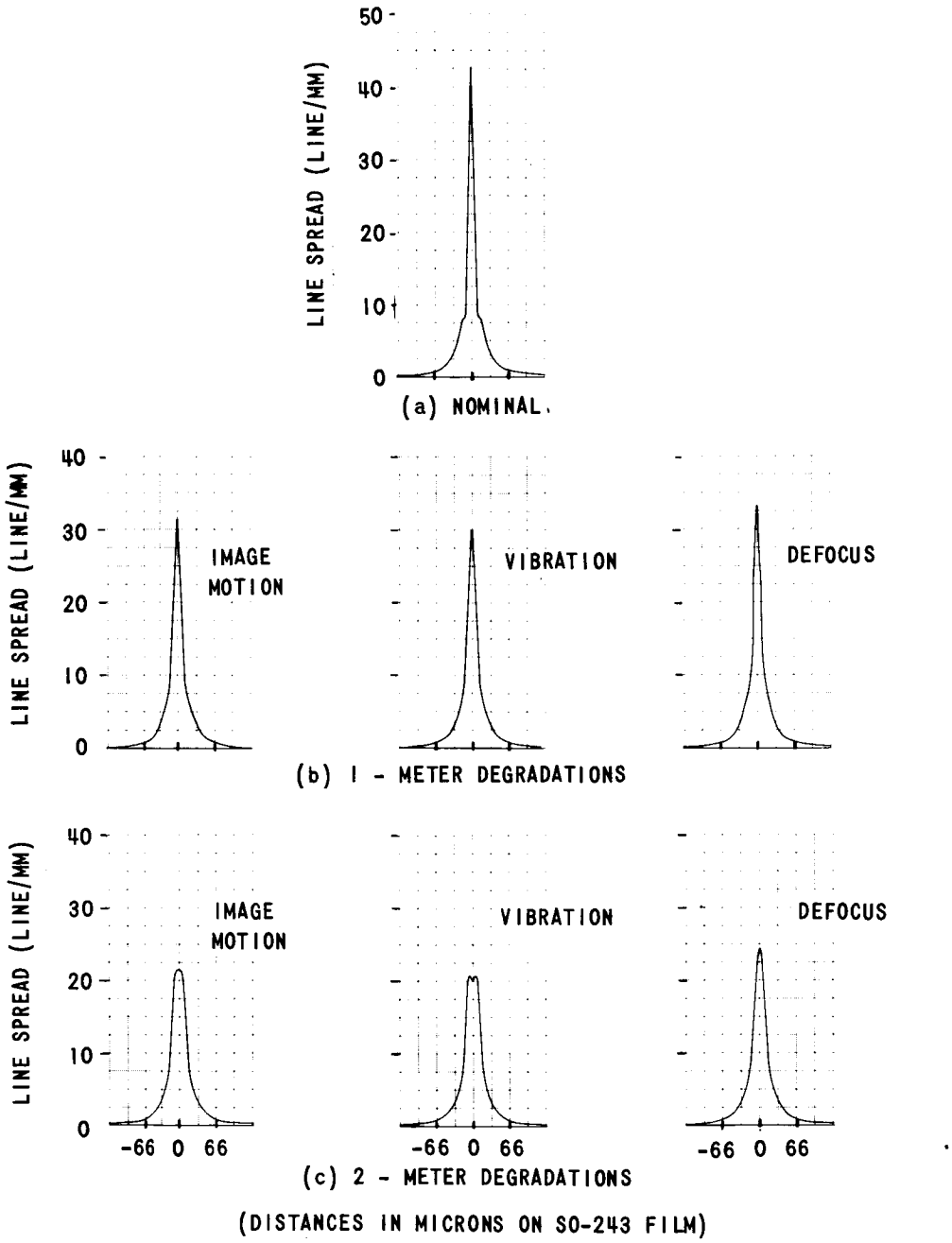

Figure 25 TYPICAL SYSTEM LINE SPREAD FUNCTIONS (LOW CONTRAST OBJECT APPROXIMATION)

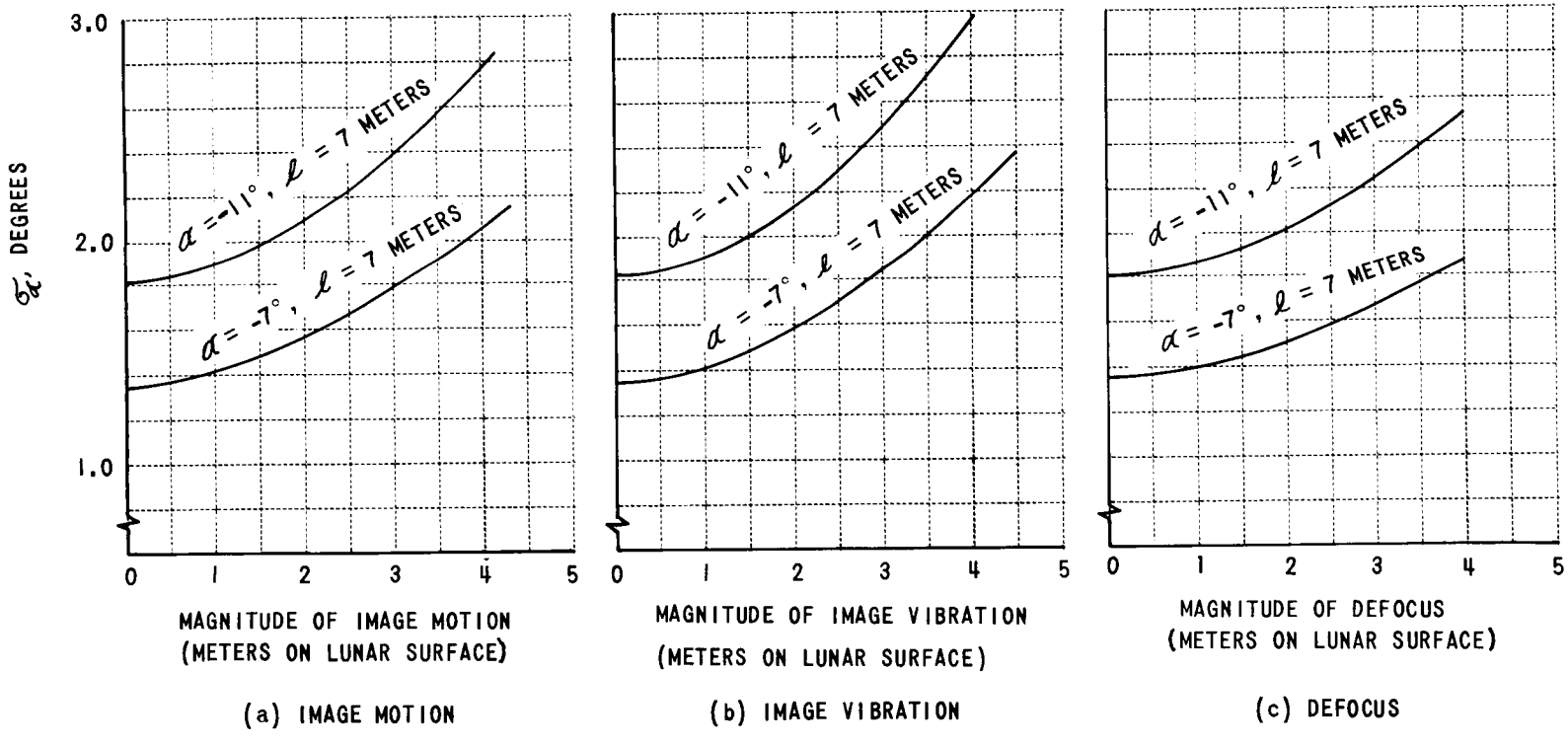

Figure 26 VARIATION OF σ_α WITH OPERATIONAL DEGRADATIONS

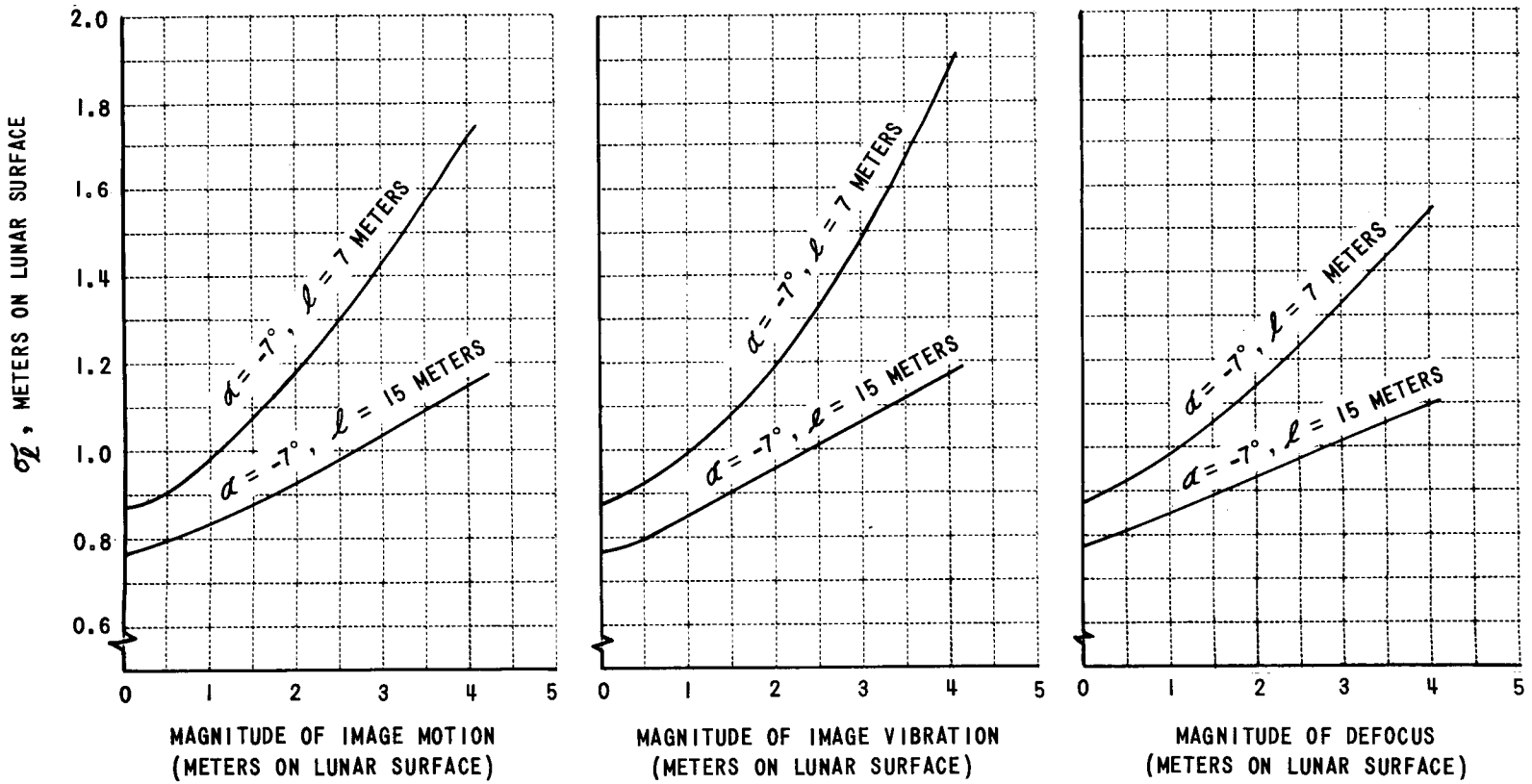

Figure 27 VARIATION OF σ_ℓ WITH OPERATIONAL DEGRADATIONS

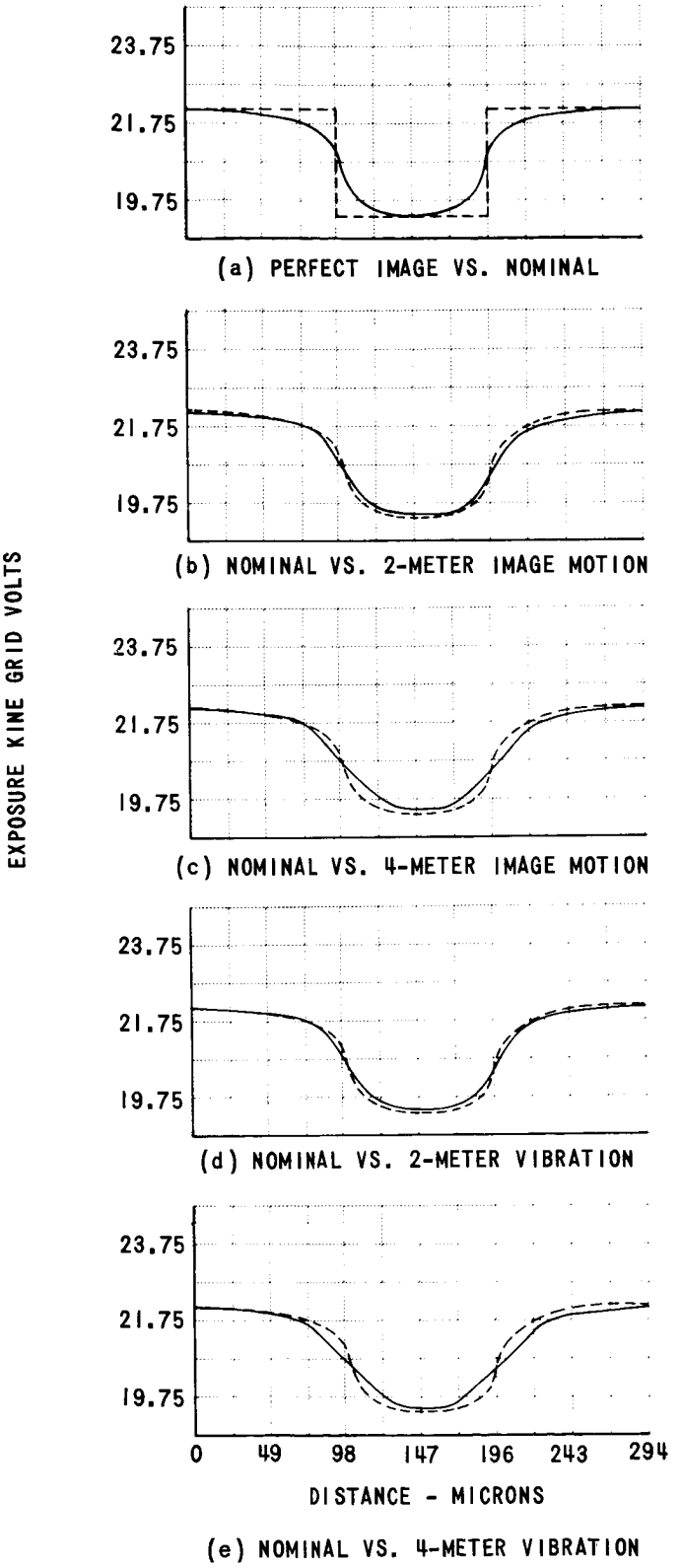

Figure 28 COMPARISON OF SLOPE IMAGES ON THE GRE FILM FOR SEVERAL DEGRADATIONS

(a) of Figure 28. In addition, the same object is shown employing the nominal line spread function. As expected, the suppression of high frequency information by the system causes a rounding of the rectangular pulse image. The remaining parts of the figure show the image when various operational degradations are present compared to the nominal image. In all cases, the degradations cause the sides of the image to become considerably less sharp and consequently decrease the ability to measure ℓ, the length of the slope, accurately in the presence of noise. This is reflected in the increase of the measure σ_ℓ with increasing degradation. In addition, the amplitude of the image is decreased slightly causing the estimate of the angle of the slope to be less than the actual value. It can be seen from these examples that σ_ℓ should change more rapidly with the magnitude of the degradation than σ_α. This fact is evident when one considers the ratio of off-nominal to nominal values for σ_α and for σ_ℓ as shown in Figure 29 for the case of image motion. The fractional change in σ_ℓ is greater for the same magnitude of degradation.

From these results it can be concluded that σ_α and σ_ℓ are reasonable measures of system performance and, in addition, have significance relative to the Lunar Orbiter mission.

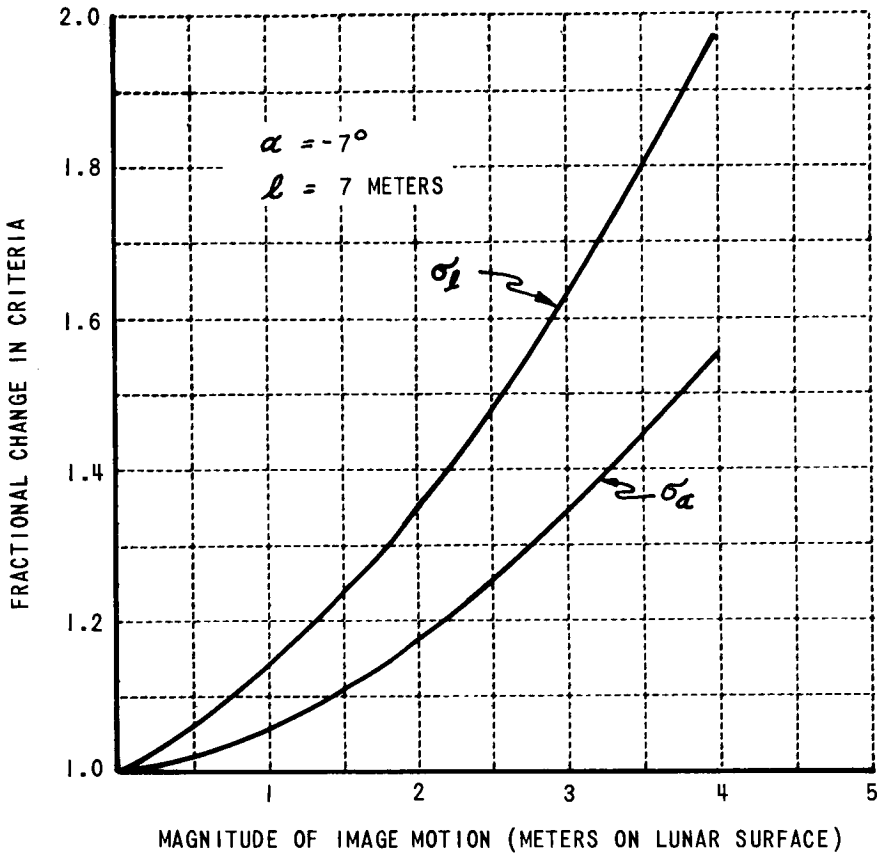

Figure 29 FRACTIONAL CHANGES IN CRITERIA

5. CONCLUSIONS

A method has been developed to make quantitative measurements of those factors which define the quality of monoscopic photographs to be received from the Lunar Orbiter spacecraft. These factors have been related to three system performance criteria which describe the ability of the system to detect and measure topographic features, obstacles and slopes. The variation of these criteria with off-nominal conditions of the Lunar Orbiter system has been demonstrated by the theoretical system analysis. In addition, the ability to detect reasonably small operational degradations from Lunar photographs by the suggested methods has been demonstrated experimentally by simulations using Ranger photographs.

Relative to the computation of a figure-of-merit, the following procedure was evolved:

(1) To evaluate detail rendition, a microdensitometer scan, using a narrow slit aperture, must be made over at least one crater shadow edge image and over an edge image in the pre-exposed data array, all on the GRE film. These scans, as shown in Figure 30, are used as inputs to a computer program which determines the end-to-end system line spread function. The end-to-end photographic system is non-linear due to the presence of the SO-243 film in the spacecraft and since the only available targets on the lunar surface are high contrast objects, namely, the shadow-to-sunlight edge in a crater, the analysis requires two scans. One scan (viz., crater shadow edge) includes the effect of the non-linear element. The second scan (viz., pre-exposed edge data) permits the removal of the effect of the non-linearity and two transfer functions, one for each linear segment, can be evaluated. These may be combined to determine the end-to-end system line spread function which represents the Lunar Orbiter photographic system when considering low contrast objects such as is done in establishing the system performance criteria.

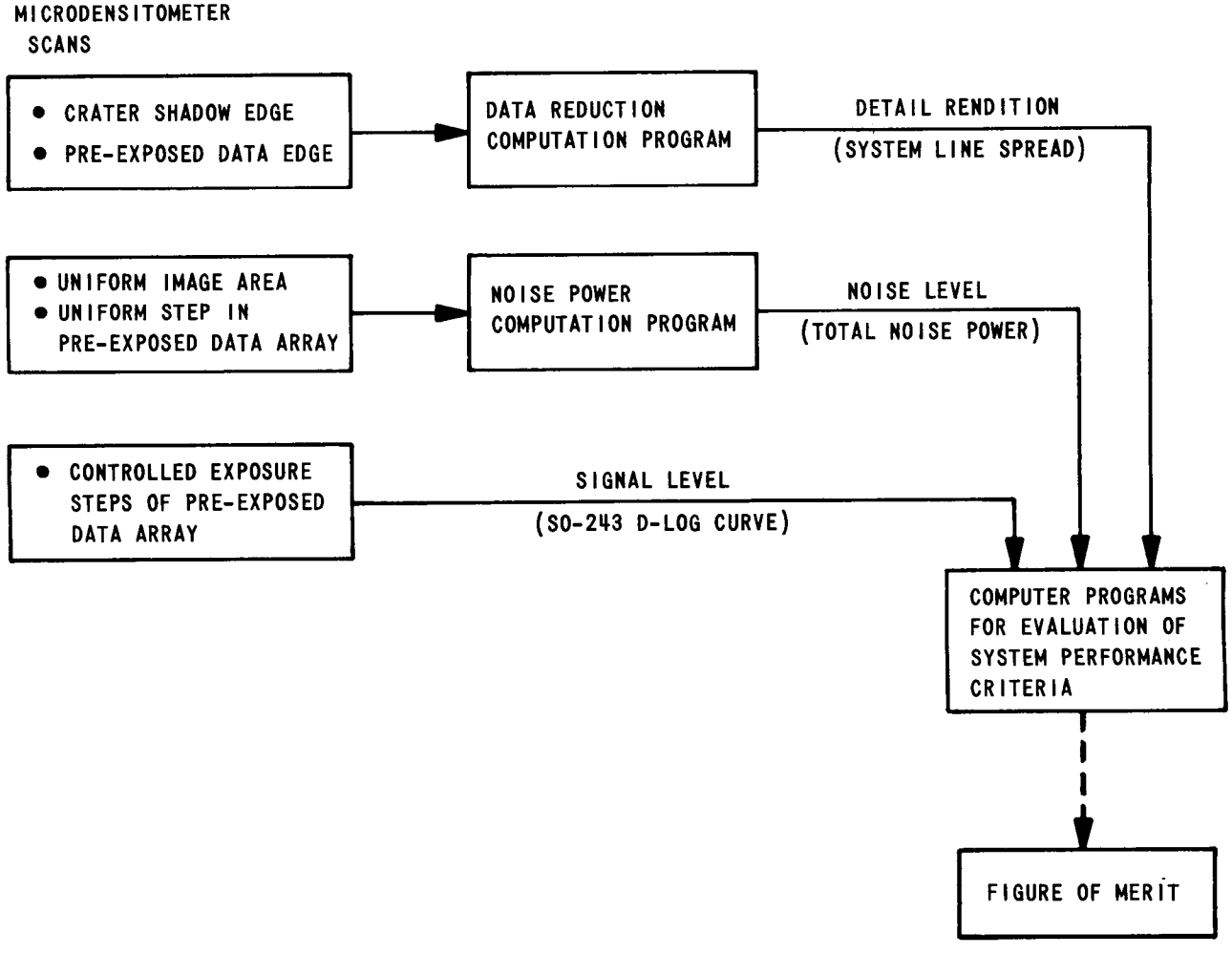

Figure 30 LUNAR ORBITER PHOTOGRAPHIC QUALITY EVALUATION FLOW DIAGRAM

(2) To measure the noise level, a microdensitometer scan, using a small aperture, must be made over a relatively uniform image area and over one step in the image of the pre-exposed data. These scans are used in the noise power calculation program.

(3) To measure signal level or gain factors, a microdensitometer scan must be made over the image of the series of controlled exposure steps in the pre-exposed data array. Additional information must be provided concerning the system gain (SO-243 film transmittance to GRE film density) used in transmitting the Lunar Orbiter photographs.

(4) From these data, the three system performance criteria, namely, the error in inclination angle measurement, length of slope measurement, and detection of conical obstacles can be determined using computer programs as shown in Figure 30.

(5) Finally, these performance criteria may be weighted based on the relative importance of the various tasks and combined to determine a figure of merit.

6. RECOMMENDATIONS

At the conclusion of this effort, a number of recommendations can be made with respect to the use of the results of the program. The recommendations are divided according to whether attention is desirable before, during, or after the first Lunar Orbiter mission. Before the first mission is launched, it is recommended that:

(1) A final selection of a single figure of merit should be made, including a decision as to the number of format positions and orientations used to evaluate the system performance criteria which will be combined into one figure of merit.

(2) As ground test results become available from the complete system tests, the sharpness of the test edges on the SO-243 film should be re-evaluated, preferably using a sample of SO-243 treated as similarly as possible to that loaded into the spacecraft.

(3) If nominal values of system performance are used as a reference in the figure of merit, the nominal performance values should be re-evaluated using the most recent data possible.

(4) If test films from the Lunar Orbiter system become available with simulated lunar objects present in the format, the complete MTF computer program and measurement techniques should be tested with these films.

(5) The noise measurement program should be used with test films to compare results with several different numerical filters, in order to select an improved filter to minimize errors in noise measurement.

(6) If the error probability of cone detection is a desired input to the figure of merit, the probability should be evaluated for various off-nominal conditions of operation, as was done for the errors in slope measurements.

During the Lunar Orbiter Missions, it is recommended that:

(7) The gain settings of the system, from the SO-243 transmittance to the GRE grid voltage, should be recorded for use in the quality evaluation program.

After the original Mission film is processed, it is recommended that:

(8) Adequate steps should be taken to assure that the relation between the density on the GRE original film and the density on the copy film used for evaluation is known. Several methods of control are suggested in the text.

In addition to the above, it is recommended that at some time before the analysis of the films is conducted:

(9) The extent to which various available image enhancement and image deblurring techniques might be applied to the Lunar Orbiter photographs should be investigated as well as the effect the enhancements would have on measurement accuracy. Such a program should examine physical limits on enhancement or deblurring and the extent to which these limits can be approached in practice by available techniques.

APPENDIX A

VALIDITY OF LINEAR ANALYSIS OF LUNAR ORBITER SYSTEM FROM SO-243 TRANSMITTANCE TO GRE FILM DENSITY

A pertinent question in any analysis of the Lunar Orbiter Photographic System is which elements may be considered as linear. The camera system, up to the SO-243 film is known to be linear in the intensity of light. The SO-243 film converts exposure, that is intensity times time, to film transmittance in a non-linear way, and cannot be considered linear except over very short intervals (i.e. low contrast objects). The film is then scanned, the time signal transmitted, and an image reconstructed on the ground. It is the purpose of this appendix to consider the operation of this latter portion of the system, and in particular, to prove that a linear analysis can be used and to specify the method for the linear analysis. Fortunately, the problems of the photographic system (PS) scanner and the Ground Reconstruction System (GRS) kinescope are similar to those encountered in television systems and hence have been the subject of early investigations[8]. The analysis presented in this appendix is based in large part upon the investigation by Mertz and Gray.

Notation

Before presenting the analysis, the notation and some of the mathematical relationships frequently employed in the analysis are defined in this section. The following symbols are employed:

u, v - the nominal velocity of the scanning spot of the PS scanner in the x and y directions respectively ($u \approx 2300$ mm/sec.),

ℓ_x, ℓ_y - the dimensions of the framelet* scanned in the vehicle (ℓ_x = 2.54 mm, ℓ_y = 57.6 mm),

N - the number of scan lines used in scanning a framelet ($\sim$17 000),

t_o - The time necessary to scan one framelet,

$T(x,y)$ - the transmittance of the image on the SO-243 film (including effect of base fog level),

$I_1(x,y)$ - the irradiance distribution of the scanning spot in the PS scanner,

$e_p(t)$ - the output of the photomultiplier (voltage),

$e_i(t)$ - the input to the GRS kinescope (voltage),

u', v' - the nominal velocity of the scanning spot of the GRS kinescope in the x', y' directions,

ℓ_x', ℓ_y' - the dimensions of the reconstructed framelet,

$I_2(x',y')$ - the output distribution of the kinescope spot,

$D(x',y')$ - the density on the GRS reconstruction film,

$\nu_x, \nu_y, \nu_x', \nu_y'$ - spatial frequencies, corresponding to x, y, x', y' directions,

f - temporary frequency,

$\tau_T(\nu_x, \nu_y)$ - spectrum (i.e., Fourier Transform) of $T(x,y)$

$\tau_D(\nu_x, \nu_y)$ - spectrum of the density of the GRS film,

$\tau_1(\nu_x, \nu_y)$ - frequency response of the GRS reconstruction spot (normalized Fourier Transform of $I_1(x,y)$),

$\tau_2(\nu_x', \nu_y')$ - frequency response of the PS scanning spot (normalized Fourier Transform of $I_2(x',y')$),

E_1 - the energy contained in the PS scanning spot, viz., $E_1 = \iint I_1(x,y)\,dx\,dy$ and,

D_2 - the maximum density of the GRS film, vis. $D_2 = \iint I_2(x',y')\,dx'dy'$

* It takes 120 framelets to scan out one frame consisting of a high resolution and low resolution photograph.

In addition the following expressions will be used for Fourier Transform pairs $f(x,y)$ and $\tau(\nu_x, \nu_y)$ in the space domain,

$$\tau(\nu_x, \nu_y) = \iint f(x,y)\, e^{-i2\pi(\nu_x x + \nu_y y)}\, dx\, dy$$

and

$$f(x,y) = \iint \tau(\nu_x, \nu_y)\, e^{i2\pi(\nu_x x + \nu_y y)}\, d\nu_x\, d\nu_y$$

with analogous definitions for the time domain. For these definitions the convolution integral becomes

$$\int f_1(x) f_2(x)\, e^{-i2\pi\nu_x x}\, dx = \int \tau_1(\nu_x - \sigma)\, \tau_2(\sigma)\, d\sigma$$

Analysis

P. S. Scanner. - The PS scanner is considered first, and the output time signal and its spectrum are derived. Following Reference 8, it is convenient for the purposes of analysis to construct a periodic array by repeating the image to be scanned, $T(x,y)$.* Let the transmittance of the array be given by $T'(x,y)$, which can be expressed, because of its periodicity, as a double Fourier series, viz.

$$T'(x,y) = \sum_{n=-\infty}^{\infty} \sum_{m=-\infty}^{\infty} D_{mn}\, e^{i2\pi\left[\frac{mx}{\ell_x} + \frac{ny}{\ell_y}\right]} \qquad \text{(A-1)}$$

---

* The base fog density of the SO-243 film D = 0.3 so, $T_{MAX} = 0.50$.

where

$$D_{mn} = \frac{1}{\ell_x \ell_y} \int_{-\ell_x/2}^{\ell_x/2} \int_{-\ell_y/2}^{\ell_y/2} T'(x,y) e^{-i2\pi\left[\frac{mx}{\ell_x} + \frac{ny}{\ell_y}\right]} dx\,dy.$$

If $\tau_T(\nu_x, \nu_y)$ represents the Fourier transform of the transmittance of the original photograph, D_{mn} can be written as $D_{mn} = \tau_T\left(\frac{m}{\ell_x}, \frac{n}{\ell_y}\right)\Big/\ell_x \ell_y$. Assume that the original photograph is scanned by a spot which has an irradiance distribution $I_1(x,y)$. The resulting energy, $\mathcal{E}(x,y)$, detected by the photomultiplier for any position x, y of the scan spot is given by

$$\mathcal{E}(x,y) = \int_{-\infty}^{\infty}\int I_1(\xi,\eta)\, T'(x+\xi, y+\eta)\, d\xi\, d\eta \qquad \text{(A-2)}$$

Substituting (A-1) into (A-2) yields

$$\mathcal{E}(x,y) = E_1 \sum_m \sum_n \frac{\tau_T\left(\frac{m}{\ell_x}, \frac{n}{\ell_y}\right)}{\ell_x \ell_y} \tau_1\left(\frac{m}{\ell_x}, \frac{n}{\ell_y}\right) e^{i2\pi\left[\frac{mx}{\ell_x} + \frac{ny}{\ell_y}\right]} \qquad \text{(A-3)}$$

where $\tau_1(\nu_x, \nu_y)$ is the normalized frequency response of the PS scanning spot. In other system analysis the PS scanning spot is assumed to have a gaussian irradiance distribution, viz.

$$I_1(x,y) = \frac{E_1}{2\pi\beta_1^2} e^{-(x^2+y^2)/2\beta_1^2} \qquad \text{(A-4)}$$

In this case, the normalized response function is given by

$$\tau_1(\nu_x, \nu_y) = e^{-2\pi^2\beta_1^2(\nu_x^2 + \nu_y^2)} \qquad \text{(A-5)}$$

To convert $\mathcal{E}(x,y)$ to a time signal representing the electrical output signal of the scanner, allow the array to be scanned by a point aperture as shown in Figure A-1 (b). This is equivalent to the actual scanning of the photograph shown in Figure A-1 (a). The x and y

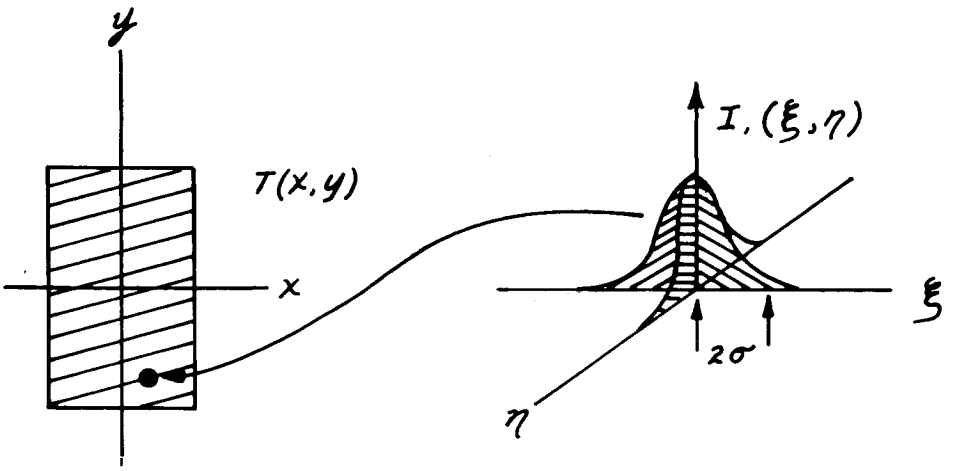

a) ACTUAL SCANNING PROCEDURE

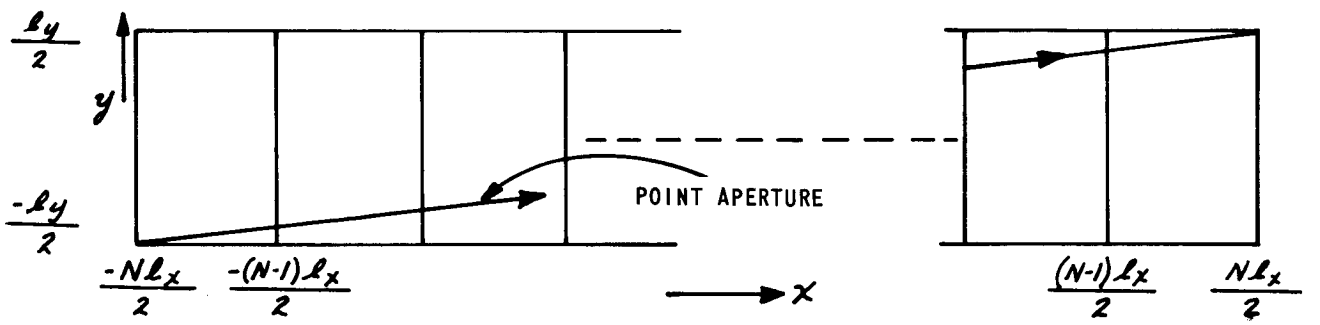

b) EFFECTIVE SCANNING PROCEDURE

Figure A-I SCANNING PROCEDURES

coordinates of the point aperture (equivalent to the center of the actual scanning aperture) are functions of time and are given by

$$x = ut \qquad and \qquad y = vt \tag{A-6}$$

Note that the parameter t has a range $-\infty < t < \infty$, or that negative values of time have meaning in this analysis, since they correspond to a point in the array. The actual, time limited, output signal of the photomultiplier, $s_p(t)$, is given by

$$s_p(t) = s'(t) \cdot s''(t) \tag{A-7}$$

where

$$s'(t) = \frac{K_p}{E_1} \mathcal{E}(ut, vt) = K_p \sum_m \sum_n \frac{\tau_T\left(\frac{m}{l_x}, \frac{n}{l_y}\right)}{l_x l_y} \tau_1\left(\frac{m}{l_x}, \frac{n}{l_y}\right) e^{i2\pi f_{mn} t} \tag{A-8}$$

$$f_{mn} = \frac{mu}{l_x} + \frac{nv}{l_y} \tag{A-9}$$

K_p is the output of the photomultiplier at 100% transmission ($K_p = 0.1$ volts)*, and $s''(t)$ is unity during the scan time, $-\frac{t_o}{2} \le t \le \frac{t_o}{2}$, and zero otherwise. If N scan lines are employed in scanning the photograph, the time for a complete scan of the photograph is

$$t_o = \frac{N l_x}{u} = \frac{l_y}{v} \tag{A-10}$$

If $v << u$, as is customary, then the velocity along a scan line is approximately u. This analysis, however, is not dependent upon the condition that $v << u$ except as it is required to eliminate the spectrum

* Figure 10, Reference 7. K_p will change depending upon the gain of the photomultiplier tube.

degradations discussed later. The output time signal of the photomultiplier (Equation A-7) becomes

$$s_p(t) = K_p \, \mathrm{rect}_t\left[-\frac{t_o}{2}, \frac{t_o}{2}\right] \cdot \sum_m \sum_n \frac{\tau_T\left(\frac{m}{\ell_x}, \frac{n}{\ell_y}\right)}{\ell_x \ell_y} \tau_1\left(\frac{m}{\ell_x}, \frac{n}{\ell_y}\right) e^{i2\pi f_{mn} t} \qquad \text{(A-11)}$$

where

$$\mathrm{rect}\, t\left[-\frac{t_o}{2}, \frac{t_o}{2}\right] = \begin{cases} 1 & -\frac{t_o}{2} \le t \le \frac{t_o}{2} \\ 0 & \text{otherwise.} \end{cases}$$

The spectrum or Fourier transform of $s_p(t)$ is given by the convolution of the Fourier transforms* of $s'(t)$ and $s''(t)$ or

$$S_p(f) = \int s_p(t) e^{-i2\pi f t} \, dt$$

$$= K_p t_o \left[\sum_m \sum_n \frac{\tau_T\left(\frac{m}{\ell_x}, \frac{n}{\ell_y}\right)}{\ell_x \ell_y} \tau_1\left(\frac{m}{\ell_x}, \frac{n}{\ell_y}\right) \delta(f_{mn} - f)\right] * \mathrm{sinc}(\pi f t_o) \qquad \text{(A-12)}$$

where δ represents the Dirac delta function and the asterisk is used to symbolize the convolution process. The first term of the convolution represents discrete spectral lines at frequencies $f = f_{mn}$ having amplitudes $\tau_T\left(\frac{m}{\ell_x}, \frac{n}{\ell_y}\right)\tau_1\left(\frac{m}{\ell_x}, \frac{n}{\ell_y}\right)\Big/\ell_x \ell_y$ and the second term represents a $\frac{\sin(\pi f t_o)}{\pi f t_o}$ function which broadens these discrete lines. The separation between the discrete spectral lines is given by

$$(\Delta f)_m = f_{m+1,n} - f_{mn} = \frac{u}{\ell_x} \qquad \text{or}$$

$$(\Delta f)_n = f_{m,n+1} - f_{mn} = \frac{v}{\ell_y} \qquad \text{(A-13)}$$

* Taken over the range $-\infty < t < \infty$

corresponding to unit changes in the index m and n, respectively. Since $v << u$, the change in frequency produced by increasing m by one is larger. The spectrum, therefore, consists of principal lines determined by setting $n = 0$ and allowing m to vary, and around the principal lines are the satellite lines arising from holding m fixed and changing n (see Figure A-2). Aside from the effect of the scanning aperture, $\tau_1\left(\frac{m}{\ell_x}, \frac{n}{\ell_y}\right)$, the amplitude of the principal lines arises from information contained in the x-direction and the amplitude of the satellite lines from information in the y-direction.

Expression (A-12) may be written directly as

$$S_p(f) = K_p t_o \sum_m \sum_n \frac{\tau_T\left(\frac{m}{\ell_x}, \frac{n}{\ell_y}\right) \tau_1\left(\frac{m}{\ell_x}, \frac{n}{\ell_y}\right)}{\ell_x \ell_y} \operatorname{sinc}\left[\pi (f - f_{mn}) t_o\right] \qquad \text{(A-14)}$$

since convolution with the delta function is simple. Consider a particular principal line (or value of m) and its associated satellite lines (various n values). The first zero of the sinc function occurs when $\Delta f = 1/t_o$ which is just the spacing between adjacent satellite lines. This condition fulfills the requirements of the Shannon sampling theorem[9] and, therefore, reproduces the original spectrum from the series of delta functions spaced at $1/t_o$.

The scanning, therefore, reproduces cross-sections of the spectrum of the transmittance of the scan-degraded photograph corresponding to $\nu_x = \frac{m}{\ell_x}$ at the temporal frequencies $f_m = \frac{mu}{\ell_x}$ and scaled by the velocity, v. Expression (A-14) may be rewritten as*

$$S_p(f) = K_p t_o \sum_{m=-\infty}^{\infty} \frac{\tau_T\left(\frac{m}{\ell_x}, \frac{f - \frac{mu}{\ell_x}}{v}\right) \tau_1\left(\frac{m}{\ell_x}, \frac{f - \frac{mu}{\ell_x}}{v}\right)}{\ell_x \ell_y} \qquad \text{(A-15)}$$

* The n subscript is eliminated since the spectrum $s(t)$ is "continuous" with respect to this subscript.

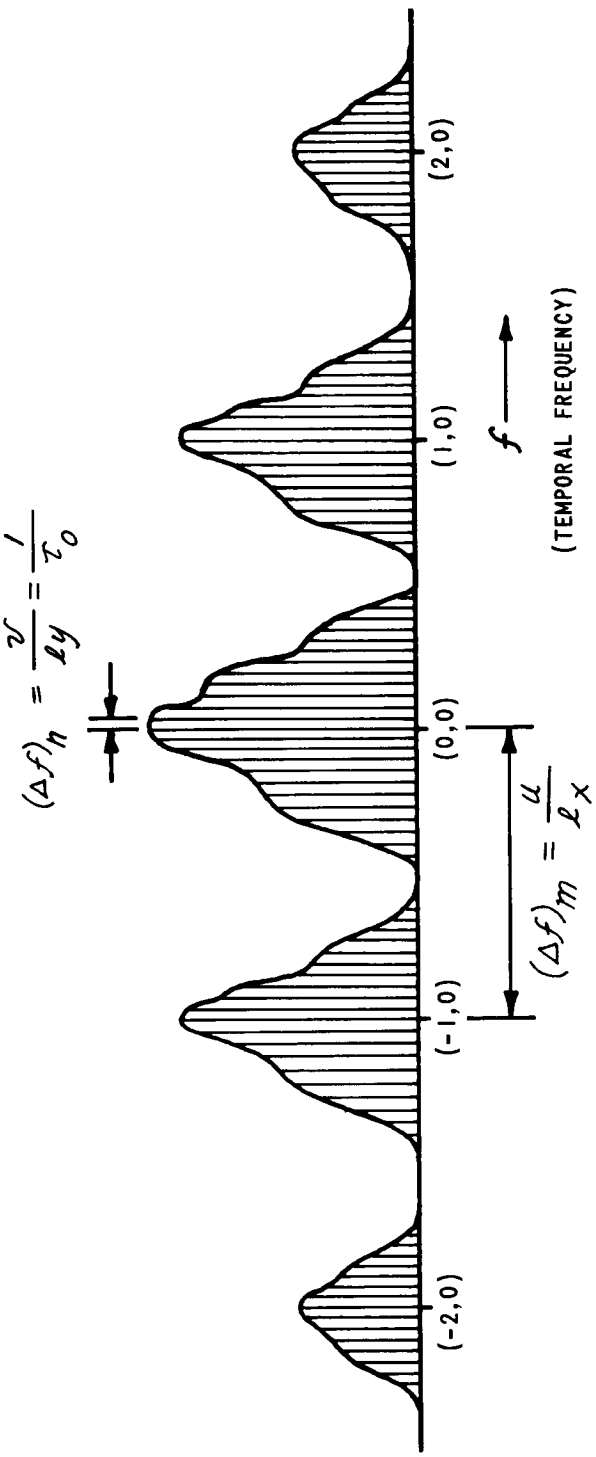

Figure A-2 SPECTRUM OF $\mathcal{A}'(t)$

The continuous reproduction of ν_y cross-sections of the spectrum is fortunate since the direction of the mechanical scan (y -direction) will contain most of the information of interest in the Lunar Orbiter photographs.

It is desirable to have $(\Delta f)_m = \frac{u}{\ell_x}$ large enough so that the adjacent ν_y cross-sections centered at $f_m = \frac{mu}{\ell_x}$ do not overlap (overlapping is sometimes referred to as a "confusion of the signal"). The width of these cross sections about f_m depends upon the information in the y -direction of the scan-degraded photograph which is limited by either the content of the original photograph (viz., lens-film frequency response) or the size of the scanning aperture. Assume that the scanning aperture is a gaussian spot and limits the maximum frequency content in the y -direction viz.

$$|\nu_y| < \frac{1}{\pi\sigma} \tag{A-16}$$

corresponding to 95.4% of the area under the response function (Equation A-5). In the case of the PS scanner $\frac{1}{\pi\sigma} \approx 196 \frac{lines}{mm}$ exceeding the expected content of the original photograph. Thus in the case of the Lunar Orbiter the condition necessary to separate the adjacent components depends upon the maximum frequency content in the photographs, viz.

$$\frac{u}{v} > 2\ell_x R_y \quad or \quad N > 2\ell_y R_y \tag{A-17}$$

where R_y is the "resolution limit" of the original photograph on the SO-243 film.

This condition states that sampling must be done at twice the rate of highest spatial frequency to be resolved, a well-known result of the sampling theorem. For the Lunar Orbiter system we assume typical values $N = 17{,}000$ and $\ell_y \approx 57.6$ mm and find that if $R_y < \sim 150$ lines/mm no confusion of the signal will be present.

Due to defocusing properties of the scanner, the width of the gaussian spot varies across the format. This effect is not explicitly included in the analysis, as the images of interest are anticipated to be small compared to the total format, and the spot size in the area of the image of interest would be used in the analysis

GRS Kinescope Reconstruction

To determine the exposure received on the reconstruction film, a process similar to that used above is employed. Let primes be used to represent the coordinates and parameters in the film plane. Assume that a point scanning aperture reproduces an image array being between $-\frac{\ell'_y}{2} \le y' \le \frac{\ell'_y}{2}$. This is essentially backtracking along the path used to generate the scan pattern. First, the single scan line is specified, in terms of normalized voltage, at a point x', y' in the array, by the line:

$$V(x',y') = \begin{cases} \dfrac{s_i\left(\frac{y'}{v'}\right)}{V_o} & \text{if } y' = \dfrac{v'}{u'}(x') \\ 0 & \text{elsewhere} \end{cases} \qquad \text{(A-18)}$$

where $s_i(t)$ is the input voltage to the kinescope and V_o is the maximum voltage the signal may have. This expression is next allowed to shift sideways by intervals of the image width, to fold the array back into one image area. The normalized voltage becomes:

$$V(x',y') = \begin{cases} \dfrac{s_i\left(\frac{y'}{v'}\right)}{V_o} & \text{if } y' = \dfrac{v'}{u'}(x' + q\,\ell'_x) \\ & q \text{ any integer} \\ 0 & \text{elsewhere} \end{cases} \qquad \text{(A-19a)}$$

$$= \sum_{q=-\infty}^{\infty} \frac{s_i\left(\frac{y'}{v'}\right)}{V_o \ell'_y}\, \delta\left(\frac{u'}{v'}\, y' - \ell'_x q - x'\right) \qquad \text{(A-19b)}$$

where the Dirac delta function has been used to represent the relationship between the x' and y' coordinates in the reconstruction.

This expression is equivalent to a voltage signal in the image plane along the scan lines and an absence of a signal between scan lines, but can extend over the whole array. To express the voltage of the single reconstructed image, we multiply expression (A-19b) by a unit rectangular function which is unity when $-\frac{\ell_{x'}}{2} \leq x' \leq \frac{\ell_{x'}}{2}$ and zero otherwise; that is

$$rect_{x'}\left[-\frac{\ell_{x'}}{2}, \frac{\ell_{x'}}{2}\right] = \begin{cases} 1 & |x'| \leq \frac{\ell_{x'}}{2} \\ 0 & otherwise \end{cases}$$

This yields, for the normalized voltage signal, $V_i(x', y')$, corresponding to the reconstructed image signal, the expression

$$V_i(x', y') = \frac{rect_{x'}\left[-\frac{\ell_{x'}}{2}, \frac{\ell_{x'}}{2}\right]}{V_o \ell_{y'}} \sum_{q=-\infty}^{\infty} s_i\left(\frac{y'}{v'}\right) \delta\left(\frac{u'}{v'}, y' - \ell_{x'} q - x'\right) \quad \text{(A-20)}$$

The effect of the scanning spot size must now be introduced in the array to spread the scan lines to finite width. However, the voltage is related in a non-linear manner to the exposure of the GRE film, which is, in turn non-linearly related to the GRE film density. Thus a truly linear, general analysis cannot extend beyond this point. The use of the analysis must be considered. First, in predicting system performance, low contrast targets are of most interest, and for this case the non-linearities can be considered linear over the narrow range. The GRE film density is linearly related to the transmitted voltage, and a linear analysis will yield correct results. The second use of the analysis is in system quality measurement, where high contrast targets are used. In this case, the analysis in the direction (essentially along the electrical scans) is correct only so long as the GRE scanning spot does not introduce large degradations. Since the nominal operation calls for the GRE scan spot response in the x - direction

to exceed 85% at the system resolution limit, only a small error will be made in assuming linearity. In the y direction, the convolution is strictly correct until the spot on one scan line overlaps the spot on the next line. The result at the positions of the scan lines remains strictly correct until energy from the spot on one line reaches the center of the next scan line. This latter condition is all that is necessary for the quality measurements, and is in general almost the case in system operation. Therefore, a linear analysis will be continued.

The effect of the finite size of the scanning spot is included by convolving $V_i(x', y')$ with the corresponding output, $I_2(x', y')$, of the scanning spot, viz.

$$D(x', y') = \int_{-\infty}^{\infty} I_2(\xi, \eta)\, V_i(\xi + x', \eta + y')\, d\xi\, d\eta \qquad \text{(A-21)}$$

The spectrum $\tau_0(\nu_x', \nu_y')$ corresponding to the density of the image is given by

$$\tau_0(\nu_x', \nu_y') = D_2\, \tau_2(\nu_x', \nu_y')\, \tau_{V_i}(\nu_x', \nu_y') \qquad \text{(A-22)}$$

where D_2 is the maximum density produced by the GRS spot at maximum brightness and τ_2 is the MTF of the scanning spot. To determine $\tau_{V_i}(\nu_x', \nu_y')$, we take the Fourier transform of expression (A-20) and employ the convolution theorem, viz.

$$\tau_{V_i}(\nu_x', \nu_y') = \iint V_i(x', y')\, e^{-i2\pi(\nu_x' x' + \nu_y' y')}\, dx'\, dy'$$

Employing the convolution theorem, we may write $\tau_{V_i}(\nu_x', \nu_y')$ as the convolution of the Fourier transforms of $V(x', y')$, i.e., $\tau_V(\nu_x', \nu_y')$ and the Fourier transform of $\text{rect}_{x'}\left[-\frac{l_x'}{2}, \frac{l_y'}{2}\right]$ viz.

$$\tau_{V_i}(\nu_x', \nu_y') = \ell_x' \, \tau_V(\nu_x', \nu_y') * \delta(\nu_y') \, \mathrm{sinc}(\pi \nu_x \ell_x') \qquad \text{(A-23)}$$

Now, using (A-19b) and integrating over x to eliminate the delta function, yields:

$$\tau_V(\nu_x', \nu_y') = \frac{v'}{V_0 \ell_y'} \left[\sum_{q=-\infty}^{\infty} e^{i2\pi q \nu_x' \ell_x'} \int s_i(t) e^{-i2\pi(u'\nu_x' + v'\nu_y')t} \, dt \right]. \qquad \text{(A-24)}$$

Using a result for the Fourier transform of a periodic generalized function[10], viz. $\sum_{q=-\infty}^{\infty} e^{i2\pi q \nu_x' \ell_x'} = \frac{1}{\ell_x'} \sum_{k=-\infty}^{\infty} \delta\left(\nu_x' - \frac{k}{\ell_x'}\right)$, we may write

$$\tau_V(\nu_x', \nu_y') = \frac{v'}{V_0 \ell_y' \ell_x'} \sum_{k=-\infty}^{\infty} \delta\left(\nu_x' - \frac{k}{\ell_x'}\right) S_i(u'\nu_x' + v'\nu_y') \qquad \text{(A-25)}$$

In order to determine the temporal frequency spectrum of the input voltage signal, i.e., $S_i(f)$ we employ the expression

$$s_c(t) = K s_p(t) \qquad \text{(A-26)}$$

to relate the output signal of the photomultiplier to the communications system voltage signal $s_c(t)$. The spectrum of the input signal $S_i(f)$ is related to the spectrum of $s_c(t)$ by

$$S_i(f') = \tau_c(f') \, S_c(f') = K \tau_c(f') S_p(f') \qquad \text{(A-27)}$$

---

[3] See M. Lighthill, "Fourier Analysis and Generalized Functions," (Cambridge University Press, London) Section 5.4, 1958.

where $\tau_c(f)$ is the normalized frequency response of the communications system. We may now combine (A-15), (A-25) and (A-27) to determine $\tau_V(\nu_x', \nu_y')$, viz.

$$\tau_V(\nu_x', \nu_y') = \frac{K_p K}{V_0 \ell_x'} \sum_{k=-\infty}^{\infty} \delta\left(\nu_x' - \frac{k}{\ell_x'}\right) \tau_c(f') \sum_{m=-\infty}^{\infty} \frac{\tau_T\left(\frac{m}{\ell_x}, \frac{f' - \frac{mu}{\ell_x}}{v}\right) \tau_1\left(\frac{m}{\ell_x}, \frac{f' - \frac{mu}{\ell_x}}{v}\right)}{\ell_x \ell_y} \qquad \text{(A-28)}$$

where $f' = u'\nu_x' + v'\nu_y'$

It is interesting to note that when there is no-confusion-of-the-signal (the requirement expressed by Equation (A-17) is fulfilled) that only one value of m in the summation contributes at a particular value of f' so that

$$\tau_V(\nu_x', \nu_y') = \frac{K_p K}{V_0 \ell_x'} \sum_{k=-\infty}^{\infty} \delta\left(\nu_x' - \frac{k}{\ell_x'}\right) \tau_c(f') \frac{\tau_T\left(\frac{m'}{\ell_x}, \frac{f' - \frac{m'u}{\ell_x}}{v}\right) \tau_1\left(\frac{m'}{\ell_x}, \frac{f' - \frac{m'u}{\ell_x}}{v}\right)}{\ell_x \ell_y} \qquad \text{(A-29)}$$

where m' is chosen so that

$$\left| m' - \frac{f'\ell_x}{u} \right| < \frac{1}{2} \qquad \text{(A-30)}$$

Due to the presence of the Dirac delta function if $\tau_V(\nu_x', \nu_y') \neq 0$ we must have $\nu_x' = \frac{k}{\ell_x'}$ and therefore,

$$\frac{f'\ell_x}{u} = k + \frac{\ell_x}{u} v'\nu_y'$$

Equation (A-30) becomes

$$\left| m' - k - \frac{\ell_x}{u} v'\nu_y' \right| < \frac{1}{2} \qquad \text{(A-31)}$$

It is convenient to substitute an integer, $p(\nu_y')$ for $m' - k$, where p is therefore dependent on the ν_y' value selected. This substitution makes no difference inside the summation over k , because $g(x)\delta(x) = g(0)\delta(x)$

is a property of the delta function. Equation (A-29) under these conditions becomes

$$\tau_V(\nu_x', \nu_y') = \frac{K_p K}{V_0 \ell_x'} \sum_{k=-\infty}^{\infty} \delta\left(\nu_x' - \frac{k}{\ell_x'}\right) \tau_c(f') \frac{\tau_T\left(\frac{k+p(\nu_y')}{\ell_x}, g(\nu_y')\right)}{\ell_x \ell_y} \tau_1\left(\frac{k+p(\nu_y')}{\ell_x}, g(\nu_y')\right) \qquad \text{(A-32)}$$

where

$$g(\nu_y') = \frac{\nu' \nu_y' - \frac{p(\nu_y')}{\ell_x}}{\nu}$$

Recalling expressions (A-22) and (A-23):

$$\tau_D(\nu_x', \nu_y') = D_2 \ell_x' \tau_2(\nu_x', \nu_y') \cdot \left[\tau_V(\nu_x', \nu_y') * \delta(\nu_y') \operatorname{sinc}(\pi \nu_x' \ell_x')\right] \qquad \text{(A-33)}$$

the convolution may now be considered and τ_D evaluated. The convolution is:

$$\tau_V(\nu_x', \nu_y') * \delta(\nu_y') \operatorname{sinc}(\pi \nu_x' \ell_x') = \int_{-\infty}^{\infty}\int \tau_V(\zeta, \eta) \delta(\eta - \nu_y') \operatorname{sinc}(\pi[\zeta - \nu_x'] \ell_x') \, \delta\zeta \, \delta\eta \qquad \text{(A-34)}$$

the $\delta(\eta - \nu_y')$ sorts out values of η where $\eta = \nu_y'$, and the $\delta\left(\zeta - \frac{k}{\ell_x'}\right)$ from τ_V (see Equation A-32) sets $\zeta = \frac{k}{\ell_x'}$. Therefore τ_D becomes:

$$\tau_D(\nu_x', \nu_y') = \left(\frac{D_2 K_p K}{V_0 \ell_x \ell_y}\right) \tau_2(\nu_x', \nu_y') \left[\sum_{k=-\infty}^{\infty} \tau_c(f_k') \tau_T\left(\frac{K+p(\nu_y')}{\ell_x}, g(\nu_y')\right) \tau_1\left(\frac{K+p(\nu_y')}{\ell_x}, g(\nu_y')\right) \cdot \operatorname{sinc}(\pi K - \pi \nu_x' \ell_x')\right] \qquad \text{(A-35)}$$

where $g(\nu_y')$ was defined above, and $f_K' = \frac{u' k}{\ell_x'} + \nu' \nu_y'$

Now, if there is no distortion, but only a magnification between the SO-243 image and the reconstructed image, then $\frac{u}{\ell_x} = \frac{u'}{\ell_x'}$. Note that the sinc function is centered at $\nu_x' = \frac{k}{\ell_x'}$ and its first zeros are located at $\nu_x' = (K \pm 1)/\ell_x'$. Now τ_c is sampled at intervals of exactly $1/\ell_x'$ for constant ν_y', and τ_T and τ_1 which are evaluated in

SO-243 spatial frequency space are sampled at intervals of $1/\ell_x$, corresponding to intervals of $1/\ell_x'$ in GRE spatial frequencies. Thus, the summation over k is again interpretable in terms of the Sampling theorem, and the summation can be accomplished by simply replacing k by $\nu_x' \ell_x'$. τ_D becomes:

$$\tau_D(\nu_x', \nu_y') = \frac{D_2 K_p K}{V_0 \ell_x \ell_y} \tau_2(\nu_x', \nu_y') \tau_c(\nu_x' u' + \nu_y' v') \tau_T\left(\frac{\nu_x' \ell_x' + p}{\ell_x}, \frac{\nu_y' v'}{v} - \frac{up}{v\ell_x}\right) \times \tau_1\left(\frac{\nu_x' \ell_x' + p}{\ell_x}, \frac{\nu_y' v'}{u} - \frac{up}{v\ell_x}\right) \quad \text{(A-36)}$$

where it is recalled that (Equation A-31): $\left| p - \frac{\ell_x v' \nu_y'}{u} \right| < \frac{1}{2}$

For convenience, all measurements will hereafter be referred to SO-243 film space, to eliminate magnification factors in (A-36). τ_D becomes:

$$\tau_D(\nu_x, \nu_y) = K_1 \tau_2(\nu_x, \nu_y) \tau_c(u\nu_x + v\nu_y) \tau_T\left(\nu_x + \frac{p}{\ell_x}, \nu_y - \frac{Np}{\ell_y}\right) \tau_1\left(\nu_x + \frac{p}{\ell_x}, \nu_y - \frac{Np}{\ell_y}\right) \quad \text{(A-37)}$$

where $K_1 = \frac{D_2 K_p K}{V_0 \ell_x \ell_y}$ and $\left| p - \frac{\ell_y \nu_y}{N} \right| < \frac{1}{2}$. Examining the restriction on p, it is not difficult to see that each value of p corresponds to allowing a different range for ν_y, and moreover, that each allowed range does not overlap the range allowed by any other value of p. Thus, only $p = 0$ yields any contribution for frequencies (ν_y) in the range $|\nu_y| < \frac{N}{2\ell_y}$ or $|\nu_y| < R_y$. For this region, the image spectrum can be written:

$$\tau_D(\nu_x, \nu_y) = K_1 \tau_2(\nu_x, \nu_y) \tau_c(u\nu_x + v\nu_y) \tau_1(\nu_x, \nu_y) \tau_T(\nu_x, \nu_y) \quad \text{(A-38)}$$

Expressions similar to (A-38) can be written for each value of p.

Figure A-3 shows a summary of the spectral relations involved in the scanner systems. The spectrum of the SO-243 image is sliced as shown in (a) at intervals $\frac{1}{\ell_x}$ in ν_x , each slice is scaled by v and centered at u/ℓ_x in temporal frequency as shown in (b). The communications system response is entered by multiplication by $\tau_c(f)$ yielding the spectrum shown in (c). The slicing process is reversed, and the Sampling theorem is used to fill in the spectral values between the slices, yielding a continuous two-dimensional spectrum. This spectrum has the same range as that of the SO-243 image, and is now mapped for different p values as shown in (d). Finally, the mapped resultant spectrum is multiplied by the response of the reconstruction scanner (τ_2) .

If the display spot is dithered so as to remove the scan line pattern, this corresponds to τ_2 removing all spectra with $p \neq 0$. In this case, Equation (A-38) gives the relation between the SO-243 image and the display, and it is shown that a linear analysis of two-dimensional spectra can be applied to the system for these elements. Even if scan lines are present in the image, data taken to measure image quality can be numerically filtered to remove all but the $p = 0$ spectrum, and the data can be used in a linear analysis.

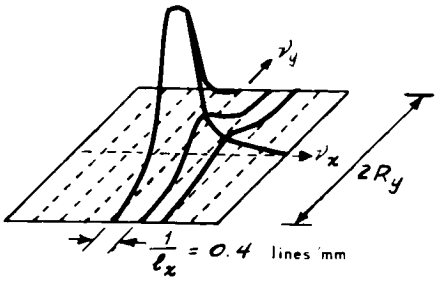

a) SPECTRUM OF TRANSMITTANCE OF SO-243 FILM CONVOLVED WITH SCANNING SPOT

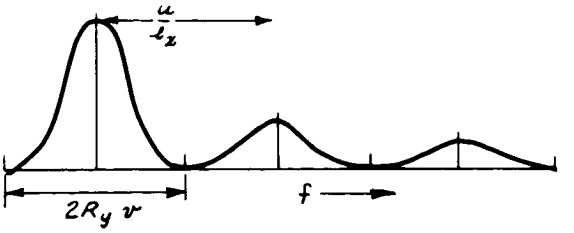

b) SPECTRUM OF TIME SIGNAL OUTPUT OF PHOTOMULTIPLIER, $S_p(f)$

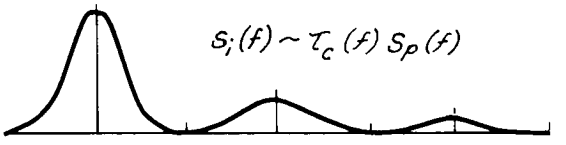

c) SPECTRUM OF INPUT SIGNAL OF GRE, $S_i(f)$

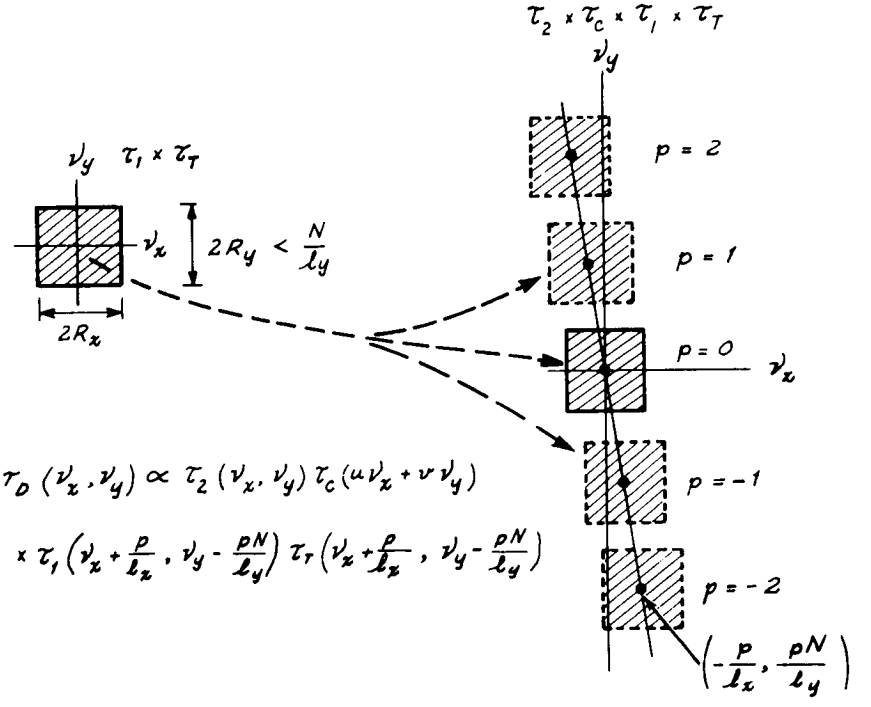

d) MAPPING OF THE SO-243 SPECTRUM RANGE BY SCANNING-COMMUNICATION SYSTEM

Figure A-3 TRANSFER FUNCTION ANALYSIS FOR SCANNER-COMMUNICATION-RECONSTRUCTION SYSTEM

APPENDIX B

MATHEMATICAL MODEL OF THE EXPECTED INTENSITY FUNCTION INSIDE A CRATER

By M. J. Mazurowski

It is shown in Section 2.1.1 that the only reasonable targets for evaluating details of the lunar photographs are shadow edges inside craters. Thus, it is desirable to know the intensity function inside the crater. This appendix develops mathematical formulas to evaluate the intensity distribution inside a spherical crater.

The selected model of the crater is a sphere of radius, a , in which the level surrounds are considered a plane. The plane of the surroundings cuts out a sector of the sphere which has a diameter, D, and a depth, d, (See Figure 4). The sun is assumed to be along the $+x$ axis and the camera along the $+z$ axis. The xz plane is the phase plane. The vertical view of the crater is that of a circle of radius $\frac{D}{2}$ which can be divided into three regions of differing intensity distributions; the shadow, the penumbra, and the sunlit part of the crater. The intensity in the shadow area of the crater is essentially zero (i.e., it is approximately 10^{-7} of the maximum intensity of the lunar surface). To determine the intensities in the penumbra and the sunlit part of the crater, a knowledge of the nature of the shadow is required. This is considered next.

Points in the crater lie on the surface of a sphere given by

$$x^2 + y^2 + (z - (a-d)^2) = a^2 \qquad \text{(B-1)}$$

The flat ground outside the crater is taken as the xy plane. It follows immediately from Equation B-1 and the fact that the crater has a radius of $\frac{D}{2}$ that

$$a^2 = (a-d)^2 + \left(\frac{D}{2}\right)^2$$

$$\frac{a}{d} = \frac{1}{8}\left[4 + \left(\frac{D}{d}\right)^2\right] \qquad \text{(B-2)}$$

The rays of the sun which make an angle θ with the XY plane (i.e., $\theta = \frac{\pi}{2} - g$, where g is the phase angle) and pass through the points y_c on the crater's rim are a family of lines given by

$$z = \tan\theta\left(x - \sqrt{\left(\frac{D}{2}\right)^2 - y_c^2}\right), \qquad |y_c| \le \frac{D}{2} \qquad \text{(B-3)}$$

Because values of y_c are on the spherical surface (see Equation B-1), the elimination of z from Equation B-3 and B-1 with $y_c = y$ gives the locus of points common to both the sphere and the family of lines and thus is the projection of the shadow onto the XY plane. Squaring the z part of Equation B-1, and inserting Equation B-2 and B-3 gives

$$x^2 + y^2 + \tan^2\theta\left(x - \sqrt{\left(\frac{D}{2}\right)^2 - y^2}\right)^2 - 2(a-d)\tan\theta\left(x - \sqrt{\left(\frac{D}{2}\right)^2 - y^2}\right) = \frac{D^2}{4} \qquad \text{(B-4)}$$

Subtracting $\left(\frac{D}{2}\right)^2$ from both sides of Equation B-4 and factoring gives

$$\left(x - \sqrt{\left(\frac{D}{2}\right)^2 - y^2}\right)\left[x + \sqrt{\left(\frac{D}{2}\right)^2 - y^2} + \tan^2\theta\left(x - \sqrt{\left(\frac{D}{2}\right)^2 - y^2}\right) - 2(a-d)\tan\theta\right] = 0 \qquad \text{(B-5)}$$

Multiplying Equation B-5 by $\cos^2\theta$ and collecting terms in the second bracket yields

$$\left(x - \sqrt{\left(\frac{D}{2}\right)^2 - y^2}\right)\left[x + \cos 2\theta\sqrt{\left(\frac{D}{2}\right)^2 - y^2} - (a-d)\sin 2\theta\right] = 0 \qquad \text{(B-6)}$$

The solution $x = \sqrt{\left(\frac{D}{2}\right)^2 - y^2}$ represent the unimportant locus of points on the rim of the crater. Thus, the shadow inside the crater is given by

$$x(y,\theta) = (a-d)\sin 2\theta - \frac{D}{2}\cos 2\theta \sqrt{1-\left(\frac{2y}{D}\right)^2},\ x^2+y^2 \le \left(\frac{D}{2}\right)^2 \qquad \text{(B-7)}$$

Equation B-7 shows that the shadow is an ellipse whose origin is located at $(a-d)\sin 2\theta$ and whose major axis along the y axis is equal to $\frac{D}{2}$. The minor axis of the ellipse in the X direction is $\frac{D}{2}\cos 2\theta$.

To make use of Equation B-7, equations relating a and d to the measurable quantities, θ and D, are required. Inserting $z = d$, and letting $y = 0$ in Equation B-3 gives

$$d = \left[\frac{D}{2} - x(0,\theta)\right]\tan\theta \qquad \text{(B-8)}$$

The distance $\left[\frac{D}{2} - x(0,\theta)\right]$ is the length of the shadow in the phase plane. Therefore, measuring the shadow length and the crater's diameter, D, and knowing the angle θ, d, and $\frac{D}{d}$ can be calculated from Equation B-8 which in turn yields the value a from Equation B-2. For the given crater dimensions and phase angle, the curve of the shadow can be obtained using Equation B-7.

The shadow's intersection with the phase plane is determined from $y = 0$ in Equation B-7, thus

$$x(0,\theta) = (a-d)\sin 2\theta - \frac{D}{2}\cos 2\theta \qquad \text{(B-9)}$$

Equation B-9 can be used to find the length of the penumbra, $\ell(\theta)$, in the phase plane. If it is assumed that θ is the elevation to the bottom edge of the sun and $\theta + \delta$ is the elevation to the top edge of the sun, then the length of the penumbra is the phase plane is given by

$$\ell(0,\theta) = x(0,\theta+\delta) - x(0,\theta) \qquad \text{(B-10)}$$

where $x(0,\theta)$ is given by Equation B-9. This could be generalized to obtain the length of the penumbra for any y and θ as

$$\ell(y,\theta) = \frac{\left[x(y,\theta+\delta) - x(y,\theta)\right]}{\sqrt{1+\left(\frac{dy}{dx}\right)^2\Big|_{y,\theta}}} \qquad \text{(B-11)}$$

where $\ell(y,\theta)$ is measured perpendicular to the shadow, and $\frac{dy}{dx}$ is obtained from Equation B-7 and is evaluated at the point of the penumbra at y and θ.

The relative intensity distribution through the penumbra is given[11] by

$$I(s) = \frac{3}{7} - \frac{3}{7\pi}\arccos\frac{2S}{\ell} + \frac{3}{7\pi}\left(\frac{2S}{\ell}\right)\sqrt{1-\left(\frac{2S}{\ell}\right)^2} + \frac{1}{7}\left(1+\frac{2S}{\ell}\right)^2\left(2-\frac{2S}{\ell}\right) \qquad \text{(B-12)}$$

where S is an element of length perpendicular to the shadow which can take the values $|S| \le \frac{\ell}{2}$, ℓ is the distance across the penumbra perpendicular to the shadow and is given by Equation B-11. The intensity distribution $I(S)$ has been normalized to give unity at the penumbra-sunlight interface. The intensity distribution $I(S)$ is plotted in Figure 5 in Section 2.1.1.

For craters of the order of 12 meters diameter, diameter to depth ratios ranging from 6 : 1 to 10 : 1, and phase angles of from 50° to 70°, the width of the penumbra is approximately a fifth of the resolution element expected on the moon's surface.

The intensity function for the sunlit floor of the crater depends upon the contours of the crater floor. The intensity function is proportional to the known lunar photometric function $\Phi(g,\alpha)$. The photometric function is a normalized reflection coefficient which is unity for perpendicular

incidence and reflection. The phase angle $g \equiv \frac{\pi}{2} - \theta$ and α is the angle in the phase plane between the observer ($+z$ direction) and the normal to the surface projected into the phase plane. Thus α must be determined at the point of interest.

For any spherical crater, the angle γ between the normal to the surface and the $+z$ direction is

$$|\cos\gamma| = \left(\frac{z-(a-d)}{a}\right) \tag{B-13}$$

Projecting the normal to the spherical surface into the phase plane gives

$$\tan\alpha = \tan\gamma\cos\phi \tag{B-14}$$

where ϕ is the polar coordinate angle with respect to the $+x$ direction in the xy plane. The sign of α is positive if the projection of the normal to the surface to the phase plane results in a vector pointing away from the sun and negative otherwise. Using Equation B-14 to obtain the $\tan\gamma$ and inserting it into Equation B-17 gives α in terms of x and y as

$$\tan\alpha = \frac{x}{\sqrt{a^2-x^2-y^2}} \qquad \begin{cases} 0 \le \alpha \le \frac{\pi}{2} \\ 0 \le \sqrt{x^2+y^2} \le \frac{D}{2} < a \end{cases} \tag{B-15}$$

The intensity function through the sunlit region can then be obtained by starting at the penumbra-sunlit interface (x_p, y_p) which from B-15 implies α_p . Using this α_p as a starting point the relative intensity along any path can be calculated from the equation

$$I_w(x,y) = \frac{\Phi(g,\alpha(x,y))}{\Phi(g,\alpha_p)} \tag{B-16}$$

The photometric function for a given phase angle g can be approximated by a polynominal equation in α as

$$\Phi(g, \alpha(x,y)) = b_0 + b_1 \alpha(x,y) + b_2 \alpha^2(x,y) + \cdots \qquad \text{(B-17)}$$

where the coefficients b_i depend only on the phase angle. The combining of Equations B-15, B-16, and B-17 gives the relative intensity function at all points on the sunlit part of the inside of the crater.

The maximum angle from the phase plane at which the edge can be scanned can be found in the following manner. For a given geometry and phase angle, the equation of the shadow (Equation B-7) intersects the rim of the crater $\left(x^2 + y^2 = \left(\frac{D}{2}\right)^2\right)$ at

$$x_c = (a-d)\tan\theta \qquad y_c = \pm\sqrt{\left(\frac{D}{2}\right)^2 - (a-d)^2\tan^2\theta} \qquad \text{(B-18)}$$

The tangent of the angle ψ which the normal to the shadow makes with the x axis is then given by

$$\tan\psi = -\left(\frac{dx}{dy}\right)_{x_c, y_c} \qquad \text{(B-19)}$$

Putting x from Equation B-7 into Equation B-19 gives

$$\tan\psi = -\frac{2y}{D}\left.\frac{\cos 2\theta}{\sqrt{1-\left(\frac{2y}{D}\right)^2}}\right|_{x_c, y_c} = \frac{-\cos 2\theta\sqrt{\left(\frac{D}{2}\right)^2 - (a-d)^2\tan^2\theta}}{(a-d)\tan\theta} \qquad \text{(B-20)}$$

Table B-1, computed from Equation B-20, shows the variation of ψ with typical phase angle, $g = \frac{\pi}{2} - \theta$, for two typical diameter to depth ratios.

TABLE B-1

MAXIMUM OFF-PHASE PLANE SCAN ANGLES

Phase Angle, g (Degrees)	D/d = 6 $\lvert\psi\rvert$ (Degrees)	D/d = 10 $\lvert\psi\rvert$ (Degrees)
50°	No Shadow	No Shadow
55°	7.5°	No Shadow
65°	39.0°	No Shadow
68°	48.4°	10.3
70°	54.1°	23.1
75°	66.2°	45.8
80°	75.5°	63.6

Experimentally, scanning directions must be confined to angles from the phase plane which are less than those shown in the table. For a phase angle in the range of 65° - 75°, it is therefore reasonable to expect that the maximum angle from the phase plane available for scanning would be 45°. In special cases, obstacles may cast shadows which can be employed to acquire data at larger angles.

APPENDIX C

DATA REDUCTION PROCEDURES

By M. J. Mazurowski

The data reduction computer program used to obtain the measures of detail rendition, namely, modulation transfer functions or line spread functions, is shown in schematic form in Figure 9.

Essentially the program utilizes input data obtained from micro-densitometer scans across lunar crater shadows, and across the pre-exposed edge targets on the SO-243 film, as well as auxiliary sensitometric data to obtain the modulation transfer function of each of the two linear elements of the Lunar Orbiter Photographic System. The actual numerical analysis techniques employed to perform the data analysis is described in this appendix.

Sensitometric Conversions

GRE Film. - The photographic data expected to be used for analysis will be copies of the GRE original film. A means must be provided for converting copy densities to GRE original densities. This can be done by exposing a series of known density values along with the GRE film when producing the copies or alternatively by measuring the densities of the controlled exposure steps in the pre-exposed edge data array on the GRE original film.

A subroutine of the computer program utilizes this data to relate the copy film densities to the GRE film densities through a quadratic equation whose coefficients a_i, $i = 0, 1, 2$, are obtained by a least squares procedure. The linear relationship between the GRE film densities and the SO-243 film transmittance is also needed to determine the relationship between copy film density and SO-243 film transmittance, viz.,

$$T_{SO243} = a_0 C + d + a_1 C D_{COPY} + a_2 C D_{COPY}^2 \qquad \text{(C-1)}$$

where the a_i's are quadratic coefficients and C and d are the parameters of the linear relationship between SO-243 film transmittance and GRE film density determined from the recorded gain settings of GRE system.

SO-243 Film. - The log exposure versus density curve for the SO-243 film is obtained by first converting the densities obtained from a scan across the 10 density steps in the pre-exposed edge data array on the GRE copy film to SO-243 film transmittance using equation C-1. These transmittance values are then converted to SO-243 film density values using

$$D_{243} = -\log T_{243} \qquad \text{(C-2)}$$

and a function of the form

$$D_{SO243} = c_1 + c_2 \operatorname{erf}\left(c_3 \log_{10}\left(c_4 + c_5 \frac{E}{E_0}\right)\right) \qquad \text{(C-3)}$$

is fitted to the data using an iterative process of differential correction to determine the proper values for the coefficients c_j, $j = 1, \cdots, 5$. The value of E_0 is determined as the exposure corresponding to a measured density D_0, in the image produced by a flat surface on the moon.

Determination of the Combined Scanner-Communications-GRS System Modulation Transfer Function

A scan across one of the edges in the image of the pre-exposed data arr y is used to evaluate the response of the combined scanner-communications-GRS system since these pre-exposed edges are degraded by only that portion of the photographic system*.

In the computational program, the initial density trace data is smoothed by convolving the data with a low pass filter. The smoothed density data is then converted to SO-243 film transmittance using Equation C-1** and then differentiated. The differentiation is accomplished by convolving the data with a function whose transform approximates that of an ideal differentiator. Both operations of smoothing and differentiation can be represented by the same computational form, namely,

$$\left.\begin{matrix} D(x_i) \\ \text{or} \\ D'(x_i) \end{matrix}\right\} = \sum_{k=-m}^{m} W_k D(x_{i-k}) \qquad \text{(C-4)}$$

where the W_k are the weightings corresponding to either a low pass filter or a differentiator and the $D(x_i)$ are the density values in the trace at the sample points x_i. In the program an 11 point smoothing filter (i.e., $m = 5$) is employed to eliminate some of the noise in the trace. The differentiation is done using transmittance rather than density as previously mentioned. In this operation an 11 point filter is also employed. The differentiation yields the line spread function which is then expanded as a Fourier series to convert to the corresponding modulation transfer function, viz.,

---

* There is some degradation of the edge data when it is pre-exposed on the SO-243 film. This degradation is accounted for in the analysis.

** The conversion to SO-243 film transmittance is not necessary since differentiation eliminates the constants of the conversion. This is done only as a matter of convenience.

$$L(x_i) = \frac{A_0}{2} + \sum_{n=1}^{\infty} A_n \cos n x_i + B_n \sin n x_i \qquad \text{(C-5)}$$

where

$$A_n = \frac{1}{\pi}\int_{-\pi}^{\pi} L(x) \cos nx \, dx$$

and

$$B_n = \frac{1}{\pi}\int_{-\pi}^{\pi} L(x) \sin nx \, dx .$$

The modulus and phase of the MTF are computed using

$$\tau_n = \frac{1}{2}\sqrt{A_n^2 + B_n^2} \qquad \text{(C-6)}$$

and

$$\phi_n = \arctan\left(\frac{B_n}{A_n}\right)$$

at frequencies equal to $\frac{n}{(N-1)\Delta x}$ where Δx is the interval used to sample the edge trace and N is the number of sampled points.

The modulus of the resulting MTF is divided by the correction MTF to account for the finite sharpness of the edge object. For convenience, the correction MTF shown in Figure 8 in the main text can be expressed by

$$\tau(\nu)_{\text{correction}} = 0.458\, e^{-0.01491|\nu|} + 0.542\, e^{-0.0001602\,\nu^2} \qquad \text{(C-7)}$$

Determination of the Camera System Modulation Transfer Function

The density values from a scan across the lunar shadow edge are converted to transmittance values using Equation C-1 and then transformed using a Fourier series expansion to obtain the amplitude and phase of the edge spectrum. Prior to taking the Fourier Transform of the edge trace, however, it is multiplied by a $\sin^2 Kx$ function in which K is adjusted so that the function is zero at the end points of the trace. This procedure is required to transform the original edge trace into a function with properties which insure existance of a Fourier transform. This is equivalent to convolving the actual edge spectrum with three closely spaced delta functions (the Fourier Transform of $\sin^2 Kx$) and only has a small effect on the spectrum at the lower spatial frequencies. The lunar target spectrum is then divided by the Modulation transfer function of the combined scanner-communications-GRS system to determine the spectrum of the target in terms of the transmittance of the SO-243 film. This spectrum is terminated at 100 lines per millimeter to remove the contribution of the noise to the spectrum. The inverse Fourier Transform is then taken and the $\sin^2 Kx$ function divided out to yield the image of the shadow edge as it would appear in transmittance on the SO-243 film. The corresponding SO-243 film density is computed and converted to exposure using Equation C-2. The resulting edge trace in exposure is again multiplied by a $\sin^2 Kx$ function and the Fourier Transform taken to obtain the spectrum of the edge in exposure. This spectrum is divided by the spectrum of an ideal shadow edge determined from the size of the crater, phase angle, shadow length and scan direction as described in Appendix B. When the resulting spectrum is normalized, it represents the modulation transfer function of the Lunar Orbiter camera system (lens-film) including any operational degradation (e.g., image motion, vibration or defocus) present in the image along the scan direction.

Finally, the inverse transform or the camera system line spread function is then obtained, and convolved with the combined scanner-communications-GRS system line spread function to obtain a total system line spread function for use in the evaluation of the system performance criteria.

APPENDIX D

NOISE ANALYSIS OF THE LUNAR ORBITER PHOTOGRAPHIC SYSTEM

A model for the noise analysis of the Lunar Orbiter photographic system is discussed in this appendix. The major problem is the development of an analytical model to represent the reconstruction of the one-dimensional noise signal as a two-dimensional array by the GRE kinescope. This problem is given primary attention at the beginning of this appendix and a solution presented. In this analysis all the noise inputs are assumed to be "white", statistically independent and represented by a gaussian random process. The discussion is divided into three sections. The first section is concerned with the reconstruction problem. The second section considers the nominal values of total noise power contributed by each component and how they are related to the total noise power in the GRE image, based upon the results of the first section. The final section outlines the computational program used to perform the noise analysis.

Reconstruction of the One-Dimensional Noise Signal

Techniques have been developed[12] for the conversion of two-dimensional isotropic random noise fields, such as the SO-243 film granularity, to one-dimensional fields when they are scanned by an aperture. Since many of the noise sources contribute in the time domain it is a relatively straightforward task to compute the spectrum or power of the noise signal $n(t)$ at the GRE kinescope surface by summing all the individual noise spectra or total noise powers. Once this has been done the problem of reconstruction of the noise signal in two dimensions is present.

This process can be represented by a weighted integral of $n(t)$ viz.

$$N(x', y') = \int_a^b h(t, x', y')\, n(t)\, dt \qquad \text{(D-1)}$$

This integral defines, under certain measurability conditions, a new random variable $N(x', y')$.[13] It remains, however, to show that $N(x', y')$ is a two-dimensional ergodic process so that its spectrum can be properly defined. This problem of the reconstruction of the one-dimensional noise signal is indeed difficult. In a recent article, T. Huang considered this very problem [14]. Although Huang concludes that the reconstructed noise can be reguarded as a "semi-discrete" ergodic random process and considers the spectrum of such a process, he does not explicitly consider a finite spread of the reconstructing scan spot but only casually mentions its effect without verification. It was also not explicitly stated if the resulting noise spectra included or did not include the "coherent noise" or line structure. As a result of these shortcomings an alternative approach to the solution of this problem is suggested in this appendix. In Appendix A it was shown that the combination of the PS scanner, communication and GRS system could be represented by a transfer function under such conditions that the coherent noise or line structure was removed from or neglected in the reconstructed image (either by sufficiently dithering the GRE spot or by optical filtering techniques). In other words, the portion of the Lunar Orbiter system from the transmittance of the SO-243 film to the density on the GRE film can be represented by a linear system. Therefore, a two-dimensional random process (noise field) at the SO-243 film plane can be transformed to a corresponding two-dimensional random process in the exposure plane of the kinescope. If the original noise field is stationary, the reconstructed noise field is also stationary.[13] In fact the noise power spectra are related by the expression

$$P_o(\nu) = |\tau(\nu)|^2 P_i(\nu) \qquad \text{(D-2)}$$

where $P_i(\nu)$ is the original noise power spectrum, $P_o(\nu)$ is the spectrum corresponding to the reconstructed signal and $\tau(\nu)$ is the frequency response or modulation transfer function of the linear system.

The grain of the SO-243 film is already a two-dimensional noise signal to which this analysis may be applied. The other noise sources shown in Figure 13 are one-dimensional random processes interjected at various points in the scanner-communications-reconstruction system. Suppose that each of these white noise sources is taken at its point of entry and projected back through the system so that it corresponds to a voltage fluctuation or noise signal in the scanner photomultiplier or equivalently a corresponding transmittance variation along a scan line on the SO-243 film. This can be done by dividing each white noise spectrum over its effective bandwidth by the square of the frequency response of all components between its point of entry and the SO-243 film. We may then add up all the individual noise spectra to determine an effective noise spectrum because all the original sources were considered to be independent and additive. The one-dimensional noise signal constructed in this manner can be imagined to originate from the scanning of a two-dimensional noise signal in the plane of the SO-243 film. Work previously completed at CAL [12] relates the one-dimensional spectrum $\phi(K)$ to the spectrum of the scanned two-dimensional isotropic random process by the integral equation.

$$P(\nu) = -\frac{1}{\pi}\frac{d}{d\nu}\int_{\nu}^{\infty}\frac{\phi(K)\,\nu}{K(K^2-\nu^2)^{1/2}}\,dK \quad . \tag{D-3}$$

Although the construction of such a two-dimensional noise field is artificial, it must be remembered that if this noise field did exist and were added to the random grain field, the resulting field when scanned in any arbitrary direction would produce at the GRE kinescope an identical ensemble of noise signals as each individual noise source operating independently. The "effective noise field" has the property that it can be transformed directly by using the square of the frequency response of the complete system to determine the spectrum of the noise signal reconstructed by the GRE kinescope. Obviously, this analysis does not include an effect of the "coherent

noise" or scan line structure since the requirement for employing the linear analysis was shown in Appendix A to be the minimization of such structure in the image.

Contributions by the Various Noise Sources

The type and location of the various noise sources in the photographic system shown previously in Figure 13 are those employed in D2-100293-1, "Picture Data Systems Analysis" made by the Boeing Company. Each noise source is discussed individually below. For convenience, the total white noise power contributed by each source is expressed in terms of the equivalent mean square deviation in voltage at the output of the Video Amplifier.

1. SO-243 Film Grain. - The grain of the SO-243 film is a two-dimensional random field which already exists in its desired form except for the degradation introduced by the gaussian PS scan spot. It is customary, in the case of film grain fields, to measure to square root of the mean square density deviation along a scan line, or granularity of the film, σ_D . These measurements are usually made using a circular aperture and not a gaussian aperture. Therefore, such measured values of granularity must be corrected not only for the size of the scanning spot but also for its shape or irradiance distribution. To compute the relationship between σ_D in the case of a circular aperture versus a gaussian spot, assume that the same two-dimensional grain field is degraded by both a circular aperture of radius r_0 which has a normalized frequency response given by

$$\tau(\nu) = 2J_1(2\pi r_0 \nu)/\pi r_0 \nu \qquad \text{(D-4)}$$

and by a gaussian spot with a normalized frequency response given by

$$\tau(\nu) = e^{-2\pi^2 \beta_1^2 \nu^2} \qquad \text{(D-5)}$$

The mean square deviation of the resulting two-dimensional random fields is given by

$$\sigma_D^2 = 2\pi \int_0^\infty |\tau(\nu)|^2 P(\nu) d\nu \qquad \text{(D-6)}$$

since $|\tau(\nu)|^2 P(\nu)$ represents the rotationally symmetric spectrum of the degraded two-dimensional random field. Assuming that the initial spectrum of the grain field is white, i.e., $P(\nu) = N_0$ for all ν, we find that from equation (D-6)

$$\sigma_D^2 = N_0 / 4\pi\beta_1^2 \qquad \text{(D-7)}$$

for the gaussian scanning spot and

$$\sigma_D^2 = N_0 / \pi r_0^2 \qquad \text{(D-8)}$$

as measured by a circular scanning aperture. Therefore, if we want to measure the mean square density fluctuation σ_D^2 due to the SO-243 film granularity, we should employ a circular aperture whose diameter is $4\beta_1$, where β_1 is the 1σ point of the gaussian scanning spot. Measurements of the value of σ_D as a function of the average density level on the SO-243 film has been supplied by Kodak [7] using a circular aperture whose diameter is as required above.

To determine σ_T^2, the mean square fluctuation in transmittance we may employ the approximation [9]

$$\sigma_T^2 = 5.3\, \bar{T}^2 \sigma_D^2 \qquad \text{(D-9)}$$

provided that ΔD and consequently $\sigma_D^2 = \overline{\Delta D^2}$ is small compared to one. For the current case, the error involved in employing the approximation is about 5%. Using the data supplied, the values of σ_T^2 were computed for the various average density levels and are shown in Table (D-1).

TABLE D-1

$\sigma_{\bar{T}}^2$ VS. $\bar{D}$ FOR SO-243 USING THE LUNAR ORBITER PS SCANNER

$\bar{D}$	$\bar{T}$	$\sigma_{\bar{T}}^2$
.3	.501	1.13×10^{-4}
.4	.398	8.87×10^{-4}
.5	.316	6.18×10^{-4}
.6	.251	6.03×10^{-4}
.7	.200	4.52×10^{-4}
.8	.158	3.17×10^{-4}
.9	.126	2.06×10^{-4}
1.0	.100	1.35×10^{-4}
1.1	.079	9.06×10^{-5}
1.2	.063	6.03×10^{-5}
1.3	.050	3.94×10^{-5}

Including the degradation introduced by the gaussian scan spot the contribution to the effective noise power density due to the SO-243 granularity becomes

$$P_1(\nu) = 4\pi\beta_1^2\sigma_1^2 e^{-4\pi^2\beta_1^2\nu^2} \qquad \text{(D-10)}$$

where $\sigma_1^2 = \sigma_T^2 G^2$ and G represents the gain of the system from SO-243 film transmittance to GRE input voltage. (Nominally G = 10 volts/unit transmittance.)

2. Line Scan Tube Phosphor Noise. - This noise source is similar to the SO-243 film grain in that it already exists at the film plane and is degraded by the PS scan spot. The nominal total noise power σ_2^2 contributed by this source at its entry point is 2500 square millivolts [7].

If the effective bandwidth in which this contribution is made is $2\nu_o$ in each dimension, the corresponding spectrum $P_2(\nu)$ becomes

$$P_2(\nu) = \frac{\sigma_2^2}{(2\nu_o)^2} e^{-4\pi^2\beta_1^2\nu^2} \qquad \text{(D-11)}$$

where the effect of the response of the degrading PS scan spot has been included and $\nu_o \approx 100$ lines/mm.

3. Photomultiplier Shot Noise. - The photomultiplier shot noise is not subject to degradations when projected to the SO-243 film plane. A problem arises, however, when one attempts to convert the one-dimensional white noise source into two-dimensions by employing expression (D-3) in a direct manner. Assuming $\phi(K) = \frac{P_o}{2\nu_o}$ for $|K| \le \nu_o$ and zero otherwise, the formal solution for $P_3(\nu)$ becomes

$$P_3(\nu) = \frac{P_o}{2\pi\nu_o(\nu_o^2 - \nu^2)^{1/2}} \qquad 0 \le \nu \le \nu_o \qquad \text{(D-12)}$$

where P_o is the total noise power in either the one-dimensional or two-dimensional spectrum. Unfortunately, the resulting spectrum diverges at $\nu = \nu_o$. To avoid this problem it is convenient to approximate $P_3(\nu)$ by retaining the first few terms in a series expansion viz.

$$P_3(\nu) = \frac{4P_o}{5\pi\nu_o^2}\left[1 + \frac{1}{2}\left(\frac{\nu}{\nu_o}\right)^2\right] \qquad 0 \le \nu \le \nu_o \qquad \text{(D-13)}$$

where normalization such that the total noise power in the spectrum remains constant equal to P_o has been employed. The one-dimensional spectrum corresponding to this two-dimensional spectrum is given by

$$\phi(K) = \frac{4P_o}{5\pi\nu_o}\left\{\left[2 + \left(\frac{K}{\nu_o}\right)^2\right]\left[1 - \left(\frac{K}{\nu_o}\right)^2\right]^{1/2} + \frac{1}{3}\left[1 - \left(\frac{K}{\nu_o}\right)^2\right]^{3/2}\right\} \quad |K| \le \nu_o \quad \text{(D-14)}$$

Figure (D-1) is a comparison of the approximations given by expressions (D-13) and (D-14) to the directly determined spectra. It is seen that

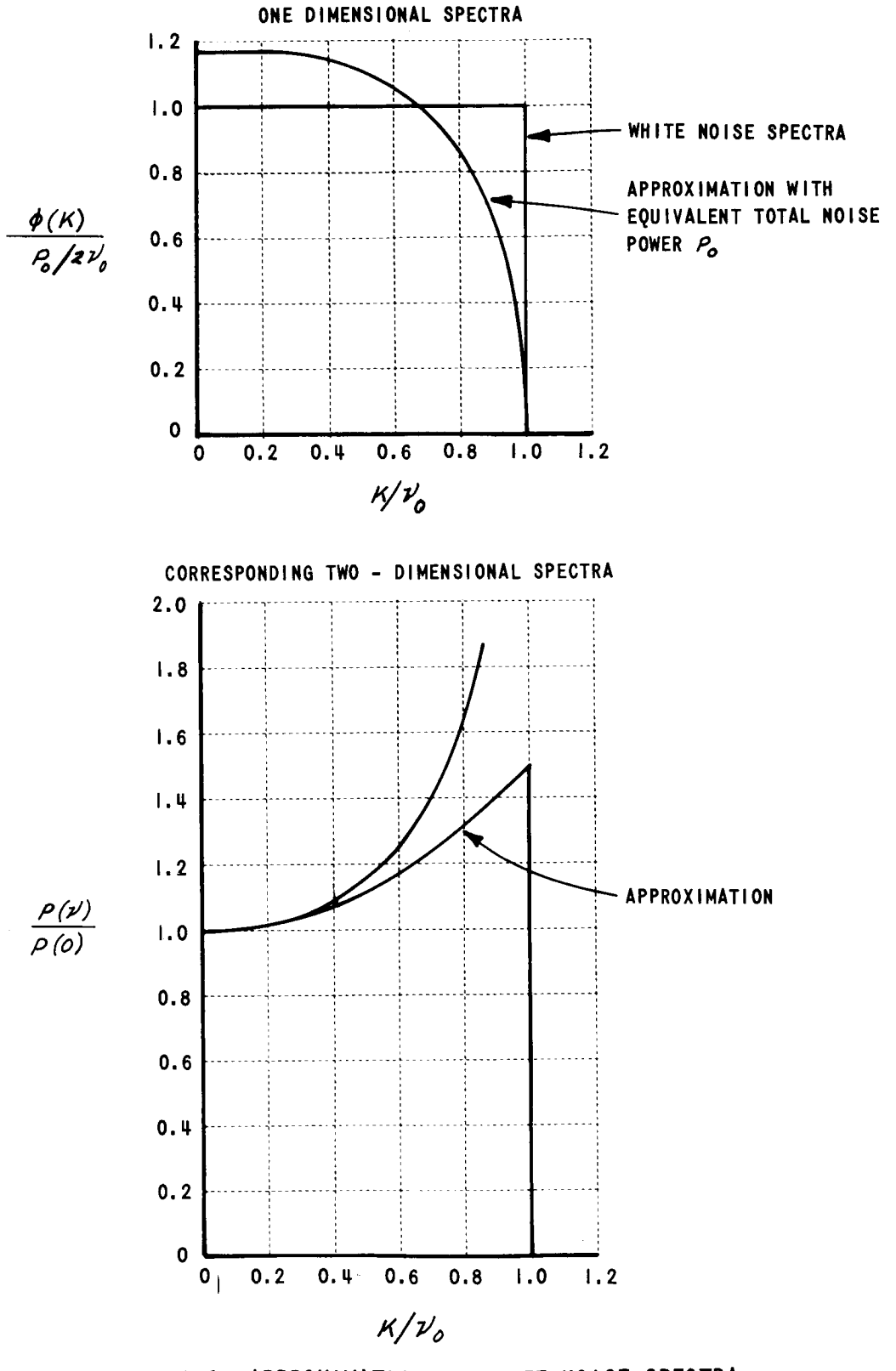

Figure D-1 APPROXIMATION TO WHITE NOISE SPECTRA

$\phi(\kappa)$ in Equation (D-14) adequately represents the one-dimensional white noise spectrum and the two-dimensional spectrum is finite everywhere. The spectrum of shot noise projected back to the SO-243 film plane is represented by a spectrum of the form

$$P_3(\nu) = \frac{4\sigma_3^2}{5\pi\nu_0^3}\left[1+\frac{1}{2}\left(\frac{\nu}{\nu_0}\right)^2\right] \qquad 0 \le \nu \le \nu_0 \qquad \text{(D-15)}$$

where σ_3^2 is the total noise power due to shot noise and has a nominal value of 906 square millivolts.[7]

4. Video Amplifier Noise. - Two pre-emphasis filters are assumed to be located between the noise input of the video amplifier and the SO-243 film plane. These filters are accounted for by dividing the square of the frequency response of each of these filters shown in Figure D-2 into the white noise spectrum. The resulting spectrum is then converted to the corresponding effective two-dimensional spectrum by employing expression (D-3). Because an analytical expression for the resulting spectrum is not available, the conversion had to be done numerically and is described in more detail in the last section of this appendix. The total noise power, σ_4^2, of this source is nominally 2.36 square millivolts and assumed to exist over a total bandwidth of 200 lines/mm.

5. Data Link Noise. - The data link noise must be corrected for the data link frequency response, the video amplifier response and the pre-emphasis filter responses when projected back to the SO-243 film plane. The frequency response for the data link and the video amplifier were assumed to be those given in Figures 12 and 13 of Reference 7. The nominal value of the total noise power of the data link, σ_5^2, is taken to be 22 800 square millivolts over a 200 line/mm bandwidth.

6. Kinescope Phosphor Noise. - The noise in the kinescope phosphor introduces phosphor streaking in the GRE image. This noise is located entirely in the electrical scan direction. Because this noise source is located at the reconstruction plane it does not have to be projected back through the entire system. Instead, its spectrum can be added to the spectrum contributed by sources (1) through (5) after they have been summed

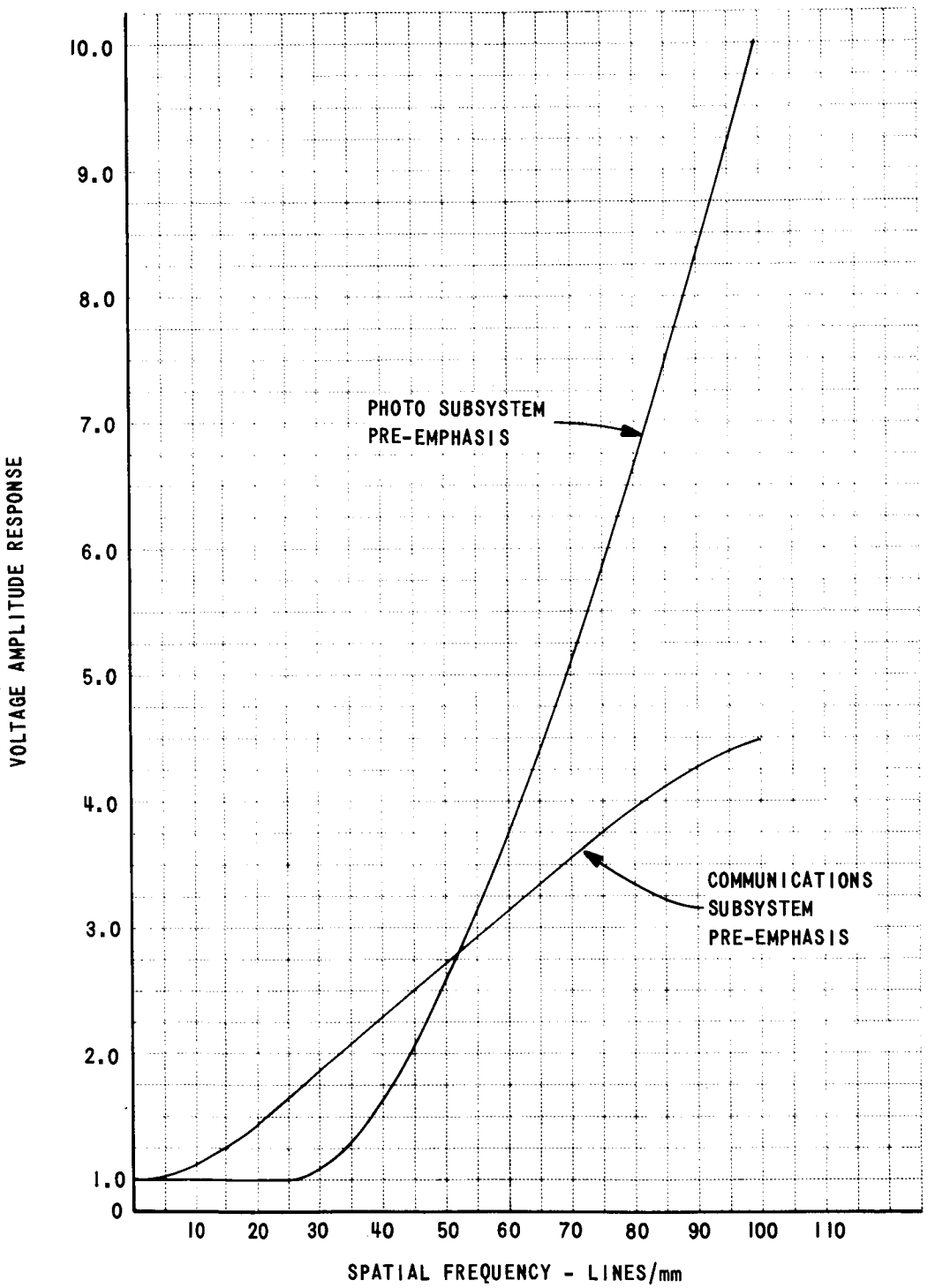

Figure D-2 PRE-EMPHASIS FILTERS

and multiplied by the square of the response of the overall scanner-communications-GRS systems. The Kine phosphor noise spectrum should include the gaussian shape of the reconstructing gaussian scan spot. If σ_6^2 , the total power of the Kine phosphor noise is located in a bandwidth $2\nu_o$ its spectrum is given by

$$P_6(\nu) = \frac{\sigma_6^2}{2\nu_o} e^{-4\pi^2\beta_1^2\nu^2} \qquad \text{(D-16)}$$

Nominally σ_6^2 is assumed to be 2500 square millivolts[7] and ν_o = 100 lines/mm.

7. Type 5374 Film Grain. - Again, the 5374 film grain need not be projected back through the system because it exists at the reconstruction plane. It is assumed to be white. Given the total noise power σ_0^2 measured by a circular aperture of radius r_o , it is only necessary to convert this to the equivalent GRE input voltage and compute the corresponding white noise power density by correcting for the measuring aperture. The computation is given previously by expression (D-8) namely

$$P_7(\nu) = \pi r_o^2 \sigma_7^2$$

for all ν where σ_7^2 is the equivalent total noise power of the 5374 film grain expressed in voltage squared. Nominally σ_7^2 is 25 square millivolts measured by a 47.7 micron aperture.[7]

Computational Program

The calculation of the noise spectrum of the reconstructed image requires numerical evaluation. This section of the appendix describes the IBM 7044 program written to perform these calculations. The flow diagram of the program is given in Figure D-3. The program computes the spectrum cross-section of the two-dimensional noise field for both the electrical and mechanical scan directions. It also computes the one-dimensional spectra

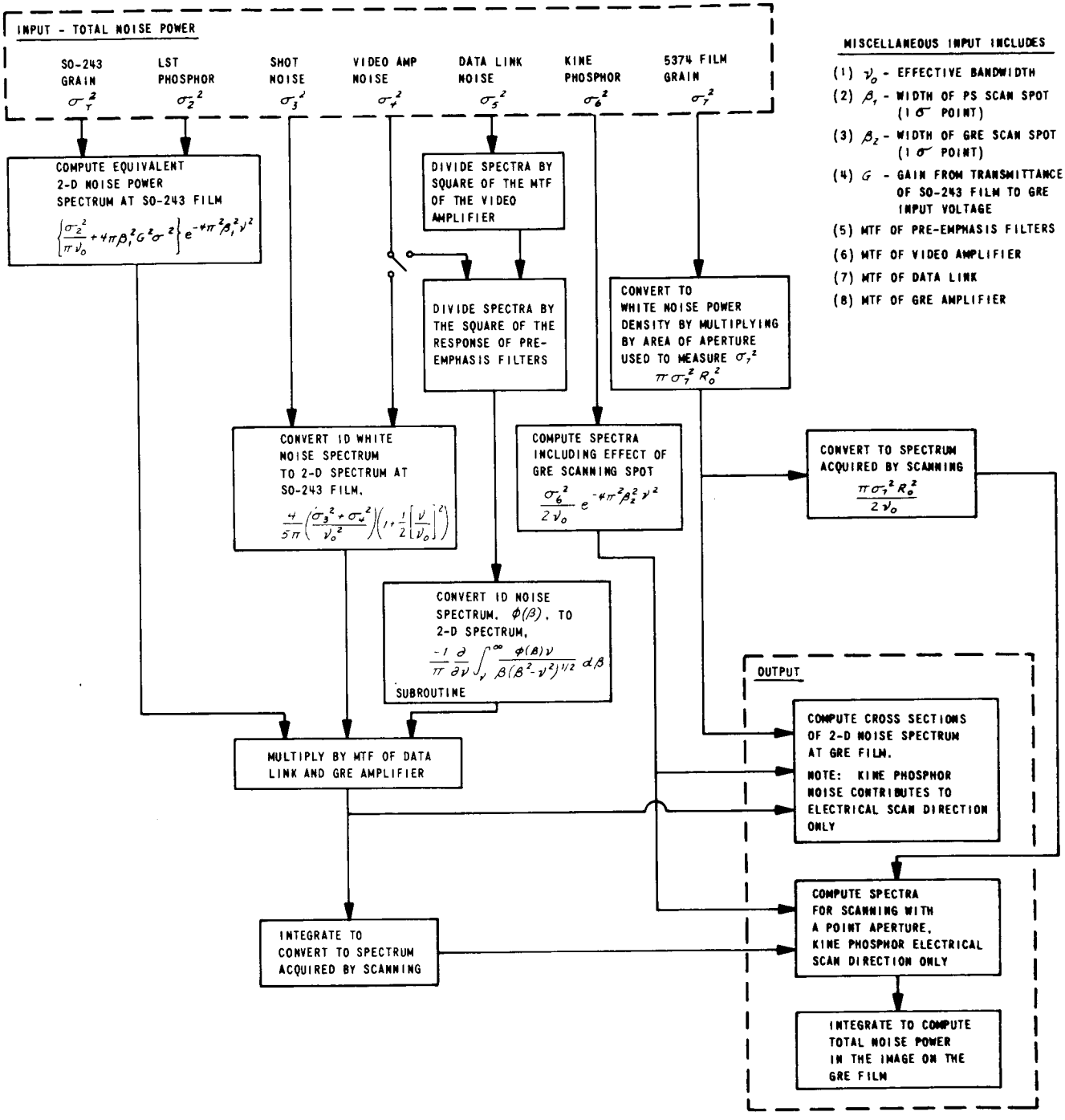

Figure D-3 NOISE COMPUTATION PROGRAM FLOW DIAGRAM

originating from scanning the two-dimensional noise field in these directions and the total noise power in the image. Several important questions to be answered by performing these computations include: (1) To what degree can the resulting noise spectra be regarded as white? and (2) What is the corresponding constant noise power density?

The primary inputs in the program are the values of the total noise power contributed by each noise source at its origin. The data link noise, video amplifier noise and photomultiplier shot noise are projected back to construct a two-dimensional effective noise field at the SO-243 film plane using the appropriate expressions described in the previous section. The integral equation given by equation (D-3) used to construct the two-dimensional noise spectrum from the one-dimensional noise spectrum was written as an individual subroutine. The integral equation, apart from the application used in this study, represents the relationship between a line spread function and the corresponding symmetrical point spread function. This has resulted in the development of a more convenient computational form[15] than that given by expression (D-3), namely

$$P(\nu) = -\frac{1}{\pi}\int_0^\infty \frac{\phi'\left(\sqrt{K^2+\nu^2}\right)}{\sqrt{K^2+\nu^2}}\,dK \qquad \text{(D-17)}$$

where $\phi'(K)$ is the derivative of the one-dimensional noise spectrum at the SO-243 film plane. The derivative was taken using a five-point differentiating filter in the subroutine. The effective two-dimensional noise spectra, due to the data link noise, video amplifier noise and photomultiplier shot noise computed using this subroutine, are added to the noise spectra of the SO-243 film grain and the LST phosphor to determine the total spectrum at the SO-243 film plane. This spectrum is then converted to the GRE film plane by employing the frequency response of the communication system and the GRE scan spot (including wobble). The resulting noise spectrum is finally added to the combined spectrum due to the 5374 film grain and the kinescope phosphor noise to determine the total two-dimensional noise spectrum in the image. It should be noted that the kinescope phosphor noise is one-dimensional, occurring in the electrical scan direction. Computations were made using the nominal values of the parameters shown in Table D-2.

TABLE D-2

NOMINAL PARAMETER VALUES

Parameter	Symbol	Nominal Value
Total Noise		
SO-243 Film Grain	σ_1^2	3.17×10^{-4} at $D_{AVE} = 0.8$
LST Phosphor	σ_2^2	2500 square millivolts
Shot Noise	σ_3^2	906 " "
Video Amplifier	σ_4^2	2.36 " "
Data Link	σ_5^2	22 800 " "
Kine Phosphor	σ_6^2	2500 " "
5374 Film Grain	σ_7^2	25 " "
PS Scan Spot Width	β_1	1.62 μ
GRE Scan Spot Width	β_2	1.25 μ
Gain	G	10^4 millivolts/transmittance
Bandwidth	ν_0	100 lines/mm

Most of these values are taken from Reference 7. Figures (D-4) and (D-5) show the results of these computations. From Figure (D-5) it can be seen that the one-dimensional spectra obtained by scanning with a point aperture can be adequately approximated by a white noise spectra over the bandwidth considered in the analysis. The white noise assumption employed in the derivation of the error measures σ_α and σ_l in Appendix E is reasonable. The nominal value of the total noise power is 43,800 square millivolts expressed in terms of the input voltage to the GRS. This corresponds to $\sigma_D^2 = 0.0034$ on the GRE film for nominal operation. To evaluate the total noise power for off-nominal performance one must realize that the total noise power in the image is directly proportional to the noise power contribution by each of the independent sources. Figure 22 of the main text shows the contribution to the total noise power of the image for

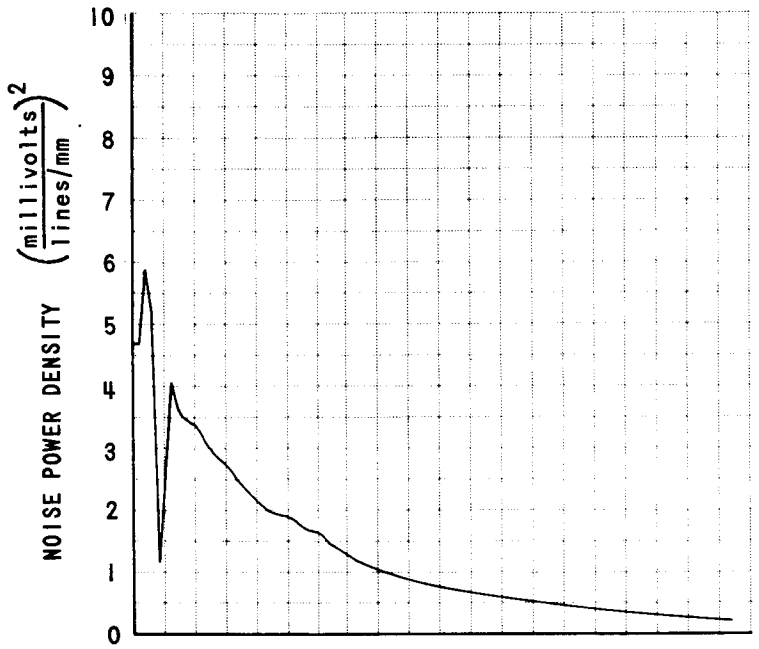

a) MECHANICAL SCAN DIRECTION

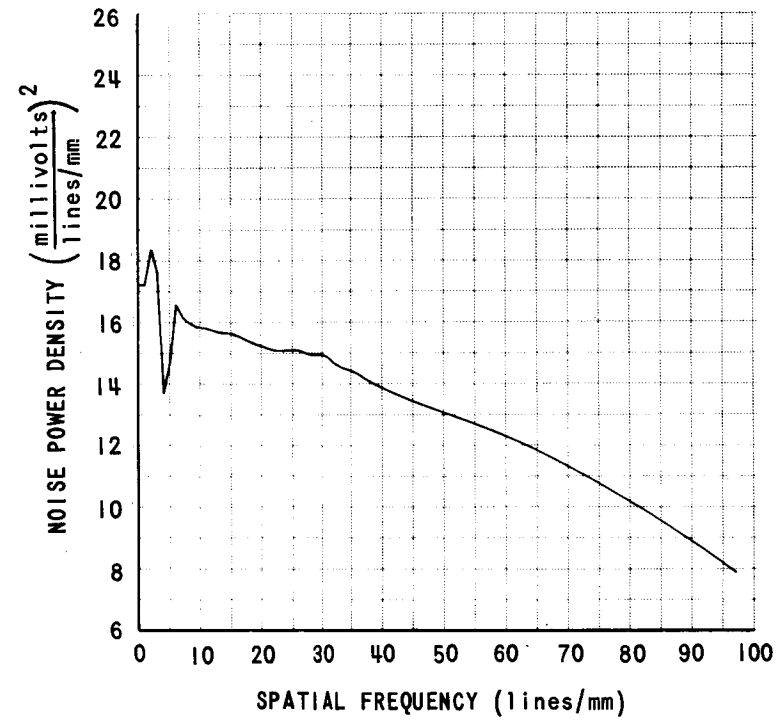

b) ELECTRICAL SCAN DIRECTION

Figure D-4 CROSS-SECTION OF TWO DIMENSIONAL NOISE SPECTRA (NOMINAL OPERATION)

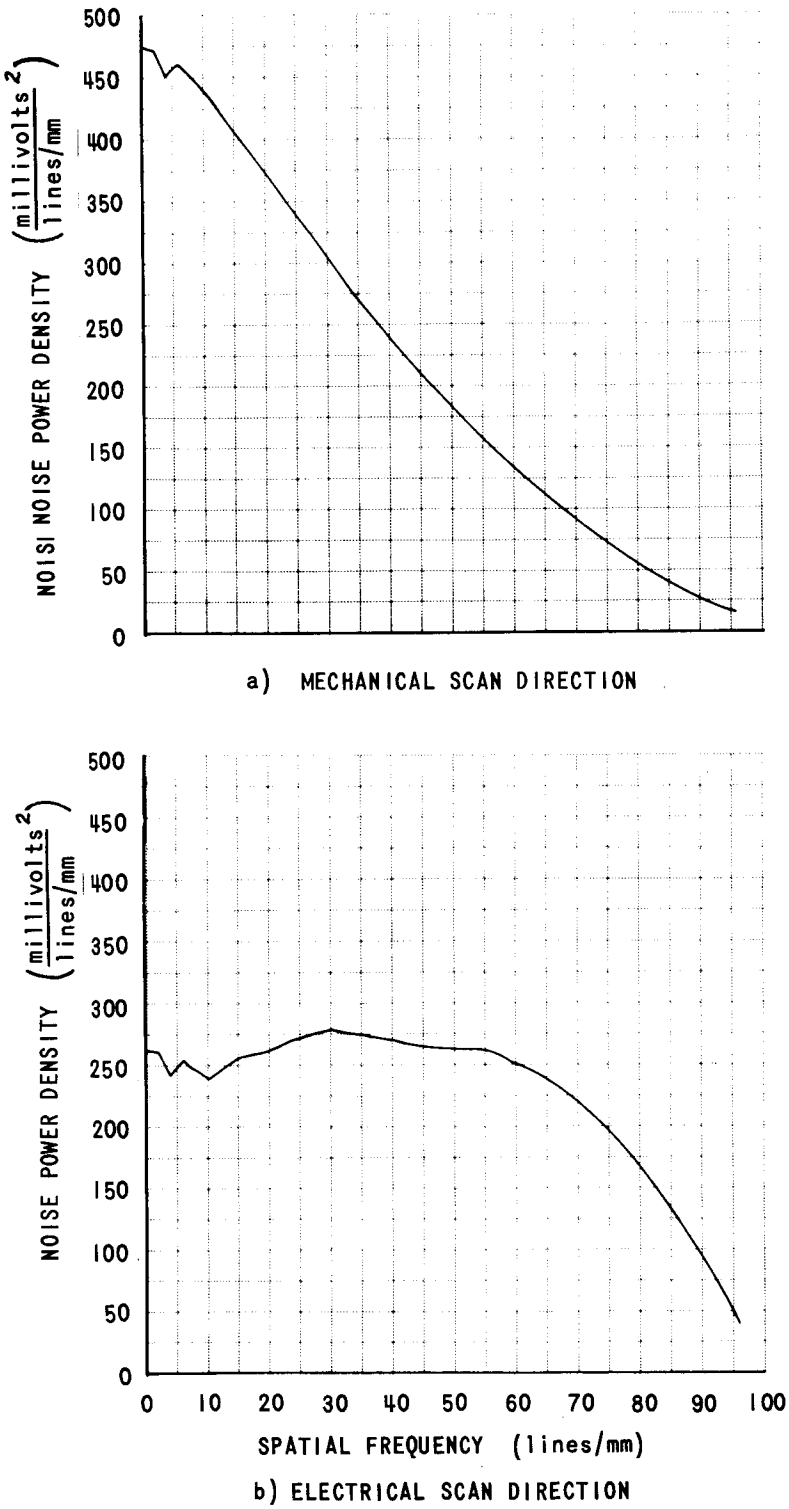

Figure D-5 ONE-DIMENSIONAL NOISE SPECTRA OBTAINED BY POINT SCANNING

each of the noise sources except the video amplifier noise which is negligible. By adding the contribution of each noise source, the total noise power for off-nominal conditions can be determined. The spectra, on the otherhand, change shape with off-nominal conditions and should be evaluated in each case of interest.

APPENDIX E

DERIVATION OF MEASURES OF SLOPE ESTIMATION

By H. B. Hammill and E. A. Trabka

A procedure is given in this appendix for estimating the greatest accuracy with which parameters of terrain profiles may be estimated from Lunar Orbiter photographs. This procedure is illustrated for the two parameter family of terrain profiles shown in Figure 17 in the report, consisting of constant slopes of inclination α_0 for a distance ℓ . Although it is not essential that the photographic system be represented by a linear system, such a representation greatly simplifies the required calculations. General expressions are derived, and the linear approximation is made to relate these expressions to the system quality measures.

The Model

One convenient mathematical description of the Lunar Orbiter system for extracting topographic information is shown in Figure E-1. We start with terrain profiles $H(x;\vec{\theta})$ corresponding to scans in a certain direction with distance measured by x . These profiles correspond to a family of targets indexed by the vector parameter set $\vec{\theta} = (\theta_1, \theta_2, \cdots \theta_n)$. The photometric function Φ of the lunar surface would yield an exposure $E(x;\vec{\theta})$ in the absence of degrading effects of the lens-film modulation transfer function (MTF). However, because of these effects the actual exposure $E_S(x;\vec{\theta})$ of the film in the satellite is linearly related to $E(x;\vec{\theta})$. This linear operation is represented by the integral operator L_1 . A (zero-memory) non-linear operation Γ converts $E_S(x;\vec{\theta})$ to film transmittance in the satellite. The scanner and communication system are represented by another linear operation L_2 giving an output $F(x;\vec{\theta})$ which we assume to be contaminated by additive noise before yielding an exposure $E_G(x;\vec{\theta})$ in the Ground Reconstruction System. Hence, the transformations from E to E_G may be

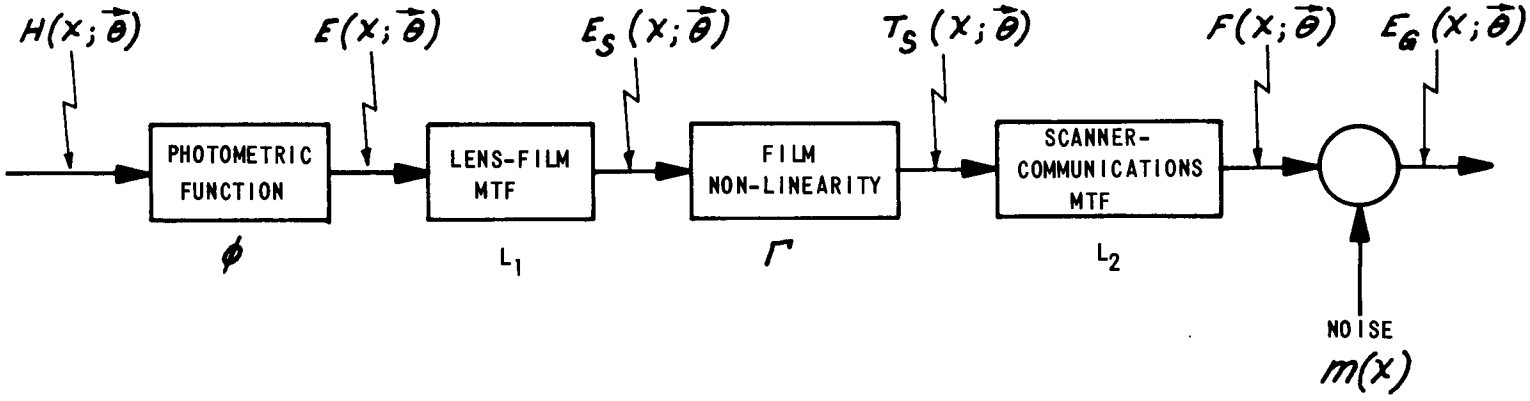

Figure E-1 MATHEMATICAL MODEL OF LUNAR ORBITER SYSTEM FOR EXTRACTING TOPOGRAPHIC DATA

described by the equations

$$F(x;\vec{\theta}) = L_2 \Gamma L_1 \left\{ E(x;\vec{\theta}) \right\}$$
$$E_G(x;\vec{\theta}) = F(x;\vec{\theta}) + n(x) \qquad \text{(E-1)}$$

Of particular relevance to the Lunar Orbiter mission are the family of input exposures $E(x;\vec{\theta})$ which arise from the two parameter family of terrain profiles $H(x;\alpha_0,\ell)$ shown in the report in Figure 17 in which

$$\vec{\theta} = (\theta_1,\theta_2) = (\alpha_0,\ell) \qquad \text{(E-2)}$$

It seems appropriate and reasonable to base the measure of the degree of success of the feature extraction phase of the Lunar Orbiter mission on the theoretical inherent accuracy with which parameter estimates may be made of a relatively simple family of targets, such as that described above.

A particularly attractive estimation procedure, and one for which accuracy formulas are available, is that based on the method of maximum likelihood (References 16 and 17). We will first discuss the accuracy of maximum likelihood estimates of target parameters based on observation of $E_G(x;\vec{\theta})$. Next, we will establish the dynamic range of the recorded signal by examining the relationship between $H(x;\vec{\theta})$ and $E(x;\vec{\theta})$. Finally, in order to gain some insight into how the photographic system parameters affect the estimation accuracy we will derive expressions which can be interpreted as typical for systems in which the effect of interchanging the order of Γ and L_1 is negligible ($L_2 \Gamma L_1 \approx L_2 L_1 \Gamma$). We begin by describing maximum likelihood estimation briefly.

Maximum Likelihood Estimation

With known noise statistics, it is reasonable to consider the probability of obtaining a given output exposure E_G if the input is due to a target with label $\vec{\theta}$. Let this probability be denoted by $P(E_G;\vec{\theta})$. For a given observation E_G, $P(E_G;\vec{\theta})$ considered as a function of $\vec{\theta}$ is known as the likelihood function. Maximum likelihood estimates $\hat{\vec{\theta}}$ are those values of $\vec{\theta}$ which maximize the likelihood function $P(E_G;\vec{\theta})$ given the observation E_G , i.e., $\hat{\vec{\theta}}$ is determined by

$$P(E_G ; \hat{\vec{\theta}}) = \underset{\vec{\theta}}{MAX}\, P(E_G ; \vec{\theta}) \qquad \text{(E-3)}$$

Let $\tilde{\vec{\theta}}$ denote the true value of $\vec{\theta}$ which resulted in the observation E_G. The component covariances of the maximum likelihood estimate are given by

$$\langle (\hat{\theta}_i - \tilde{\theta}_i)(\hat{\theta}_j - \tilde{\theta}_j) \rangle_{AVG} = (A^{-1})_{ij} \qquad \text{(E-4)}$$

where $(A^{-1})_{ij}$ is the inverse matrix corresponding to A_{ij} with

$$A_{ij} = \frac{1}{\psi} \int_{x_1}^{x_2} \frac{\partial F(x;\vec{\theta})}{\partial \theta_i} \frac{\partial F(x;\vec{\theta})}{\partial \theta_j} dx \qquad \text{(E-5)}$$

and x_1 and x_2 are reasonable limits beyond $\pm \frac{|\ell|}{2}$. In writing (E-4) and (E-5), it has been assumed that the noise is white and gaussian with ψ being the constant noise power per unit bandwidth of the double-sided spectrum. Other more general formulas, together with a comprehensive discussion of their applicability, are given by Swerling (Reference 17). For example, in certain cases, classifical least squares estimation also yields (E-4) and(E-5).

Actually, the formulas (E-4) and E-5) give lower bounds in general. However, if a minimum variance unbiased estimate (efficient estimate) exists, the method of maximum likelihood will yield this estimate. In any case, we will not concern ourselves here with how this estimate may be obtained in practice, but only with the limiting accuracy of the estimates as given by the variances obtained from (E-4) and (E-5). For example, in the case of the parameter vector given by Equation (E-2) and corresponding to the target family depicted in Figure 17, we would be interested in the variances

$$\left.\begin{aligned} \sigma_{\alpha_0}^2 &= (A^{-1})_{11} = \frac{A_{22}}{\Delta} \\ \sigma_{\ell}^2 &= (A^{-1})_{22} = \frac{A_{11}}{\Delta} \end{aligned}\right\} \qquad \text{(E-6)}$$

in which

$$\Delta = A_{11} A_{22} - A_{12}^2 \qquad \text{(E-7)}$$

and the elements of the A matrix are given by

$$A_{11} = \frac{1}{\psi}\int_{x_1}^{x_2}\left(\frac{\partial F}{\partial \alpha_o}\right)^2 dx$$

$$A_{22} = \frac{1}{\psi}\int_{x_1}^{x_2}\left(\frac{\partial F}{\partial \ell}\right)^2 dx \qquad \text{(E-8)}$$

$$A_{12} = A_{21} = \frac{1}{\psi}\int_{x_1}^{x_2}\left(\frac{\partial F}{\partial \alpha_o}\right)\left(\frac{\partial F}{\partial \ell}\right) dx$$

In order to apply the evaluation proposed above, we need only be able to calculate the output $F(x;\vec{\theta})$ for the input signal corresponding to each $\vec{\theta}$.

Signal Recording in the Spacecraft

It is now essential to establish the relationship between terrain profiles, such as $H(x;\vec{\theta})$ in Figure 17 and the exposure $E(x;\vec{\theta})$. The following formulation is based on the concepts and procedures defined in References 18 and 19.

Assuming scans in the direction of the sun, the angle, usually denoted by α , between the surface normal and the line of sight when projected on the plane of the phase angle* g , measures the inclination of the terrain (see Figure 17 of Reference 18) and is given by

$$\alpha(x) = \arctan\frac{dH(x)}{dx} \qquad \text{(E-9)}$$

so that our earlier use of α_o as a parameter** in the family of targets defined by Figure 17 is consistent with (E-9).

The ideal illuminance of the satellite film due to light reflected from the moon is

---

* Angle between line of sight and sun line.

** In order to avoid extracting topographic information in shadows, we assume that for positive α, $\alpha < \frac{\pi}{2} - g$.

$$B(\alpha) = \frac{\rho_o B_o}{\pi} \Phi(\alpha; g) \qquad \text{(E-10)}$$

where ρ_o is the reflectance coefficient of the moon for normal incidence, B_o is the mean solar constant at the moon's surface, $\Phi(\alpha; g)$ the photometric function of the moon as a function of α for a given phase angle g .

We have found that $\Phi(\alpha; g)$ may be adequately represented by a polynomial

$$\Phi(\alpha; g) = a_o(g) - a_1(g)\alpha - a_2(g)\alpha^2 \qquad \text{(E-11)}$$

where a_o, a_1, a_2 are all positive. Since the target of interest is:

$$\alpha(x; \vec{\theta}) = \alpha_o \, rect\left(\frac{x}{|\ell|}\right) \qquad \text{(E-12)}$$

where α_o on the right hand side of (E-12) is a constant and we have used Woodward's rectangle function by

$$rect\ \mu = \begin{cases} 1 & \left(|\mu| \le \frac{1}{2}\right) \\ 0 & \left(|\mu| > \frac{1}{2}\right) \end{cases} \qquad \text{(E-13)}$$

it becomes possible to write the exposure on the spacecraft film (before effects of lens-film MTF) as

$$E(x; \alpha_o, \ell) = E_o + (\Delta E)\, rect\left(\frac{x}{|\ell|}\right) \qquad \text{(E-14)}$$

where E_o is the exposure for $\alpha = 0$, and (ΔE) is the (constant) difference between the exposure E_o and the exposure for an inclination α_o .

The Linear Approximation

For small values of α_o , ΔE will not be very large, and it becomes reasonable to assume that both MTF's shown in Figure E-1 can be assumed to act together, and that the exposure, E , may be carried through the film non-linearity before the MTF effect is taken into account. The value of E_o is proportional to a_o of equation E-11 and ΔE is

$$\Delta E = E(\alpha_o) - E_o \qquad \text{(E-15)}$$

where $E(\alpha_o)$ is also evaluated from E-11 for angle α_o , with the same constant of proportionality as E_o .

It has been shown (see report Section 4.2 and Appendix G) that a good fit to the SO-243 film T-log E curve is an error function, and that the film transmittance can therefore be written

$$T(\alpha) = 10^{-(C_1 + C_2 \operatorname{erf}\{C_3 \log_{10}[C_4 + C_5 \frac{\Phi(\alpha)}{\alpha_o}]\})} \qquad \text{(E-16)}$$

where $C_{1,2,3,4,5}$ are constants of the fitting process. Thus, a $T(\alpha_o)$ and a T_o can be calculated from E-16, corresponding to $E(\alpha_o)$ and E_o of E-15. Similarly, it has also been shown (see Section 2.2) that the density, D , on the GRE is related to $T(\alpha)$ by

$$D(\alpha) = \gamma T(\alpha) \qquad \text{(E-17)}$$

where γ is evaluated from Figure 11 or the comparable curve for the operating system. Thus, a D_o and ΔD can be computed corresponding to the E_o and ΔE given above, and

$$D(x; \alpha_o, \ell) = D_o + (\Delta D)\, rect\left(\frac{x}{|\ell|}\right) . \qquad \text{(E-18)}$$

The effect of the system MTF is now included, and $F(x; \alpha_o, \ell)$ to be used in equation (E-8) is written

$$F(x; \alpha_o, \ell) = \int_{-\infty}^{\infty} L(x - x')\, D(x'; \alpha_o, \ell)\, dx' . \qquad \text{(E-19)}$$

where $L(x)$ is the Fourier transform of the system MTF $[\tau(\nu)]$, or

$$L(x) = \int_{-\infty}^{\infty} \tau(\nu)\, e^{2\pi i \nu x}\, dx . \qquad \text{(E-20)}$$

The elements A_{11}, A_{12}, and A_{22} in equation (E-8) can now be evaluated. The derivatives of $F(x;\alpha_o,\ell)$ are needed. The derivative evaluated from E-18 and E-19 are

$$\frac{\partial F}{\partial \alpha_o} = \frac{\partial \Delta D(\alpha_o)}{\partial \alpha_o} \int_{-\infty}^{\infty} L(x-x')\, rect\left(\frac{x'}{|\ell|}\right) dx' \qquad \text{(E-21)}$$

$$\frac{\partial F}{\partial \ell} = \Delta D(\alpha_o) \int_{-\infty}^{\infty} L(x-x') \frac{\partial}{\partial \ell}\left[rect\left(\frac{x'}{|\ell|}\right)\right] dx' \,. \qquad \text{(E-22)}$$

Employing equations E-16 and E-17, $\frac{\partial \Delta D}{\partial \alpha_o}$ can be written

$$\frac{\partial \Delta D(\alpha_o)}{\partial \alpha_o} = \gamma \frac{\partial T}{\partial \alpha_o} = \gamma \left(-\frac{C_2 C_3 C_5}{a_o \sqrt{2\pi}}\right)\left(\frac{T(\alpha_8)\, e^{-\frac{1}{2}\left[C_3 \log_{10}\left\{C_4 + C_5 \frac{\Phi(\alpha_8)}{a_o}\right\}\right]^2} (a_1 + 2a_2\alpha_o)}{C_4 + C_5 \frac{\Phi(\alpha_8)}{a_o}}\right). \qquad \text{(E-23)}$$

However, one problem remains in computing the partial derivations, namely the evaluation of

$$\frac{\partial}{\partial \ell}\left[rect\left(\frac{x'}{|\ell|}\right)\right] \,. \qquad \text{(E-24)}$$

The absolute value signs on ℓ can be eliminated, if we remember in the following analysis that negative ℓ values have no physical significance. In order to differentiate rect $\left(\frac{x'}{|\ell|}\right)$ with respect to ℓ, the function must be written as a function of ℓ. Recalling the definition of the rect function from equation E-13, the significant relation is:

$$\left|\frac{x'}{|\ell|}\right| < \frac{1}{2} \qquad \text{(E-25)}$$

or

$$2|x'| < |\ell| \qquad \text{(E-26)}$$

Thus, rect $\left(\frac{x'}{|\ell|}\right)$ is unit over all ℓ except between $\pm 2|x'|$. This function can be written as

$$rect\left(\frac{x'}{|\ell|}\right) = 1 - rect\left(\frac{\ell}{4|x'|}\right) \,. \qquad \text{(E-27)}$$

Now, the partial derivative with respect to ℓ becomes

$$\frac{\partial}{\partial \ell}\left[rect\left(\frac{x'}{|\ell|}\right)\right] = -\delta(\ell+2|x'|)+\delta(\ell-2|x'|) \qquad \text{(E-28)}$$

where $\delta(\mu)$ is the Dirac delta function. Each zero argument of a delta function occurs at an edge of the rect function. Rewriting E-28 in terms of x' instead of ℓ, and maintaining normalization of the delta function, yields

$$\frac{\partial}{\partial \ell}\left[rect\left(\frac{x'}{|\ell|}\right)\right] = \frac{\delta\left(|x'|-\frac{\ell}{2}\right) - \delta\left(|x'|+\frac{\ell}{2}\right)}{2} \quad . \qquad \text{(E-29)}$$

The integral in equation E-22 may now be evaluated as

$$\frac{\partial F}{\partial \ell} = \frac{\Delta D}{2}\left[L\left(x+\frac{\ell}{2}\right)+L\left(x-\frac{\ell}{2}\right)\right] \qquad \text{(E-30)}$$

where, of course, $\delta\left(|x'|+\frac{\ell}{2}\right)$ never contributes, because $|x'|+\frac{\ell}{2}$ is always positive for positive ℓ. Returning to equation E-8, A_{11}, A_{22}, and A_{12} can be evaluated. First,

$$A_{11} = \frac{1}{\psi}\int_{-\infty}^{\infty}\left(\frac{\partial \Delta D}{\partial \alpha_o}\right)^2\left[\int_{-\infty}^{\infty} L(x-x')\,rect\left(\frac{x'}{|\ell|}\right)dx'\right]^2 dx \qquad \text{(E-31)}$$

$$A_{11} = \frac{1}{\psi}\left(\frac{\partial \Delta D}{\partial \alpha_o}\right)^2\iiint_{-\infty}^{\infty} L(x-x')\,L(x-x'')\,rect\left(\frac{x'}{|\ell|}\right)rect\left(\frac{x''}{|\ell|}\right)dx'dx''dx \qquad \text{(E-32)}$$

letting $\xi = x-x'$, $\eta = x'-x''$, interchanging the order of integration, and using the rect functions to set integral limits

$$A_{11} = \frac{1}{\psi}\left(\frac{\partial \Delta D}{\partial \alpha_o}\right)^2\int_{-\frac{\ell}{2}}^{\frac{\ell}{2}}\int_{-\frac{\ell}{2}-x''}^{\frac{\ell}{2}-x''}\phi_L(\eta)\,d\eta\,dx'' \qquad \text{(E-33)}$$

where $\phi_L(\eta)$ is the autocorrelation of the line spread function, L. Integrating the x'' integral by parts, and using the fact that $\phi_L(x) = \phi_L(-x)$ yields

$$A_{11} = \frac{2}{\psi}\left(\frac{\partial \Delta D}{\partial \alpha_o}\right)^2\int_0^{\ell}(\ell-x)\,\phi_L(x)\,dx \; . \qquad \text{(E-34)}$$

Equations E-23 and E-34 yields the value of A_{11}. Next,

$$A_{22} = \frac{1}{\psi}\int_{-\infty}^{\infty}\left(\frac{\Delta D}{2}\right)^2\left[L\left(x+\frac{\ell}{2}\right)+L\left(x-\frac{\ell}{2}\right)\right]^2 dx \qquad \text{(E-35)}$$

or

$$A_{22} = \frac{(\Delta D)^2}{2\psi}\left[\phi_L(0)+\phi_L(\ell)\right] \qquad \text{(E-36)}$$

where ϕ_L is again the autocorrelation of the line spread function. Finally,

$$A_{12} = \frac{1}{\psi}\int_{-\infty}^{\infty}\left(\frac{\partial \Delta D}{\partial \alpha_o}\right)\left(\int_{-\ell/2}^{\ell/2} L(x-x')\,dx'\right)\left(\frac{\Delta D}{2}\right)\left[L\left(x+\frac{\ell}{2}\right)+L\left(x-\frac{\ell}{2}\right)\right]dx\,. \qquad \text{(E-37)}$$

Interchanging the order of integration, and integrating over x

$$A_{12} = \left(\frac{\Delta D}{2\psi}\right)\left(\frac{\partial \Delta D}{\partial \alpha_o}\right)\int_{-\ell/2}^{\ell/2}\left[\phi_L\left(\frac{\ell}{2}+x'\right)+\phi_L\left(\frac{\ell}{2}-x'\right)\right]dx'\,. \qquad \text{(E-38)}$$

Letting $\frac{\ell}{2}+x' = x''$ in the first expression, separately letting $\frac{\ell}{2}-x' = x'''$ in the second expression, and using the symmetry of ϕ_L, A_{12} can be reduced to

$$A_{12} = \frac{\Delta D}{\psi}\left(\frac{\partial \Delta D}{\partial \alpha_o}\right)\int_{o}^{\ell}\phi_L(x)\,dx\,. \qquad \text{(E-39)}$$

With all equations reached as far as possible, σ_{α_o} and σ_{ℓ} are now calculated using a digital computer, programming a solution of equations E-6, 7, 16, 17, 23, 34, 36, and 39.

APPENDIX F

DETECTABILITY OF CONES IN LUNAR ORBITER PHOTOGRAPHS

By H. B. Hammill and E. A. Trabka

This appendix deals with the "detectability" of cone targets. The evaluation is based on the extension to two dimensions of certain results of statistical communication theory. Specifically, we will assume that the inherent limit of "detectability" of targets in Lunar Orbiter photographs is given by the performance of filters "matched" to the expected exposure, in the ground reconstruction system. After stating the relationship between the performance of such "matched" filters and the photographic system parameters, we will carry out an explicit evaluation of the detectability measure for a particular channel. This explicit evaluation, like that carried out in Appendix E, will be for the case in which it is possible to represent the photographic system, from film transmittance in the satellite to exposure on the ground, by an "equivalent" linear system.

The Matched Filter

The one-dimensional matched filter of communication theory is the "optimum" filter for deciding which one of two possible signals, $S_1(t)$ or $S_2(t)$, occurs in the presence of additive gaussian noise. If the output of the matched filter is thresholded (dichotomized) to make the required decision, the minimum average error probability for white noise backgrounds is given (Ref. 20) by the parameter

$$d^2 = \frac{E(1-\rho)}{2n_o} \qquad \text{(F-1)}$$

in which E is the average energy per signal, i. e.

$$E = \frac{1}{2}\left[\int_0^T S_1^2(t)\,dt + \int_0^T S_2^2(t)\,dt\right] \qquad \text{(F-2)}$$

ρ is the normalized cross correlation of the two signals of duration T, i.e.

$$\rho = \frac{1}{E}\int S_1(t)\,S_2(t)\,dt \qquad \text{(F-3)}$$

and n_0 in the noise power density per cycle of bandwidth (one-sided spectrum). The relationship between the detectability parameter d and the error probability P_e is given in Figure 1 of Ref. 20 :

$$P_e = 1 - erf\left(\sqrt{2}\,d\right) \qquad \text{(F-4)}$$

with the error function defined by:

$$erf(x) = \frac{1}{\sqrt{2\pi}}\int_{-\infty}^{x} e^{-\frac{1}{2}\mu^2}\,d\mu \qquad \text{(F-5)}$$

The utility of this result to detection and resolution problems in optical and photographic systems has recently been recognized (Ref. 21). It is possible to rewrite (F-1) in the form

$$d^2 = \frac{Q}{4n_0} \qquad \text{(F-6)}$$

in which Q denotes the "quadratic content"

$$Q = \int_0^T \left[S_1(t) - S_2(t) \right]^2 dt \qquad \text{(F-7)}$$

Eqn. (F-7) is of the form used by Harris (Ref. 21).

Extending this result to two dimensions, and using the notation of Appendix E, we will consider the detectability of targets to be given by

$$d^2 = \frac{Q}{\mathcal{E} N_0} \qquad \text{(F-8)}$$

with

$$Q = \int_{y_1}^{y_2} \int_{x_1}^{x_2} \left[F_1(x, y) - F_2(x, y) \right]^2 dx\, dy \qquad \text{(F-9)}$$

In writing (F-8) by analogy with the one-dimensional case, we have, however, taken N_0 to be the usual two-dimensional noise power density defined over both positive and negative spatial frequencies in both dimensions (all-sided spectrum). In Eqn. (F-9) we will consider that $F_1(x, y)$ denotes the noise-free exposure on the GRE film due to the presence of a cone target and $F_2(x, y)$ denotes the corresponding exposure for a level surface (See Figure E-1 of Appendix E).

We note that in view of (F-8) and (F-9), target detectability does not depend on target shape so that it is perfectly reasonable to consider a cone target equivalent to a three-bar test pattern yielding the same value of Q. However, this equivalence is not employed here.

In order to calculate Q we can compute $F_1 - F_2$ for the Lunar Orbiter system, again treating all non-linearities in a straightforward, uncompromising manner as was also possible in the procedure presented in Appendix E for estimating the accuracy of slope estimates. It is of interest, however, to proceed with further analysis for the case in which exposures, F_i , produced by the GRS kinescope on the ground may be related to corresponding film transmittances, T_{Si} ., in the satellite by convolution with an effective point spread $W(u, v)$. Letting

$$\left.\begin{aligned} \Delta F(x,y) &= F_1(x,y) - F_2(x,y) \\ \Delta T_S(x,y) &= T_{S1}(x,y) - T_{S2}(x,y) \end{aligned}\right\} \qquad \text{(F-10)}$$

we can write

$$\Delta F(x,y) = \int_{-\infty}^{\infty}\int W(x-u,\, y-v)\, \Delta T_S(u,v)\, du\, dv \qquad \text{(F-11)}$$

Inserting this expression for ΔF into Eqn. (F-9) yields:

$$Q = \int_{-\infty}^{\infty}\int \left[\int_{-\infty}^{\infty}\int W(x-u,\, y-v)\, \Delta T_S(u,v)\, du\, dv\right]^2 dx\, dy \qquad \text{(F-12)}$$

which can be written:

$$Q = \int_{-\infty}^{\infty}\int\int\int\int W(x-u',\, y-v')\, W(x-u,\, y-v)\, \Delta T_S(u'v')\, \Delta T_S(u,v)\, du\, dv\, du'\, dv'\, dx\, dy \qquad \text{(F-13)}$$

Interchanging the order of integration we get:

$$Q = \int_{-\infty}^{\infty}\int_{-\infty}^{\infty}\int_{-\infty}^{\infty}\int_{-\infty}^{\infty} \Delta T_s(u',v')\Delta T_s(u,v)\left[\int_{-\infty}^{\infty}\int_{-\infty}^{\infty} W(x-u',y-v')W(x-u,y-v)\,dx\,dy\right] du\,dv\,du'\,dv' \quad \text{(F-14)}$$

Eliminating x, y, u', v' in favor of x', y', ξ, η through the double two-dimensional transformation $x' = x - u'$, $y' = y - v'$, $\xi = u' - u$, $\eta = v' - v$ yields:

$$Q = \int_{-\infty}^{\infty}\int_{-\infty}^{\infty}\left[\Delta T_s(u+\xi, v+\eta)\Delta T_s(u,v)\,du\,dv\right]\left[\int_{-\infty}^{\infty}\int_{-\infty}^{\infty} W(x'+\xi, y'+\eta)\,W(x',y')\,dx'\,dy'\right] d\xi\,d\eta \quad \text{(F-15)}$$

The square brackets are recognized as the autocorrelation functions (denoted ϕ_Δ and ϕ_W) of ΔT_s and W respectively. Thus:

$$Q = \int_{-\infty}^{\infty}\int_{-\infty}^{\infty} \phi_\Delta(\xi,\eta)\,\phi_W(\xi,\eta)\,d\xi\,d\eta \quad \text{(F-16)}$$

APPENDIX G

IMAGE SYNTHESIS FOR THE LUNAR ORBITER PHOTOGRAPHIC SYSTEM

The purpose of this appendix is to present the analysis used to synthesize the image on the GRE master under various conditions of photographic system operation. The analysis was made to demonstrate the manner in which the content of various images on the GRE film could be expected to vary and to provide input data to evaluate the suggested data reduction techniques for determining the system frequency response from actual edge traces on the reconstructed photographs (Appendix C) . The analysis in this appendix is based upon the photographic data flow diagram shown in Figure 1. The input is assumed to be a one-dimensional topographic profile (i.e., the auxiliary angle α as a function of position). The corresponding one-dimensional output signal is synthesized in terms of the GRE Kinescope grid voltage or equivalently GRE film density. Because of the complex nature of the photographic system, general closed-form solutions for the output signal synthesis cannot be obtained. Instead, the analysis was implemented on the IBM 7044. Provision was made for varying the following parameters:

1. phase angle
2. lens-film MTF
3. magnitude of operational degradations (e.g., image motion, vibration and defocus)
4. radiation exposure,
5. exposure time,
6. size of the PS scan spot,
7. size of the GRE scan spot,
8. amount of dither introduced into GRE scan spot,
9. system gain and
10. total noise power in the image

Because a one-dimensional analysis is employed, the synthesized output signal represents the expected image on the GRE film when the topographic profile is assumed to be identical for an adequate number of resolution elements in the direction orthogonal to the profile. This condition is reasonable in the case of the 7 meter square test areas but not for the test cones.

In performing the analysis it is both convenient and necessary to have analytical expressions for the response of the various elements of the photographic system (e.g., photometric function, lens-film MTF, SO-243 D-log E curve, etc.). The various expressions used in the analysis are developed below.

Photometric Function

It was found for a fixed phase angle, g , that the photometric function $\Phi(g,\alpha)$ could be represented adequately by a quadratic expression in α , viz.

$$\Phi(g,\alpha) = a_0(g) + a_1(g)\alpha + a_2(g)\alpha^2 \qquad \text{(G-1)}$$

The coefficients a_0 , a_1 and a_2 depend upon the phase angle selected. Table G-1 shows the values of the coefficients obtained using a least square fitting procedure on the photometric function curves of the "Revised Lunar Reflectivity Model" described in the Jet Propulsion Laboratory Technical Report 32-664, dated 2 November 1964.[22] The standard deviation of the least squares fit is also given in the table. Lower standard deviations are obtained by employing higher degree polynomials, however, the quadratic is sufficient for present purposes. The coefficients $a_0(g)$, $a_1(g)$, and $a_2(g)$ are input parameters in the computational program.

Table G-1

COEFFICIENTS OF THE QUADRATIC EXPANSION
OF THE PHOTOMETRIC FUNCTION FOR
VARIOUS PHASE ANGLES

PHASE ANGLE, g, IN DEGREES	$a_0(g)$	$a_1(g)$ DEGREES^{-1}	$a_2(g)$ DEGREES^{-2}	STANDARD DEVIATION $\sigma(g)$
50	0.239	-0.00374	-0.0000487	.009
60	0.168	-0.00410	-0.0000421	.005
70	0.107	-0.00444	-0.0000356	.004
80	0.050	-0.00466	-0.0000305	.003

Lens-Film Modulation Transfer Function

Primary attention was given to the performance of the 24" focal length lens although the techniques are equally applicable to either lens system. Previous experience has shown that many MTF curves can be parametrically represented by the sum of an exponential function and a gaussian function employing three parameters, viz.

$$\tau(\nu) = b_0 e^{-b_1|\nu|} + (1-b_0) e^{-b_2\nu^2} \qquad \text{(G-2)}$$

The measured MTF for the 1965 lens S/N5-W plate* was multiplied by the MTF of Kodak SO-243 film (Figure 5 of LOP Engineering Note L-009038-KU)[7] to yield the lens-film response curve. Using this data, an estimate of the values of the parameters b_0, b_1 and b_2 was made by the method of differential correction with the result that

*Received in letter X/L-87-TPH dated 13 January 1966, from C. Nelson, Lunar Orbiter Project Office, Langley Research Center.

$$b_0 = 1.841\ ,\ b_1 = 0.0366\ ,\ \text{and}\ \ b_2 = 0.00099$$

The analytic curve and the experimental points representing the measured lens-film MTF are shown in Figure G-1. It is convenient to convolve the one-dimensional aerial image with the lens-film line spread function rather than perform the several Fourier transform operations necessary to employ expression G-2 for the lens-film MTF. To determine the line spread function it is only necessary to Fourier transform expression G-2 which can be done in closed form. This operation yields

$$L(x) = \frac{2b_0 b_1}{b_1^2 + (2\pi x)^2} + (1-b_0)\sqrt{\frac{\pi}{b_2}}\, e^{-\frac{\pi^2 x^2}{b_2}} \qquad \text{(G-3)}$$

Expression G-3 is employed in the image synthesis program with the constants b_0 , b_1 and b_2 being input parameters.

Operational Degradations

The image synthesis program includes several options for selecting various operational degradations. The degradations include image motion, image vibration and defocus. The line spread functions for these degradations are well known. The uniform image motion line spread function is a rectangular pulse of length ℓ and height $\frac{1}{\ell}$.

$$L(z) = \begin{cases} 1/\ell & |z| \le \frac{\ell}{2} \\ 0 & \text{elsewhere} \end{cases} \qquad \text{(G-4)}$$

Image vibration has a line spread function given by

$$L(z) = \frac{2}{\pi}(d - 4z^2)^{-1/2} \qquad |z| \le \frac{d}{2} \qquad \text{(G-5)}$$

where d is the total amount of vibration present. In using this expression, some caution must be exercised because of the divergence of the line spread at $z = \pm\frac{d}{2}$. To avoid this circumstance, the vibration line spread is assumed constant within a region near $\pm\frac{d}{2}$. When employing this

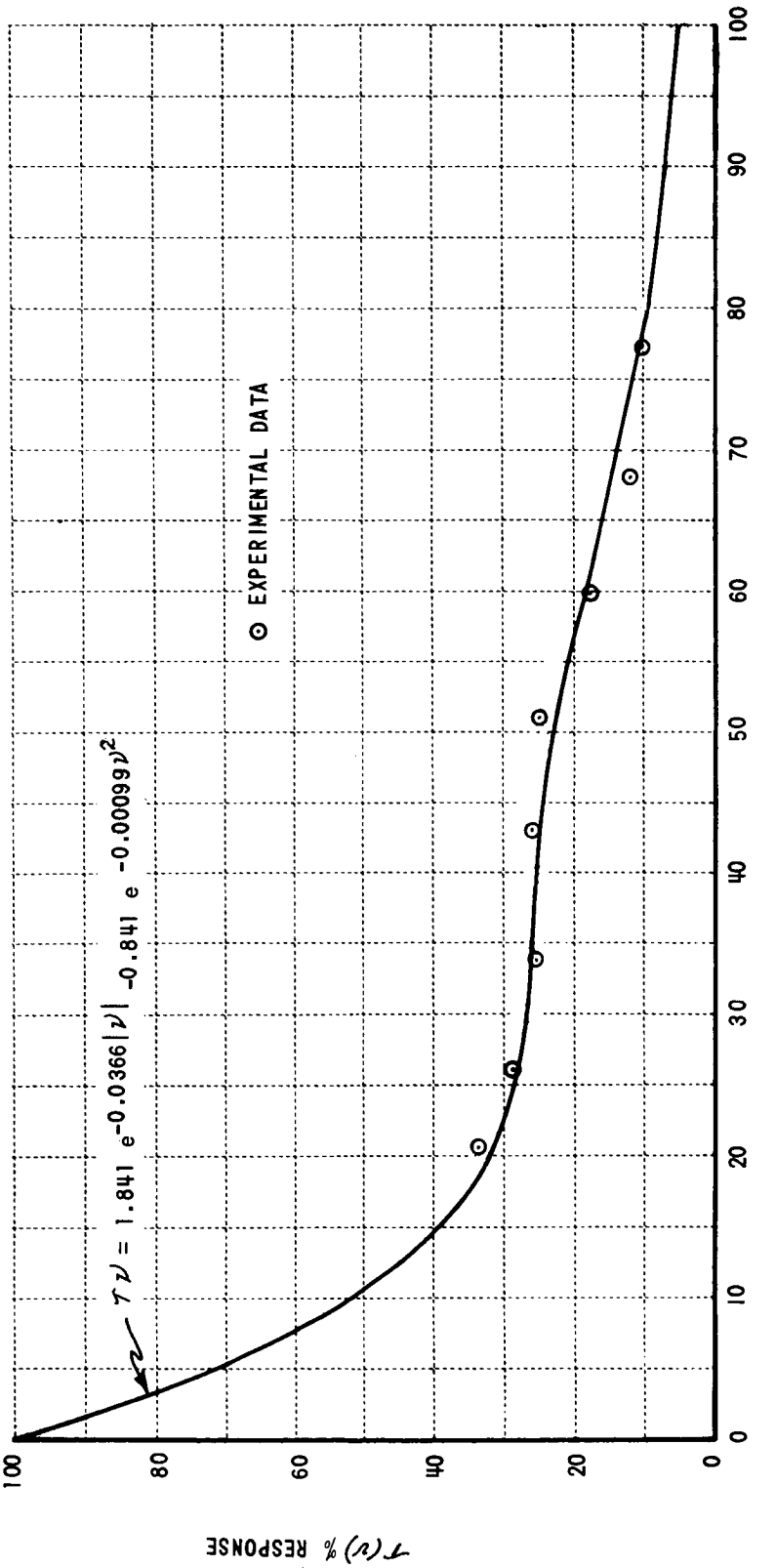

Figure G-1 ANALYTIC FIT TO LUNAR ORBITER LENS-FILM TRANSFER FUNCTION FOR THE 24" LENS

assumption, the area under the approximating line spread function must be renormalized to one.

The customary model used to represent defocus is a cylindrical point spread. The line spread corresponding to such a point spread is given by

$$L(z) = \frac{2}{\pi}\left[1 - \left(\frac{z}{r}\right)^2\right]^{1/2} \qquad |z| < r \qquad \text{(G-6)}$$

where r is the blur radius of the cylindrical point spread. When using this line spread in numerical computational procedure, contrary to the two previous forms, care must be used to sample $L(z)$ fine enough to ensure that it is adequately represented, especially for small amounts of defocus. If this is not done, normalization is lost and the energy contained in the image is not conserved. In addition, the simple cylindrical point spread model chosen to represent defocus is reasonable in the geometrical limit of many wavelengths of defocus.

D-Log E Curve

Experimental data for the conventional Hurter-Driffield response curve for SO-243 developed with SO-111 bimat film processing was received in letter X/L-94-TPH dated 15 February 1966. Two response curves were available; a nominal curve and a lower speed limit curve. Both curves can be represented by an analytical expression given by

$$D = C_1 + C_2\, erf\left[C_3 \log_{10}\left(C_4 + C_5 \frac{E}{E_0}\right)\right] \qquad \text{(G-7)}$$

where

$$erf(x) = \frac{1}{\sqrt{2\pi}} \int_{-\infty}^{x} e^{-\frac{t^2}{2}}\, dt$$

This is chosen incontrast to the conventional $D = \gamma \log\left(\frac{E}{E_0}\right)$ representation because it provides good reconstruction of densities near the toe of the response curve. This region must be considered important because its projected role in the Lunar Orbiter photography. Figure G-2, shows the

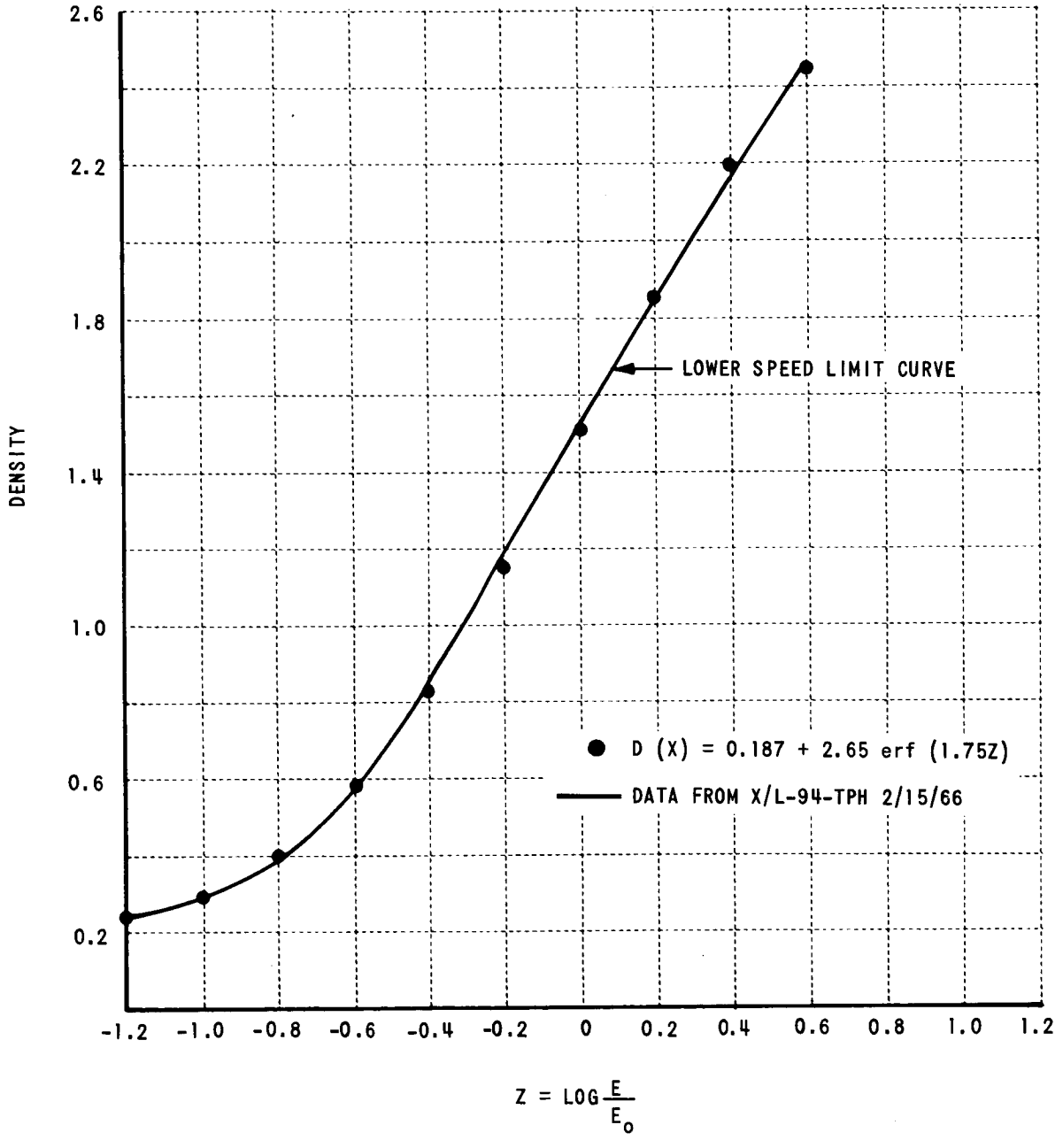

Figure G-2 ANALYTIC FIT TO THE H AND D CURVE FOR SO-243 DEVELOPED WITH SO-111 BIMAT FILM

comparison between the experimental data of lower speed limit curve and expression G-7 for appropriate values of the parameters. Since expression G-7 depends upon the ratio of two exposures, it can be written more conveniently as

$$D = C_1 + C_2 \, erf \left[C_3 \log \left(C_4 + C_5 \frac{\phi(\alpha)}{\phi(0)} \right) \right] \qquad \text{(G-8)}$$

In this form the constant C_4 represents the exposure acquired by the film due to some radiation dosage. Nominally, C_4 is taken to be zero. When the exposure due to the aerial image vanishes (i.e., when $\phi(\alpha)$ is zero such as in a crater shadow), the only contribution to densities above nominal base fog level is due to the parameter C_4. Thus, by examining the shadow areas in the reconstructed photographs, it may be possible to estimate the magnitude of the radiation dosage received by the film, if any. The constant C_5 represents the exposure on the SO-243 film from a flat area on the lunar surface $\left(\frac{\phi(\alpha)}{\phi(0)} = 1 \right)$ and therefore incorporates the effect of the exposure time. Since the exposure is selected to yield an average density across the format approximately equal to 0.8, C_5 was selected so that the density of a flat area was near 0.8. The nominal values of the constants were taken to be: $C_1 = 0.187$, $C_2 = 2.65$, $C_3 = 1.75$, $C_4 = 0.0$ and $C_5 = 0.3467$. This corresponds to an exposure time such that a flat area has a density of 0.74 on the SO-243 film.

Scanner - Communications - GRS Modulation Transfer Function

In Appendix A it was shown that a modulation transfer function could be written for the combined scanner-communications-GRS systems in the form

$$\tau(\nu_x, \nu_y) = \tau_1(\nu_x, \nu_y) \, \tau_2(\nu_x, \nu_y) \, \tau_c(u\nu_x + v\nu_y) \qquad \text{(G-9)}$$

where $\tau_1(\nu_x, \nu_y)$ is the MTF of the PS scanning spot and $\tau_2(\nu_x, \nu_y)$ is the MTF of the GRE scanning spot. The velocities of the scan spot have nominal values

of $u \approx 2,300$ mm/sec in the electrical scan direction and $v \approx 2.9$ mm/sec in the mechanical scan direction. Over the frequencies of interest - 100 lines/mm $\leq \nu_x, \nu_y \leq$ 100 lines/mm the dependence of τ_c upon ν_y may be neglected and expression G-9 written as

$$\tau(\nu_x, \nu_y) = \tau_1(\nu_x, \nu_y)\, \tau_2(\nu_x, \nu_y)\, \tau_c(\nu_x) \qquad \text{(G-10)}$$

where τ_c has been scaled from cycles/sec to lines/mm by omitting u. Both scanning spots are assumed to have a gaussian shape and hence gaussain frequency responses. In addition, the GRE spot is wobbled or dithered normal to the electrical scan direction. In letter X/L-94-TPH dated 15 February 1966, it was indicated that the voltage used to wobble the GRE spot is sinusoidal in nature with a frequency of about 2.2 mc/sec. The frequency response or MTF of the wobble is equivalent to that produced by harmonic vibration in the image and is given by $J_o(\pi \nu_y d)$ where d is the end-to-end magnitude of the dither or wobble. The frequency response of the GRE scan spot is the product of the frequency response of the wobble and the frequency response of the unwobbled gaussian spot, that is,

$$\tau_2(\nu_x, \nu_y) = e^{-2\pi^2 \beta_2^2 (\nu_x^2 + \nu_y^2)}\, J_o(\pi \nu_y d) \qquad \text{(G-11)}$$

where β_2 measures the width (1 σ point) of the GRE scan spot. Equation G-11 may now be written as

$$\tau(\nu_x, \nu_y) = e^{-2\pi^2 (\beta_1^2 + \beta_2^2)(\nu_x^2 + \nu_y^2)}\, \tau_c(\nu_x)\, J_o(\pi \nu_y d) \qquad \text{(G-12)}$$

with β_1 measuring the width (1 σ point) of the PS scan spot. As mentioned previously, it is more convenient in the analysis to convolve intensity distributions with line spread functions rather than performing the several Fourier transform operations necessary to employ the modulation transfer functions. The line spread function, $L(x)$, in the electrical scan direction is obtained by Fourier transforming $\tau(\nu_x, 0)$, or

$$L(x) = 2 \int_o^\infty e^{-2\pi^2 (\beta_1^2 + \beta_2^2) \nu_x^2}\, \tau_c(\nu_x) \cos(2\pi \nu_x x)\, dx \,. \qquad \text{(G-13)}$$

Similarly, the line spread function in the mechanical scan direction, $L(y)$, is obtained by Fourier transforming $\tau(o, \nu_y)$, or

$$L(y) = 2\int_o^\infty e^{-2\pi^2(\beta_1^2+\beta_2^2)\nu_y^2} J_o(\pi\nu_y d)\cos(2\pi\nu_y y)d\nu_y \qquad \text{(G-14)}$$

By employing the convolution theorem, G-14 can be written in a more convenient form

$$L(y) = \frac{2}{\pi\sqrt{2\pi(\beta_1^2+\beta_2^2)}}\int_{-d/2}^{d/2} \frac{e^{-(y-\xi)^2/2(\beta_1^2+\beta_2^2)}}{(d^2-4\xi^2)}\,d\xi$$

Integrating by parts results in further simplification for computational purposes, viz.

$$L(y) = \frac{2}{\pi\sqrt{2\pi(\beta_1^2+\beta_2^2)}}\left\{\frac{\pi}{4}\left[e^{-\frac{(y-\frac{d}{2})^2}{2(\beta_1^2+\beta_2^2)}} + e^{-\frac{(y+\frac{d}{2})^2}{2(\beta_1^2+\beta_2^2)}}\right]\right.$$
$$\left. - \frac{1}{2(\beta_1^2+\beta_2^2)}\int_{-d/2}^{d/2}\left[\sin^{-1}\frac{2\xi}{d}\right]\left[y-\xi\right]e^{-\frac{(y-\xi)^2}{2(\beta_1^2+\beta_2^2)}}\,d\xi\right\} \qquad \text{(G-15)}$$

Expressions G-13 and G-15 with β_1, β_2 and d as input parameters are employed in the image synthesis program. No effect of the pre-emphasis filters is included in $\tau_c(\nu_x)$ since it is assumed that their effects are reduced by de-emphasis filter in the GRS to yield a combined frequency response of unity over the frequency range of interest. The response of the communications system is shown in Figure G-3 both for 2:1 and 3:1 peaking of the GRE Amplifier. The figure was constructed by multiplying the MTF curves shown in Figure 12, 13 and 14 or 15 of LOP Engineering Note L-009038-KU[7] which represent MTF of the various components of what is referred to as the "communications system" in this report.

System Gain

System gain refers to relationship between the kinescope grid voltage or density on the GRE film and the transmittance of the SO-243 film. This can vary due to several sources (e.g., PS photomultipler gain, GRE electronics response, etc.). The nominal value of the gain is

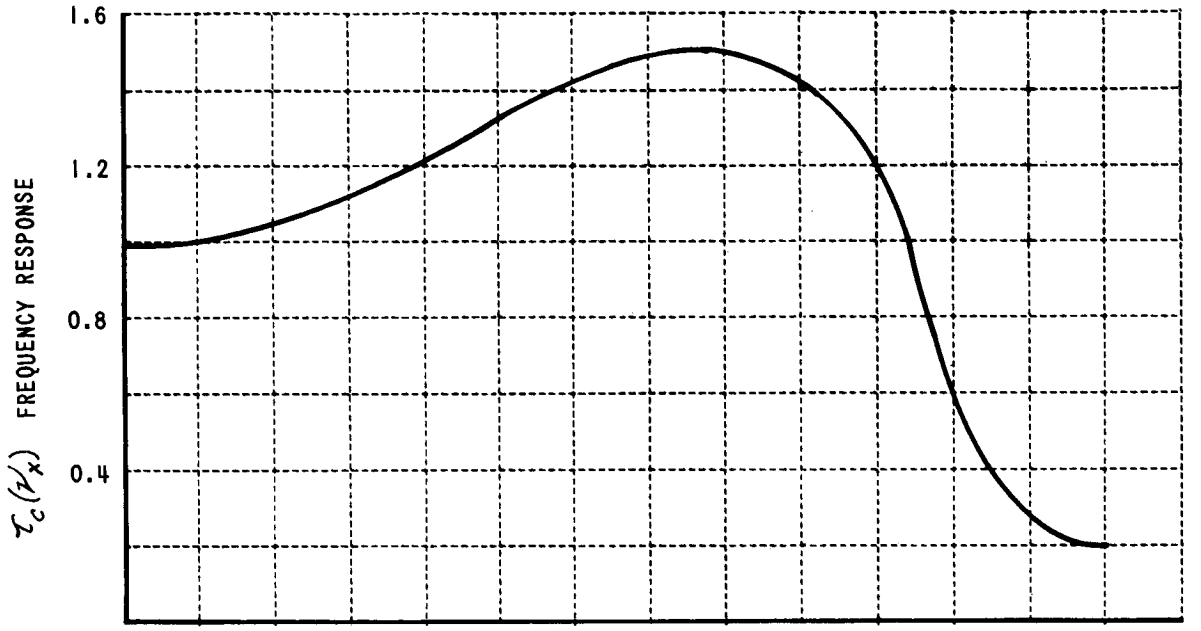

(a) 2:1 PEAKING OF GRE AMPLIFIER

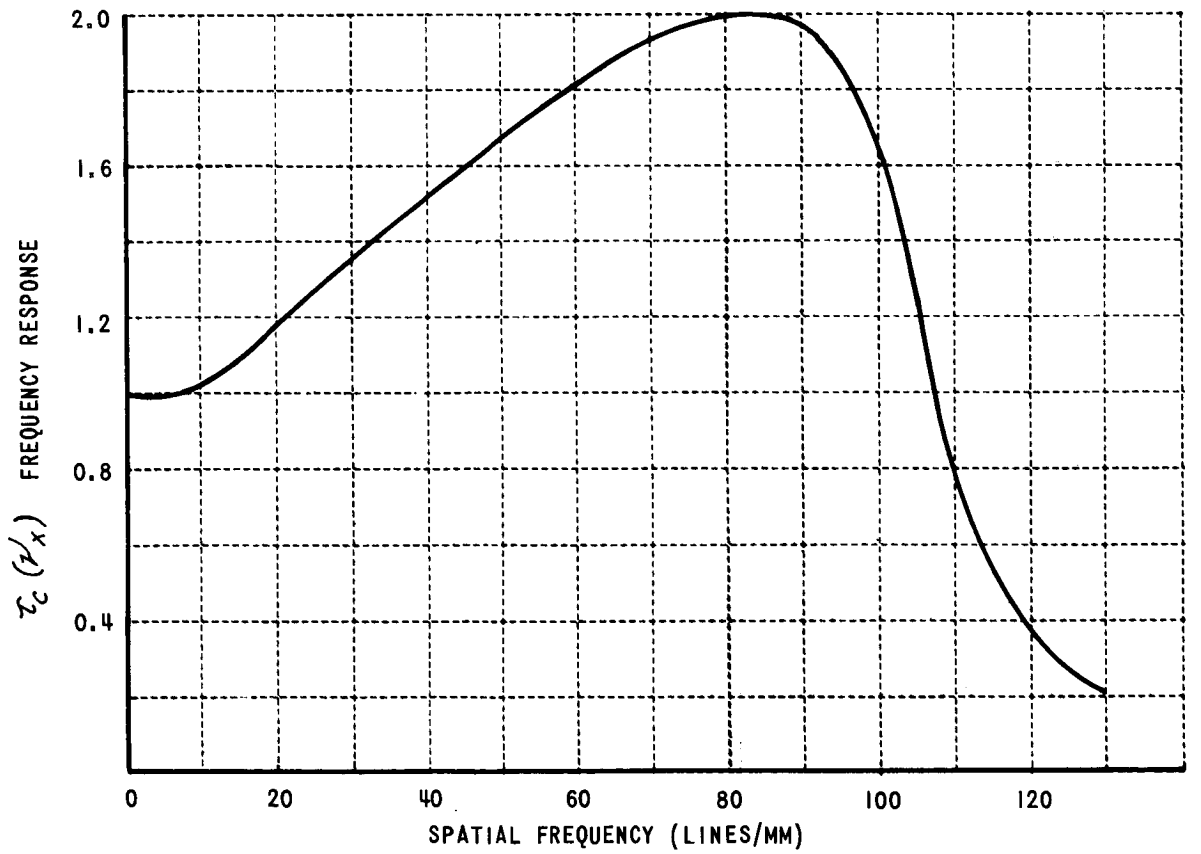

(b) 3:1 PEAKING OF GRE AMPLIFIER

Figure G-3 COMMUNICATIONS - GRS MTF

assumed 55.5 volts/unit transmittance determined from Figures 11 and 16 of LOP Engineering Note L-009038-KU*[7].

Image Synthesis Program

The flow diagram shown in Figure G-4 indicates the major sections of the synthesis program written for the IBM 7044 computer. All distances are scaled to the SO-243 film plane for convenience. The input function is the variation of slope, α (projected into the phase plane) with position. The output of the system is GRE kinescope grid voltage versus position. Provision is made to obtain the image trace (voltage vs. position) with and without gaussian random noise added. Figure 5 shows the calculation of the image trace for a slope profile 7 meters long and inclined at 7^{o} toward the sun assuming a phase angle of 70^{o} and nominal operation of the photographic system. Both the noise and noise free images are shown for comparison. Other examples of image traces are given in the main text.

* In a telephone conversation with T. Hansen of Langley Research Center it was verified that the slope of Figure 11 (L-009038-KU)[7] should be positive.

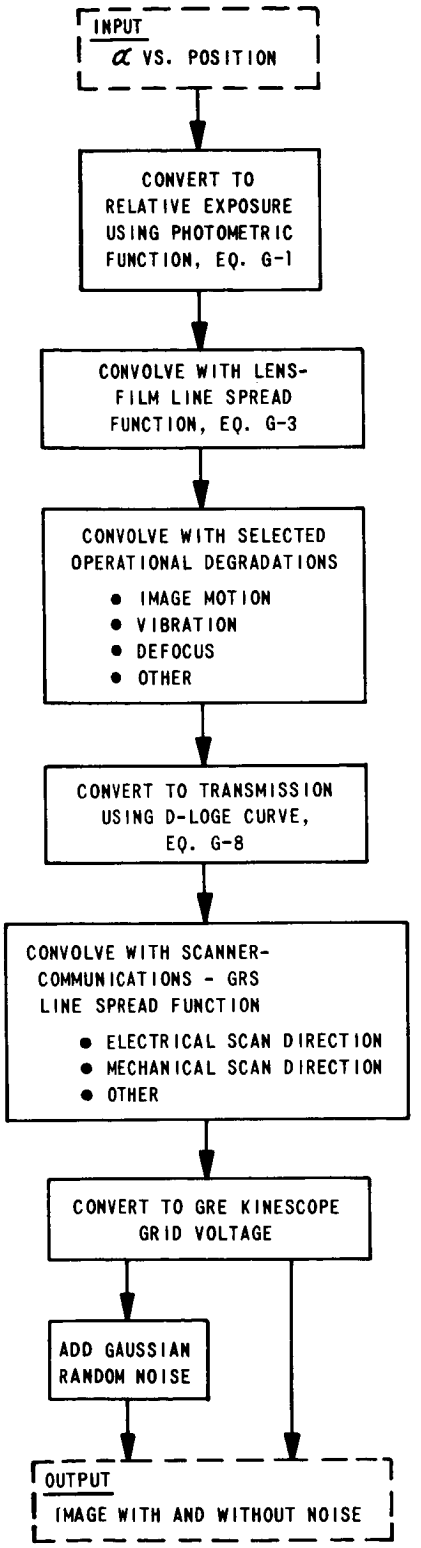

Figure G-4 IMAGE SYNTHESIS PROGRAM FLOW DIAGRAM

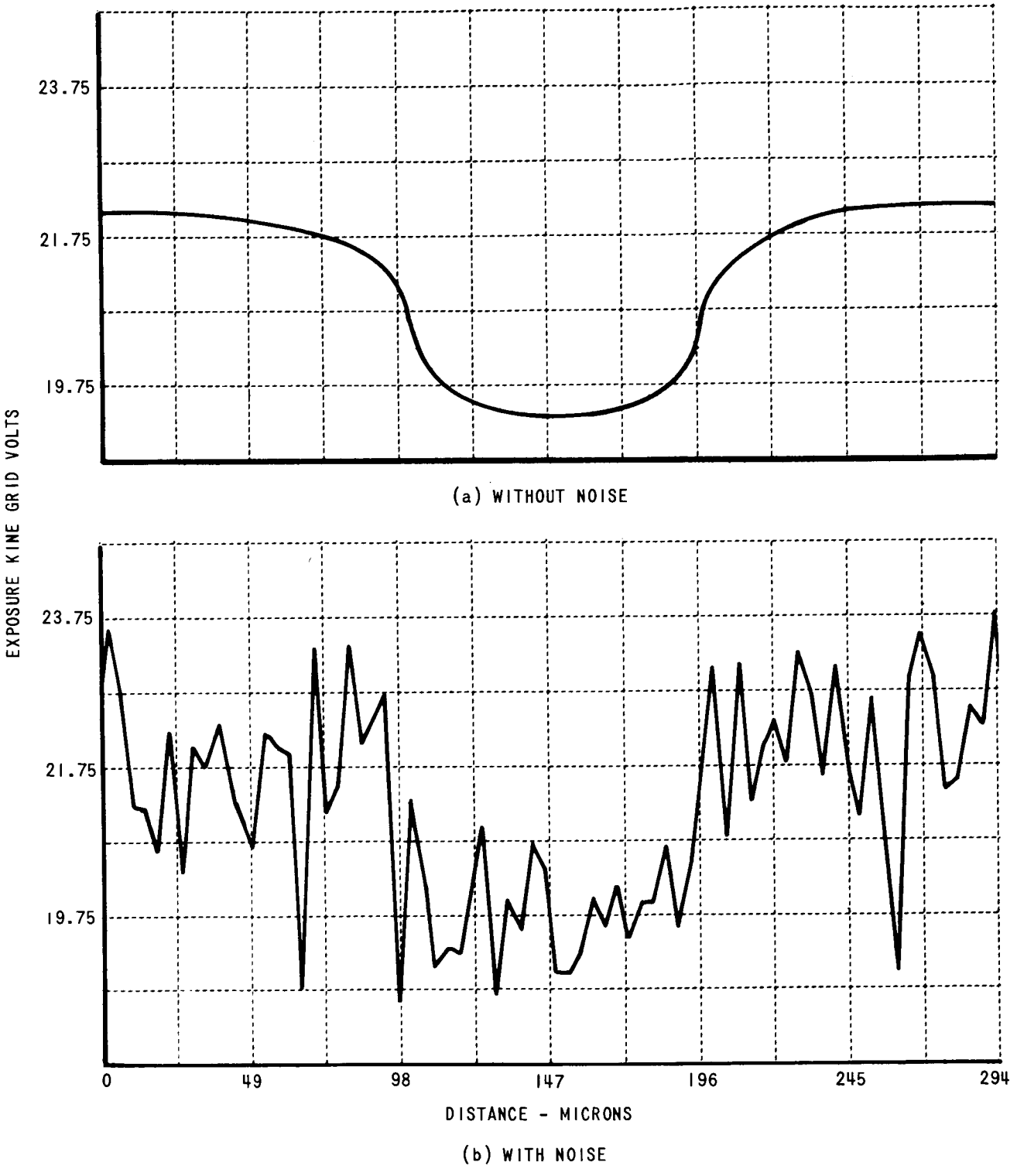

Figure G-5 EFFECT OF SYSTEM NOISE ON THE NOMINAL IMAGE OF A SLOPE WITH $\alpha = -7°$, $\ell = 7$ METERS

REFERENCES

1. Roetling, P.G.; Hammill, H.B.; and Holladay, T.M.: Quality Categorization of Aerial Reconnaissance Photography. RADC-TDR-63-279, 30 Spetember 1963.

2. Mazurowski, M.J.; Hammill, H.B.; and Snider, G.H.: A Study of Image Quality Evaluation. CAL Report No. VE-1867-G-1, November 1963.

3. Keene, George T.: Lunar Photo Study. Eastman Kodak Company, Z-3841, October 1965.

4. Scott, Frank; Scott, Roderic M.; and Shack, Roland V.: The Use of Edge Gradients in Determining Modulation-Transfer Functions. Photographic Science and Engineering, vol. 7, no. 6, Nov. - Dec. 1963, pp. 345-349.

5. Hammill, H.B.; Snider, G.H.; and Trabka, E.A.: A Study of Photographic Signal to Noise Ratio. CAL Report No. VE-1910-D-1, December 1964.

6. Lunar Orbiter Project Office: Lunar Orbiter Mission A Description. National Aeronautical and Space Administration, LOTD-102-0, September 1965.

7. Hopkins, W.D.: Handbook of LOP Response Curves and Noise Calculation. LOP Engineering Note L-009038-KU, April 19, 1965. (This also includes LOP Engineering Note L-011639-KU, June 30, 1965).

8. Mertz, P.; and Gray, F.: Bell System Technical Journal, vol 13, 1934, p. 464.

9. O'Neill, E.L.: Introduction to Statistical Optics. Addison-Wesley Publishing Company, Reading, Mass., 1963.

10. Lighthill, M.: Fourier Analysis and Generalized Functions. Cambridge University Press, London, Section 5.4, 1958.

11. Kopal, Zdenek: Topography of the Moon. Space Science Reviews, vol. IV, no. 5/6, September 1965, p. 771.

12. Trabka, E.A.: Wiener Spectrum of Scans Obtained from an Isotropic Two-Dimensional Random Field. J. Opt. Soc. Am., vol. 55, no. 2, Feb. 1965, pp. 203-204.

13. Davenport, W.; and Root, W.: Random Signals and Noise. Section 4.7, McGraw-Hill Co., Inc., 1958.

14. Huang, Thomas S.: The Power Density Spectrum of Television Random Noise. Applied Optics, vol. 4, no. 5, May 1965, pp. 597-601.

15. Marchand, F.: Derivation of the Point Spread Function from the Live Spread Function. J. Opt. Soc. Am., vol. 54, no. 7, July 1964, pp. 915-919.

16. Helstrom, C. W.: Statistical Theory of Signal Detection. Pergamon Press, New York, Chapters 7 and 8, 1960.

17. Swerling, P.: Parameter Estimation Accuracy Formulas. IEEE Transactions on Information Theory, vol. IT-10, no. 4, 1964, p. 302.

18. Kosofsky, L.; and Broome, G.: Lunar Orbiter: A Photographic Satellite. Presented at the Spring Convention of the SMPTE (Los Angeles, California), Mar. 28 - Apr. 2, 1965.

19. Rindfleisch, T.: A Photometric Method for Deriving Lunar Topographic Information. JPL TR No. 32-786, Sept. 15, 1965.

20. Becker, H.; and Lawton, J.: Theoretical Comparison of Binary Data Transmission Systems. CAL Report No. CA-1172-S-1, (Revised March 1961).

21. Harris, J.L.: Resolving Power and Decision Theory. J. Opt. Soc. Am., vol. 54, no. 5, May 1964, p. 606.

22. Willingham, D.: The Lunar Reflectivity Model for Ranger Block III Analysis. Jet Propulsion Laboratory Technical Report 32-664, 2 November 1964.